A Thesis for the Degree of Ph.D. in Engineering

Numerical Study on Propagation Behaviors of Gaseous Detonation in Two- and Three-Dimensional Tubes

February 2013

Graduate School of Science and Technology
Keio University

Yuta Sugiyama

Acknowledgement

There are several people who deserve thanks for the assistance they given me over the years at Keio University. First and foremost, my advisor Akiko Matsuo has supported in all aspects of my research, especially in CFD, presentation skills, and intellectual vitality. Hiroaki Miura honestly answered my questions and helped me even if he was busy. Jiro Kasahara at University of Tsukuba gave me the insight into the theoretical and experimental works of PDEs and RDEs. Humiteru Akamatsu at Osaka University gave me many advices about not only study but also life in PhD course. Hisahiro Nakayama gave much time to discuss detonation phenomena, which made some ideas described in this thesis.

I would like to thank several researchers in Matsuo laboratory for their assistance with issues ranging from detonation and fluid mechanics to CFD code – Takayuki Nirasawa, Kazuma Shigematsu, Kyohei Suzuki, Hironori Nakamura, Yutaka Shimada and others. I am grateful for the service of my thesis committee members Jiro Kasahara, Toshihisa Ueda and Koji Fukagata.

Finally, and most importantly, I am eternally grateful to my family and friends for moral support and patience.

Abstract

This thesis examines propagation behaviors of detonations in two- and three-dimensional tubes by numerical simulations with compressible Euler equations. The first part is concerned with spinning and pulsating detonations in square and circular tubes in order to understand propagation behavior near multi-cellular detonation limit. The second part discusses propagation mechanism in a two-dimensional curved channel in order to discuss stable propagation limit. The third part is focused on the characteristics of double cellular detonation. Chapter 1 gives the background and the motivation of the thesis. Chapters 2 and 3 reveal the propagation mechanism of pulsating and spinning detonations in circular and square tubes. Pulsating detonation cannot maintain a constant velocity and shows cyclic behavior in longitudinal direction. Spinning detonation can maintain its propagation when the coupling with transverse detonation and acoustic wave is satisfied. Chapter 4 treats two series of simulations of detonations propagating in a two-dimensional curved channel. One is that channel width L is equivalent to 0.5λ (λ: simulated cell width) and that the ratio of outer and inner radii R_{out}/R_{in} is chosen as a parameter. Steady curved detonation with Mach reflection structure is observed. The structure of three-shock configuration is investigated using three-shock theories with and without chemical reaction. In the case that Mach number of triple point is larger or smaller than CJ one, the simulated incident shock angles agree well with those by three-shock theory with or without chemical reaction. The other is

that R_{out}/R_{in} is fixed as 1.5 and 2 and that inner radius normalized by cell width R_{in}/λ is chosen as a parameter. Curved detonation front appeared and became more stable at a larger R_{in}/λ as well as the previous experimental results. I applied the idea of quasi-steady solution to the numerical results of detonation propagating in a two-dimensional curved channel and confirmed that the detonation propagates steadily in the case of larger shock radius of detonation front than the critical value. This says that the idea of quasi-steady solution is available to a steadily propagating curved detonation and gives the stable detonation limit in a curved channel. In Chapter 5, double cellular detonations were numerically investigated using two-dimensional Euler equations with two successive chemical reactions, whose reaction lengths differ one order of magnitude. Simulated soot track images showed the double cellular structure with two cell widths that differ one order of magnitude, as well as previous experiments and numerical simulations. I successfully divided the double cellular detonation with two successive exothermic reactions into two detonations, primary and secondary detonations, with a single exothermic reaction, based on P-V relation of Rayleigh line and Hugoniot curves with the addition of the hypothetical condition of intermediate initial state. The linear stability analysis of planar detonation and the soot track images of double, primary and secondary detonations showed that instabilities of primary and secondary detonations are dominant to that of double cellular detonation with two successive reactions. I confirmed the validity of division of two successive reactions to clarify the detonation instability and its cellular structure. Chapter 6 gives the conclusion of the thesis.

Contents

List of Figures

List of Tables

Nomenclature

		SI unit
Roman characters		
A	momentum flux	(kg m/s)/(m^{2}s)
a	sound speed	m/s
a	mass fraction of reactant	
B	energy flux	J/(m^{2}s)
b	mass fraction of intermediate	
c	mass fraction of product	
c_p	constant-pressure heat capacity	J/kg/K
D	detonation velocity	m/s
D	diameter	m
$\mathbf{E}$	inviscid flux vectors in x direction	(various)
E_1, E_2	activation energies for two-step reaction model	J/kg
E_1, E_2	activation energies for two successive reactions model	J/mol
e	total energy per volume	J/m^3
$\mathbf{F}$	inviscid flux vectors in y direction	(various)
$\mathbf{G}$	inviscid flux vectors in z direction	(various)
H	total enthalpy per mass	J/kg
K_1, K_2	pre-exponential factors of two successive reactions model	m^3/kg/s

k_1	rate constant for two-step reaction model	$m^3/kg/s$
k_2	rate constant for two-step reaction model	$m^4/N^2/s$
L_{ind}	induction length	m
L	channel width	m
L	half reaction length	m
M	Mach number	
m	mass flux	$kg/(m^2s)$
P	pressure	Pa
$\mathbf{Q}$	conservative solution vector	(various)
Q	heat release	J/kg
R	gas constant	J/kg/K
R	gas constant	J/mol/K
R	radius of circular tube	m
R	distance from axis of two-dimensional curved channel	m
$\mathbf{S}$	chemical source vector	(various)
T	temperature	K
t	time	s
u	velocity in x direction	m/s
V	specific volume	m^3/kg
V	velocity	m/s
v	velocity in y direction	m/s
W	molecular weight	kg/kmol

w	velocity in z direction	m/s
x	Cartesian coordinate	m
y	Cartesian coordinate	m
z	Cartesian coordinate	m

Greek characters

α	reaction progress variables	
α	track angle of spinning detonation	degree
β	reaction progress variables	
β	shock angle of spinning detonation	degree
γ	specific heat ratio	
π	circular constant	
Θ	angle from triple point in a circumferential direction	degree
θ	shock angle	degree
θ	deflection angle	degree
θ	effective activation energy	
θ_M	Mach angle	degree
θ	switching function of explicit and implicit method in Appendix B	
ρ	density	kg/m^3
λ	cell width	m
τ	period of oscillation	s

τ	normalized time	
τ_{ind}	induction time	s
ω	reaction rate	$kg/m^3/s$

Operator

Δ	difference

Acronums

1/2	transition from the first to second reaction
A	initial state
CJ	Chapman-Jouguet
D	hypothetical initial state
I.S.	incident shock wave
l_1	Hugoniot curve of adiabatic
l_2	Hugoniot curve after the end of first chemical reaction
l_3	Hugoniot curve after the end of second chemical reaction
M.S.	Mach stem
PDE	pulse detonation engine
RDE	rotating detonation engine
R.F.	reaction front
T.P.	triple point
T.W.	transverse wave

vN	von Neumann point
ZND	Zel'dovich-von Nermann-Döring

Superscript

L	left side of cell boundary
n	time step
R	right side of cell boundary
*	empirical value
*	value for normalization
o	degree

Subscript

1	upstream condition
1/2	end state of first reaction in two successive reactions model
acou	acoustic wave
ave	averaged value
CJ	Chapman-Jouguet
curve	curved shock condition
cr	critical value
eq	equilibrium condition
i	incident shock wave
i	i-th reaction

ig	igntion
in	inner wall of two-dimensional curved channel
ind	induction state
j	grid point
m	Mach stem
n	normal direction
out	outer wall of two-dimensional curved channel
p	primary
planar	planar detonation
r	reflected shock wave
s	shock wave
s	secondary
tran	transverse wave
vN	von Neumann
α	induction phase
β	reaction phase

Chapter 1

Introduction

Gas-phase detonation is a shock-induced combustion wave that propagates with supersonic speed relative to sound of speed at upstream gas condition and that contains a reaction zone behind a leading shock wave. The premixed gas is compressed by the leading shock wave, and high pressure and temperature conditions are easily obtained. After shock compression, the premixed gas is immediately auto-ignited, and chemical reaction supports detonation propagation. Gas-phase detonation can achieve high-energy release rate and high-pressure without mechanical work, which attracts researchers to application for propulsion. In recent years, significant results were obtained by a detailed research on the concept of Pulse Detonation Engine (PDE), that creates thrust by burning the fuel in a combustion chamber where a detonation wave is periodically initiated and propagates, and Rotating Detonation Engine (RDE), that detonation always maintains its propagation in a circumferential direction of annular combustor. However, since detonation makes sudden pressure increase, it is hazardous: for example, accidentally generated detonation caused pipe rupture in Hamaoka nuclear power plant in 2001. For the practical use of detonation and the prevention of serious accident by detonation, its characteristics such as initiation mechanism and propagation behavior should be revealed. In the present thesis, numerical simulations are conducted in order to understand propagation behaviors of gas-phase detonations in two- and

three-dimensional tubes.

1.1. Historical background in detonation research

In the latter half of 19 century, Berthelot and Vieille [1] measured the gas-phase detonation velocity in a variety of gas fuels mixed with various diluted oxidizers for the first time. The early pioneers [1,2] recognized that the adiabatic shock compression induces the chemical reaction in a propagation of detonation. A quantitative theory that predicts the detonation velocity was formulated by Chapman [3] and Jouguet [4] after 20 years of the discovery of detonation by Berthelot and Vieille. Chapman and Jouguet based their theory on the works of Rankine [5] and Hugoniot [6,7] who investigated the physical value change across a shock wave. In detonation propagation, the tangency point of the Rayleigh line and Hugoniot curve, which is now well-known as Chapman-Jouguet (CJ) point in *P*-*V* plane, should represent the proper end state of chemical reaction after passing through a shock wave. The CJ criterion agrees with the experimentally measured propagation velocity. Hence, a detonation velocity can be calculated from thermodynamic consideration. In the 1940s, Zel'dovich [8], von Neumann [9] and Döring [10] independently formulated essentially the same one-dimensional model for the internal structure of detonation waves, and the equations including heat release were first applied. ZND (Zel'dovich-von Neumann-Döring) model considers a steady one-dimensional detonation with the non-reactive shock discontinuity prior to a reaction zone. Although one-dimensional detonation theory is well established by pioneers, experiments [11] revealed that detonation fronts usually

have complicated three-dimensional structures. The true three-dimensional detonation structures were not clear until the late 1950's. Until now, the structure and properties of detonation have been investigated by many researchers using experimental, theoretical, and numerical approaches, and they made a remarkable insight.

1.2. Detonation theory

In this section, I will show one-dimensional steady detonation. As described in 1.1., the simple description of steady one-dimensional detonation called the ZND model is well known. The ZND model neglects transport process, and assumes one-dimensional flow. Figure 1.1 shows the configuration of the ZND wave. The flow is steady in the shock-capturing coordinate. The ZND wave consists of the leading shock wave and the reaction zone after induction zone. The leading shock wave makes a discontinuous change in physical values from point 1 to 2 in Fig. 1.1 and triggers of chemical reaction. P_{vN} is called as von Neumann spike. In the induction zone, chain-branching reaction occurs before main heat release between points 2 and 3. The main reaction zone is located behind the induction zone and makes continuous change in physical values from point 3 to 4 in Fig. 1.1. After the end of chemical reaction, physical values are constant. The shock wave and the reaction zone propagate together at the detonation velocity.

The detonation propagates at the speed, D_1. The conservation of mass, momentum and energy of perfect gas are expressed by

$$\rho_1 u_1 = \rho u, \tag{1.1}$$

$$P_1 + \rho_1 u_1^2 = P + \rho u^2, \tag{1.2}$$

and

$$c_p T_1 + \frac{u_1^2}{2} + Q = c_p T + \frac{u^2}{2}, \tag{1.3}$$

where ρ, u, P, T are density, velocity, pressure and temperature, respectively. Here, gas is modeled as perfect gas with constant specific heat ratio γ. Subscript "1" means the upstream condition. Therefore, u_1 is equivalent to D_1. c_p and Q are the constant-pressure heat capacity and the heat release, respectively. When u is eliminated from (1.1) and (1.2), the result defines a line in the P-V plane called the "Rayleigh line", expressed by

$$\frac{P}{P_1} = \left(1 + \gamma M_1^2\right) - \gamma M_1^2 \frac{V}{V_1} \tag{1.4}$$

where $V = 1/\rho$ and $M = u/a$ are specific volume and Mach number. Here, a is defined as sound speed. A Rayleigh line passes through the point (P_1, V_1) and has the slope $-\gamma_1 M_1^2 = -\gamma_1^2 D_1^2 / a_1^2$. The limiting cases are the horizontal $D_1 = 0$ and the vertical $D_1 = \infty$. The equation for the Hugoniot curve in the P-V plane is obtained by eliminating u and T from Eq. (1.3) by using (1.1) and (1.2). The Hugoniot curve is

$$\frac{P}{P_1} = \left(\frac{\gamma+1}{\gamma-1} - \frac{V}{V_1} + \frac{2Q}{P_1 V_1} \right) \Bigg/ \left(\frac{\gamma+1}{\gamma-1} \frac{V}{V_1} - 1 \right). \tag{1.5}$$

The two equations (1.4) and (1.5) determine the state (P, V) for a given detonation velocity D_1, as the intersection of the Rayliegh line and Hugoniot curve. Figure 1.2 shows the diagram of the Hugoniot curves and Rayleigh lines on the P-V plane. The adiabatic and full-reaction Hugoniot curves are expressed by the equation (1.5) with Q = 0 and $Q = Q_{eq}$. The slope of the Rayleigh line indicates the detonation velocity D_1, and the intersection point A denotes initial condition. As the premixed gas experiences the leading shock wave, the solution of the Hugoniot curves with Q = 0 and Rayleigh lines discontinuously changes from point A to B. Regions of possible solutions are constructed by drawing tangents to the curve through the point A, and vertical (point E) and horizontal (point F) lines from A. The curve is thus divided into five regions as shown in Fig. 1.2. The two tangent points to the curve are called Chapman-Jouguet points D and G, generally referred to as CJ points, and denoted by D for the upper CJ point and G for the lower CJ point. Mach number at CJ point is unity, and flow is under thermal choking condition. Since the slope of Rayleigh line is always negative, the solution between point E and F is imaginary. Thus, region E-F is shown to be a physically impossible region.

Region C-D is called the strong-detonation region because the slope of Rayleigh line and Mach number M_1 is larger than that at CJ detonation. Within it, the pressure of the

burned gases is greater than that of CJ detonation wave. The gas velocity in a shock-attached frame is reduced to lower subsonic velocity by shock compression, and increases to higher subsonic velocity by chemical reaction. At the same time, the pressure and density increase significantly. A strong detonation wave is rarely observed, since it requires a special experimental setup for generating overdriven shock waves in a very strong confinement, such as a piston-initiation.

Region D-E is called the weak-detonation region. Within it, the pressure of the burned gases is lower than that of the CJ detonation wave. The gas velocity in a shock-attached frame is reduced to subsonic by shock compression, and increases to supersonic by chemical reaction. In general, a weak detonation wave is not observed because the subsonic flow cannot accelerate to supersonic speed only by the heat addition.

Under most experimental conditions, detonations are Chapman-Jouguet waves, and thermal choking condition at CJ point is important to maintain detonation propagation. When the slope of a Rayleigh line is less than that of Chapman-Jouguet waves, a Rayleigh line through the point A will not intersect with the full-reaction Hugoniot curve. Therefore, the wave speed at D corresponds to the minimum detonation wave speed.

In contrast to the upper CJ point, the CJ deflagration (corresponding to G) has the maximum wave speed of deflagrations. This is because a Rayleigh line through point A fails to intersect the full-reaction Hugoniot curve if the magnitude of its slope exceeds that of the tangent line. If the slope of a Rayleigh line is less than that of the

tangent line, it intersects the full-reaction Hugoniot curve at regions F-G and G-H.

Region F-G is called the weak-deflagration region. In passing through a weak deflagration wave, the gas velocity relative to the wave front is accelerated from lower subsonic velocity to a higher subsonic one. The solution in region F-G is often observed; the pressure in the burned-gas zone is slightly lower than that of the unburned gases in most experimental conditions.

Region G-H is called the strong-deflagration region. In passing through a strong deflagration wave, the gas velocity relative to the wave front must be accelerated substantially from subsonic to supersonic speed. Strong deflagration is never observed experimentally because the subsonic flow cannot accelerate to supersonic speed only by the heat addition.

1.3. Cellular structure of detonations

Experiments [11] revealed that detonation fronts usually have complicated three-dimensional structures with interior transverse waves. Many of the frontal features of two- and three-dimensional detonation structures have been revealed by experimental and numerical investigations. Figure 1.3 is a schematic of detonation structure in two-dimension. The leading shock is wrinkled and consists of incident shock wave I.S. and Mach stem M.S., joined at triple point T.P. by transverse waves T.W. which travel back and forth perpendicular to the front. Transverse waves T.W. collide with each other and walls, which induce local explosion and is important to keep propagation of detonation. As transverse waves T.W. repeat intermittent reflections, trajectories of triple

point, denoted in dashed lines in Fig. 1.3, make cellular pattern. The spacing by triple point trajectories is often called cell width, which is important parameter to discuss its propagation behavior. Cellular structure is commonly used to evaluate detonation propagation. Lee [12] reported that when a detonation propagates through rectangular and circular tubes whose width and diameter are larger than the critical values, it would succeed to maintain propagation of detonation through expansion area after diffraction. The cell width is measured as one to two orders of magnitude greater than the steady, one-dimensional detonation reaction length such as half reaction length. Many researchers investigated two-dimensional detonation and showed remarkable insight for the propagation behavior. The first attempt to simulate two-dimensional detonations was performed by Taki and Fujiwara [13] using two-step reaction model by Korobeinikov *et al*[14]. Kailasanath *et al*. [15] attempted to understand the effect of channel width on cellular structures. Shock configurations and distribution of energy release of detonation have been investigated by Bourlioux and Majda [16], Lefebvre and Oran [17], and Oran *et al*. [18]. The detonation that had more than three or four cellular structures across a two-dimensional channel were successfully simulated and visualized in the form of maximum pressure histories by Gamezo *et al*. [19, 20]. Sharpe [21] investigated the nature of transverse waves in numerical simulations, and the results are in remarkable agreement with experiments of cellular detonation, including the transverse shock structures and nature of the pockets of unburned gas. In usual gaseous reactive mixtures (for instance, mixtures of H_2 or C_nH_m with O_2), detonation is characterized by a single cellular structure because the chemical energy is released in

one step. Presles *et al.* [22] observed a double cellular structure in pure nitromethane and nitromethane-oxygen mixtures. They assumed that the double cellular structure could be associated with two characteristic chemical lengths during the process of heat release and the chemistry was supposed to proceed through two main steps. Investigations of double cellular detonation have been conducted [23-29] to reveal the propagation mechanism by the experiments and numerical simulations. Sugiyama and Matsuo [30] conducted numerical investigations on double cellular detonation in order to understand its characteristics using two successive reactions model.

In resent years, the detailed three-dimensional structure of detonation has been become clear because of improvement of computer power. Williams *et al*. [31] studied the two-headed mode in a square tube, and Deledicque and Papalexandris [32] studied multi-headed mode in a rectangular tube using a one-step chemical reaction model of Arrhenius' form. Eto *et al*. [33] and Tsuboi *et al*. [34] investigated the detailed shock structures in a rectangular tube of single- and two-headed modes using detailed reaction model. A few modes have been observed in detonation of circular tube such as spinning (single-headed), two-headed and multi-headed modes, and they are classified according to the number of transverse wave. Spinning detonation in circular tube, discovered experimentally in 1926 by Campbell and Woodhead [35] followed by a succession of papers by Campbell and Woodhead [36] and Campbell and Finch [37], is observed near detonation limit and the lowest mode that has only one transverse wave in a circumference direction, whereas two-headed detonation has two transverse waves along circumference and one transverse wave along a radius. Spinning detonation

propagates helically on the wall, and transverse detonation rotates around the tube wall. Tsuboi and Hayashi [38] and Tsuboi *et al*. [39] and Virot *et al*. [40] investigated the spinning detonation in a circular tube, and their simulated results agreed well with experimental data. Kasimov and Stewart [41] numerically investigated hydrodynamic instability of spinning detonations using a three-dimensional linear perturbation to find the heat release and activation energy dependence. Sugiyama and Matsuo [42] studied the influence of activation energy by one-step reaction model of Arrhenius form and showed that an increase of activation energy makes the simulated spinning detonation unstable. Cho *et al*. [43] investigated three-dimensional simulations of multi-headed detonation in a circular tube. They discussed differences of cellular structures and propagation behaviors in two- and three-dimensions.

1.4. Application of detonations

Gas-phase detonations can achieve high-energy release rate and high-pressure in a smaller chamber without mechanical work such as compressor. Significant results were obtained by a detailed research on the concept of Pulse Detonation Engine (PDE) and Rotating Detonation Engine (RDE) in order to apply detonation for propulsion. In this section, I mention the above two detonation engines.

1.4.1. Pulse Detonation Engine [44, 45]

PDE produces the thrust from intermittent generation and propagation of detonations. Figure 1.4 shows schematic pictures of the operation cycle of PDE.

In the phase (a), as detonation is intermittently initiated, fuel and oxidizer should be well mixed. After filling the premixed gas in a tube. In the phase (b), the detonation is initiated using igniter. There are two modes of detonation ignition. One is the deflagration to the detonation transition. A small amount of energy is provided at the end of the tube and deflagration occurs. The deflagration evolves into the detonation by the influence of the reflected compression waves. The other mode is direct initiation. The detonation is immediately ignited by a high-energy source. In the phase (c), the generated detonation near the closed end of tube propagates to the open end. In the phase (d), exhausting of the burned gas and purging is occurred. The rarefaction wave propagates from the open end to the closed end of the tube. Before rarefaction wave reaches the closed end of the tube, detonation product gas is under high-pressure condition (plateau condition), and it pushes the closed end, which becomes main thrust of PDE. After rarefaction wave reaches the closed end of the tube, the burned gas is released, and pressure at the closed end becomes small. After phase (d), refilling of fuel and oxidizer is conducted as shown in Fig. 1.4a.

The heat efficiency is good for combustion because the gas in the operation cycle of the PDE is compressed by the shock wave under constant volume. The system is simple because premixed gas is compressed without a mechanical compressor. However, it seems difficulties of fast exhaust of the combustion products, recharging with fresh combustible gases in high frequencies in order to obtain full efficiency.

1.4.2. Rotating Detonation Engine [46, 47]

RDE is a new type of continuous detonation engine in that detonation always maintains its propagation in a circumferential direction of annular combustor. Figure 1.5 is a schematic of RDE. Premixed gas is supplied through a narrow slit. Detonation always propagates in a circumferential direction. RDE utilizes one or more detonation waves that rotate in an annular chamber for energy conversion. After detonation propagation, expansion wave decreases the pressure near the narrow slit, which reduce to the inlet pressure after propagation of the detonation wave. This allows the reactants to automatically feed into the chamber. Therefore, the premixed gas always exists at upstream of detonation wave, and detonation maintains its rotation in an annular chamber. Unlike the PDE, it does not have to initiate a detonation many times in a second. Therefore, RDE provides a stable thrust, and it may be attractive to engineers as a new propulsive device. High-enthalpy burned gas is accelerated through a nozzle, which becomes main thrust of RDE. Nowadays, many research groups are investigating RDE system for optimal design. However, propagation behavior of a detonation in annular chamber is not well understood.

1.5. Objectives

The present research focuses on the propagation behaviors of detonations by two- and three-dimensional numerical simulations. In this thesis, propagation behaviors of pulsating and spinning detonations in three-dimensional tubes in Chapters 2 and 3, in a two-dimensional curved channel in Chapter 4 and of double cellular detonation in

Chapter 5 are described.

For small tubes, boundary layer introduces the heat and momentum losses that cause the detonation velocity deficits. Diameter is important parameter to understand the effect of boundary layer. However, in numerical simulations, it is difficult to conduct three-dimensional calculations with full Navier-Stokes equations because of high grid resolution for boundary layer near the wall. Since the calculation with Euler equations can artificially eliminate the loss of heat and momentum, the effect of initial conditions, tube dimension and geometry could be revealed in the simulations separately. In Chapters 2 and 3, pulsating and spinning detonations in three-dimensional tubes are numerically investigated using compressible Euler equations with the two-step chemical reaction model proposed by Korobeinikov *et al*. The geometry effects of diameter in a circular tube and channel width in a square tube and initial pressure are chosen as parameters. A series of simulations are carried out in an attempt to understand the propagation behavior of pulsating and spinning detonations in small square and circular tubes.

The previous studies of RDE showed propagation behaviors by two-dimensional calculations in circumferential and longitudinal directions and by three-dimensional calculations. However, in three-dimensional calculations, a width of annular combustion chamber is too narrow to investigate the three-dimensional effect such as diffraction and accumulation effects from inner and outer walls in a radial direction. It is evident that the circumferential velocity of detonation wave near the outer wall should be higher than that near the inner wall if its angular velocity keeps constant.

When self-sustaining detonation propagates with CJ velocity, it should have an oblique shock front relative to incoming premixed gas flow. Moreover, as a circumferential velocity of detonation rotating in annular combustion chamber linearly increases with the distance from its axis, self-sustaining detonation front should be curved in order to maintain a CJ oblique detonation front at each point between inner and outer walls. For the practical use of RDE, propagation behavior of detonation with the effect in radial direction should be revealed. In Chapter 4, I show the propagation mechanism of curved detonations in a two-dimensional curved channel to clarify the effect of the size of channel and the stable detonation limit. I show the characteristics of unstable and stable detonation propagation depending on the size of curved channel.

Some researchers investigated double cellular detonation by experiments and numerical simulations. They assumed that the double cellular structure could be associated with two characteristic chemical lengths during the process of heat release and the chemistry was supposed to proceed through two main steps. However, its characteristics are not well understood. In Chapter 5, I discuss the double cellular detonation using two successive exothermic reactions model by numerical simulations in two-dimensional straight channel. The detailed discussions are conducted with the time evolutions of the simulated results, soot track images and Rankine-Hugoniot relations in the *P*-*V* plane. Two successive chemical reactions are separated into each chemical reaction, and I discuss the effect of two separated chemical reactions from the viewpoint of the instability and cellular structures of double cellular detonation.

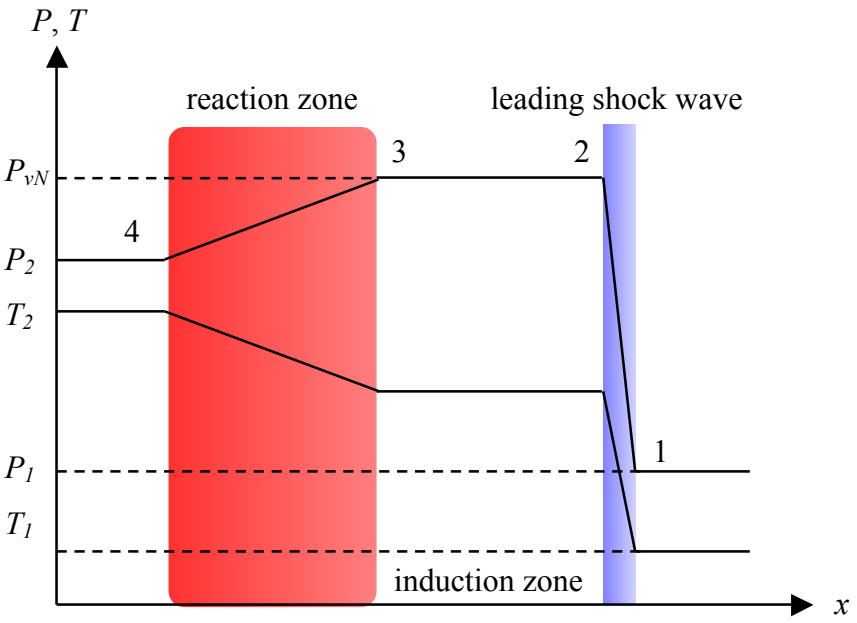

Fig. 1.1 Configuration of the ZND wave.

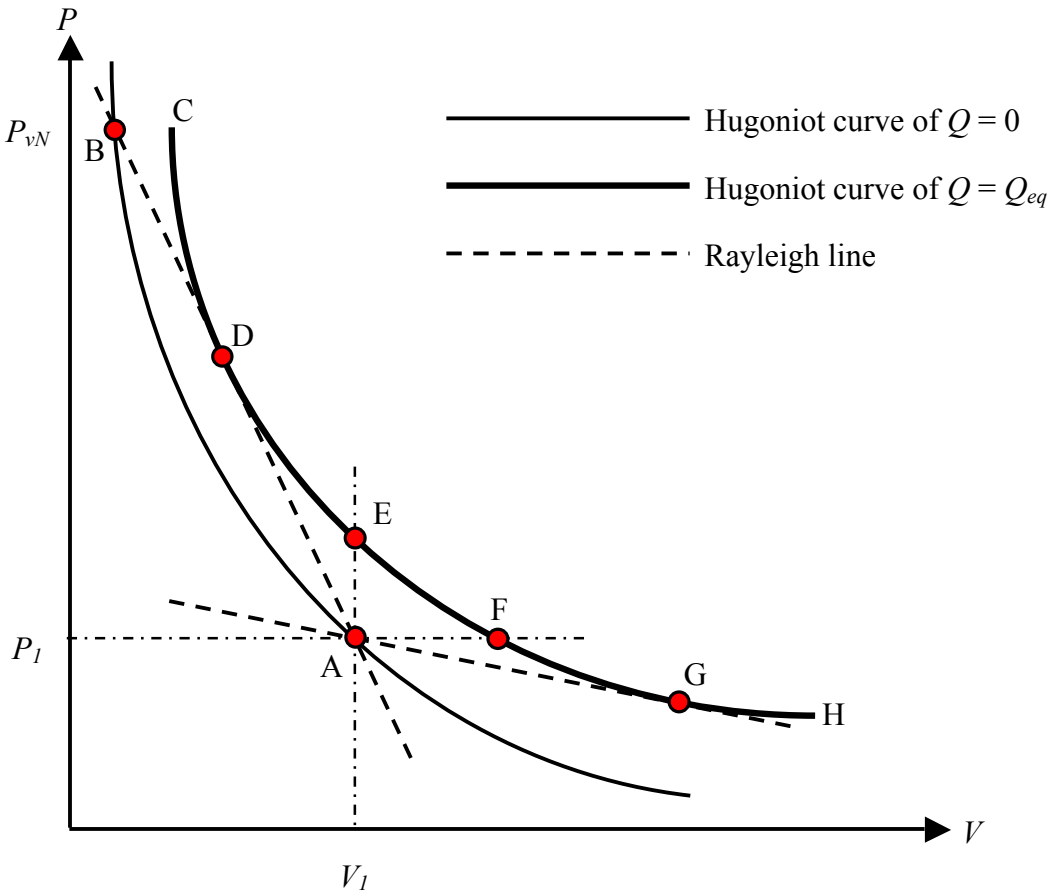

Fig. 1.2 The diagram of the Hugoniot curves and Rayleigh lines on the *P*-*V* plane.

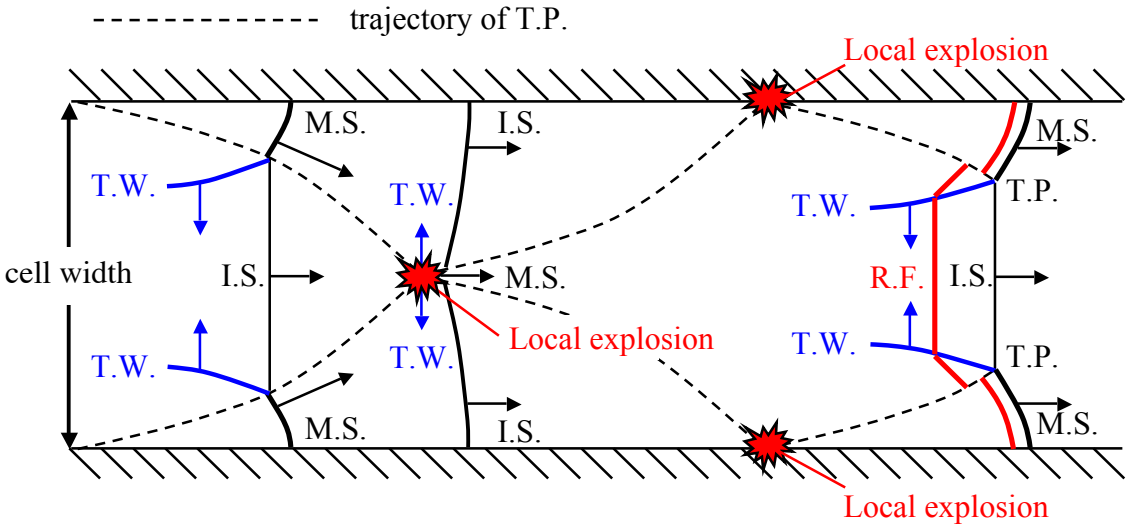

Fig. 1.3 A schematic of detonation structure in two-dimension.

T.W.: Transverse wave, M.S.: Mach stem, I.S.: Incident shock wave, T.P.: triple point, R.F.: Reaction front

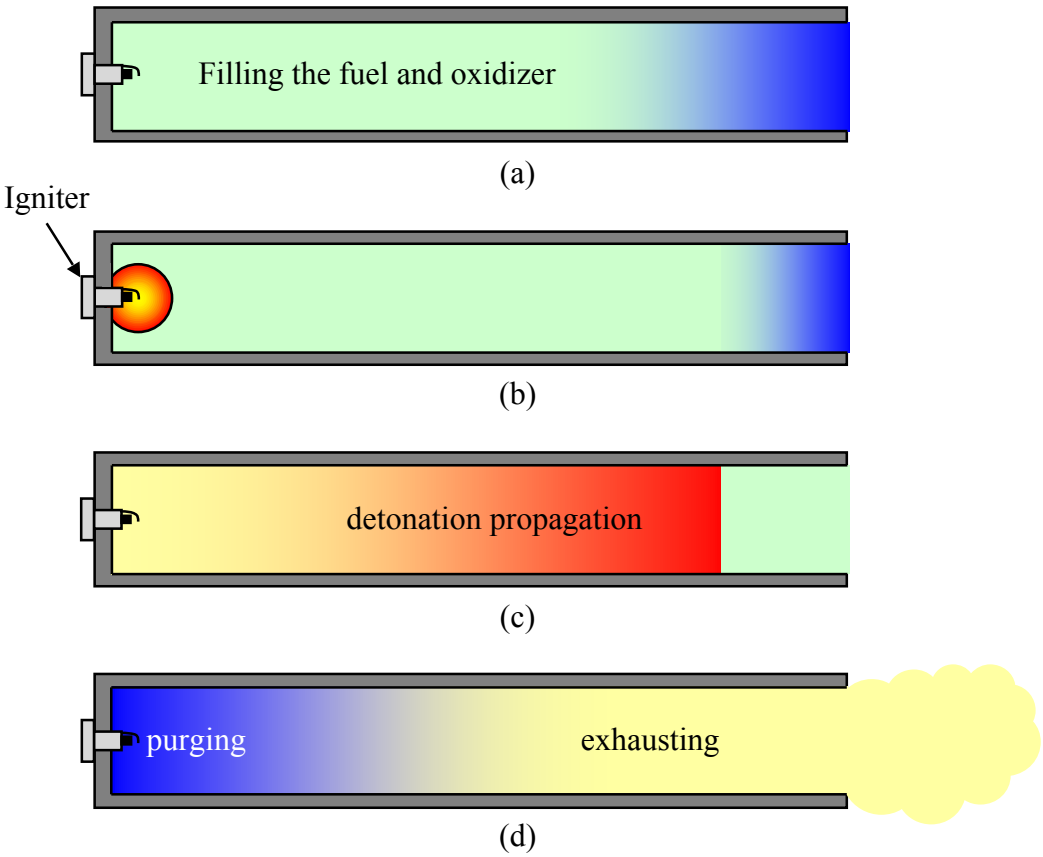

Fig. 1.4 Schematic pictures of the operation cycle of Pulse Detonation Engine.

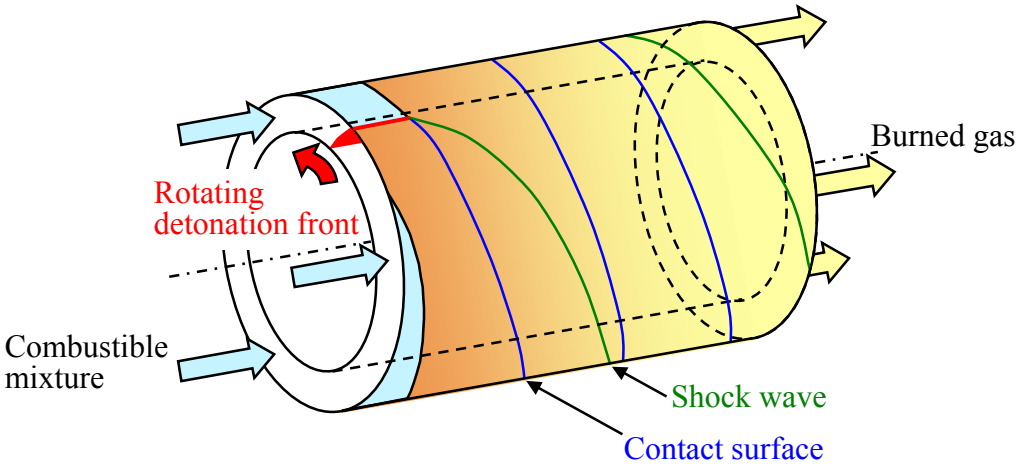

Fig. 1.5 A schematic picture of Rotating Detonation Engine.

Chapter 2

Pulsating detonations in circular and square tubes

2.1. Introduction

Experimental, numerical and theoretical approaches [11] revealed that detonation front usually has a complicated three-dimensional structure and that detonation propagates at constant velocity, namely Chapman-Jouguet velocity. In some experimental conditions, galloping detonation whose velocity repeats longitudinal pulsations is observed [48, 49]. Viscous boundary layer effects and turbulence play a crucial role in the cyclic process of a galloping detonation as well as in DDT process. In the numerical simulations, a longitudinally unstable detonation is often observed in one-dimensional simulation. Most of the previous studies using a one-step and a detailed chemical reaction model reproduced the low-frequency mode of one-dimensional unsteady detonations. Their results have been compared with the results of the linear stability analysis [50-55]. It has been studied so as to investigate one-dimensional longitudinal unsteadiness and obtain the stability boundary. One-dimensional detonation showed the pulsation further from the stability boundary. Near the boundary, the pulsations are regular and periodic, but they become nonlinear and chaotic further from the stability boundary. In these very unstable cases, the leading shock becomes very weak and decouples from the reaction front for long induction time that is estimated by physical values behind a weak shock wave. One-dimensional detonation is repeated by the intermittent re-ignition by the

shock compression and is essentially different from the experimentally observed galloping detonation.

Many researchers have investigated cellular detonation in two- and three-dimensions in order to reveal its propagation mechanism. In their works, detonations always show cellular structures and propagate at a CJ velocity because of completion of the potential exothermicity by transverse wave and triple point. However, in narrow tubes, detonation with multi-dimensional structure will fail, and pulsating detonation, which is supported by complex interaction of shock compression and chemical reaction, will be observed. The aim of Chapter 2 is to numerically investigate the three-dimensional propagation behavior of pulsating detonations in square and circular tubes and to show the difference between experimentally observed galloping detonations and numerically obtained pulsating detonations. As three-dimensional detonation shows longitudinal pulsation, its propagation behavior is quantitatively compared with that of numerically obtained one-dimensional pulsating detonation.

2.2. Numerical setup

The governing equations are the compressible and reactive three-dimensional Euler equations with two-step reactions model by Korobeinikov *et al*. [14] as shown in Eqs. (2.1), (2.2), (2.3) and (2.7) and Eqs. (2.4), (2.5), (2.6) and (2.7) for three and two dimensions, respectively.

$$\frac{\partial \mathbf{Q}}{\partial t}+\frac{\partial \mathbf{E}}{\partial x}+\frac{\partial \mathbf{F}}{\partial y}+\frac{\partial \mathbf{G}}{\partial z}=\mathbf{S} \tag{2.1}$$

$$\mathbf{Q}=\begin{bmatrix}\rho\\ \rho u\\ \rho v\\ \rho w\\ e\\ \rho\alpha\\ \rho\beta\end{bmatrix},\quad \mathbf{E}=\begin{bmatrix}\rho u\\ \rho u^2+P\\ \rho uv\\ \rho uw\\ (e+P)u\\ \rho\alpha u\\ \rho\beta u\end{bmatrix},\quad \mathbf{F}=\begin{bmatrix}\rho v\\ \rho vu\\ \rho v^2+P\\ \rho vw\\ (e+P)v\\ \rho\alpha v\\ \rho\beta v\end{bmatrix},\quad \mathbf{G}=\begin{bmatrix}\rho w\\ \rho wu\\ \rho wv\\ \rho w^2+P\\ (e+P)w\\ \rho\alpha w\\ \rho\beta w\end{bmatrix},\quad \mathbf{S}=\begin{bmatrix}0\\ 0\\ 0\\ 0\\ 0\\ \omega_\alpha\\ \omega_\beta\end{bmatrix}, \tag{2.2}$$

$$e=\frac{P}{\gamma-1}+\rho Q\beta+\frac{1}{2}\rho\left(u^2+v^2+w^2\right), \tag{2.3}$$

$$\frac{\partial \mathbf{Q}}{\partial t}+\frac{\partial \mathbf{E}}{\partial x}+\frac{\partial \mathbf{F}}{\partial y}=\mathbf{S} \tag{2.4}$$

$$\mathbf{Q}=\begin{bmatrix}\rho\\ \rho u\\ \rho v\\ e\\ \rho\alpha\\ \rho\beta\end{bmatrix},\quad \mathbf{E}=\begin{bmatrix}\rho u\\ \rho u^2+P\\ \rho uv\\ (e+P)u\\ \rho\alpha u\\ \rho\beta u\end{bmatrix},\quad \mathbf{F}=\begin{bmatrix}\rho v\\ \rho vu\\ \rho v^2+P\\ (e+P)v\\ \rho\alpha v\\ \rho\beta v\end{bmatrix},\quad \mathbf{S}=\begin{bmatrix}0\\ 0\\ 0\\ 0\\ \omega_\alpha\\ \omega_\beta\end{bmatrix}, \tag{2.5}$$

$$e=\frac{P}{\gamma-1}+\rho Q\beta+\frac{1}{2}\rho\left(u^2+v^2\right), \tag{2.6}$$

and

$$P=\rho RT, \tag{2.7}$$

where **Q, E, F, G,** and **S** are the conservative solution vector, the inviscid flux vectors in the *x*, *y* and *z* directions, and the chemical source vectors, respectively. The fluid is an ideal gas with constant specific heat ratio of 1.4, and all diffusive effects are neglected. The Zel'dvich-von Neumann-Doring (ZND) wave structure model is useful for understanding the CJ detonation. The ZND model consists of a shock discontinuity followed by a zone of chemical reaction after a certain ignition delay. Two-step reaction model by Korobeinikov *et al.* [14] is used for chemical reaction, instead of all of the elementary chemical reactions occurring behind a leading shock wave. This simplified model represents the reaction mechanism with two phases; induction and exothermic periods whose reaction rates, ω_α and ω_β, are shown in Eqs. (2.8) and (2.9), based on the ZND model. In this model, induction progress variable α changes from 1 to 0 (exothermic progress variable β is constant with 1) in the induction period, and exothermic progress variable β changes from 1 to β_{eq} (α is constant with 0) in the exothermic period.

$$\omega_\alpha \equiv \frac{d\alpha}{dt} = -k_1 \rho \exp\left(-\frac{E_1}{RT}\right) \tag{2.8}$$

and

$$\omega_\beta \equiv \frac{d\beta}{dt} = \begin{cases} -k_2 P^2 \left[\beta^2 \exp\left(-\frac{E_2}{RT}\right) - (1-\beta)^2 \exp\left(-\frac{E_2+Q}{RT}\right)\right] & (\alpha \le 0) \\ 0 & (\alpha > 0) \end{cases}. \tag{2.9}$$

The parameters of this model in the present work are listed in Table 2.1. Premixed gas is modeled as stoichiometric hydrogen-air. Initial pressure is chosen as a parameter (P_1 = 0.2, 0.6 and 1.0 atm), and initial temperature is fixed as T_1 = 293 K.

As discretization methods, Yee's Non-MUSCL Type 2nd-Order Upwind Scheme [56] is used for the spatial integration, and Point-Implicit Method that treats only source term implicitly is used for the time integration. The details of Yee scheme and Point-Implicit Method are described in Appendix A and B. Grid resolution is defined as the number of grid points in induction length L_{ind} calculated by one-dimensional steady solution. In Chapter 2, 33 grid points in induction reaction length L_{ind} are set in all directions, respectively. Grid convergence study for detonation propagation is conducted in Appendix D, and grid resolution is determined by computational cost. Cell width λ is important parameter to discuss propagation behavior of detonation such as the existence of empirical critical diameter $\pi D_{cr}^* = \lambda$ and empirical channel width $4L_{cr}^* = \lambda$ (λ: cell width), respectively. Therefore, cell widths λ at each initial pressure P_1 are estimated by two-dimensional channel calculations. The computational grid is an orthogonal system, and channel widths L depend on the initial pressure and are approximately 200 L_{ind} (30 mm at P_1 = 1 atm, 45 mm at P_1 = 0.6 atm and 112.5 mm at P_1 = 0.2 atm). The wall boundaries in two-dimensional channel are adopted to adiabatic and slip conditions. In all two-dimensional calculations, the premixed gas velocity of incoming flow is 2000 m/s, which is slightly (about 3 %) overdriven with respect to CJ velocity in the present chemical parameters. The axial length in the computational grid is more than 500 L_{ind} to avoid disturbance from the outflow boundary, which is proposed by Gamezo *et al.* [19].

The computational grids for a square tube are an orthogonal system, whose channel widths L are varied between 0.32 and 2.70 mm. The computational grids for a circular tube are cylindrical system, whose diameters D are varied between 0.2 and 3.0 mm. Since the present computational grid of a circular tube has a singular point at a center, physical values on the singular point are averaged using the values around it. The wall boundaries in circular and square tubes are adopted to adiabatic and slip conditions. In all three-dimensional calculations, the premixed gas velocity of incoming flow is 2000 m/s, which is slightly (about 3 %) overdriven with respect to CJ velocity in the present chemical parameters. The axial length in the computational grid is more than 500 L_{ind} to avoid disturbance from the outflow boundary proposed by Gamezo *et al.* [19].

The results of one-dimensional steady simulation are used as an initial condition. Details of one-dimensional steady simulation are described in Appendix C. Sheets of two- and three-dimensional unburned gas mixture behind detonation front are artificially added in order to create initial disturbances.

2.3. Results and discussion

2.3.1. The effect of initial pressure, tube size and cell width

Previous paper [49] showed the existence of critical diameter and channel width, which are empirically obtained as $\pi D_{cr}^* = \lambda$ and $4L_{cr}^* = \lambda$ (λ: cell width), respectively. In order to discuss the effect of diameter D and channel width L, empirical critical diameter D_{cr}^* and empirical channel width L_{cr}^* are calculated by the simulated cell

width λ of two-dimensional calculations. Figure 2.1 shows the smoked track image at initial pressure P_1 = 1.0 atm and channel width L = 30 mm. Since pressure near a triple point shows higher value in a calculation region, the black tracks give trajectories of the triple points that form cellular structures. Table 2.2 shows the relation between initial pressures P_1, simulated cell widths λ, empirical critical diameters D_{cr}* and empirical critical widths L_{cr}*. The table indicates that simulated cell widths λ are one magnitude smaller than those of the detonation database [57]. Figure 2.2 and Table 2.3 show the calculation conditions and propagation modes; steady (○), unstable (△) and pulsating mode (×), for detonations in a circular tube. Red circles (●) show $D_{cr} = D_{cr}*/2 = \lambda/2\pi$. As diameter decreases, spinning detonation tends to fail as shown in Fig. 2.2, and pulsating detonations appear. In present simulations, the simulated critical diameter D_{cr} of spinning detonation is around half size of empirical critical diameter D_{cr}*. Figure 2.3 and Table 2.4 shows the calculation condition, track angle and propagation modes; spinning (○), and pulsating (×), for detonations in a square tube. Red circles (●) show $L_{cr} = L_{cr}* = \lambda/4$. As channel width decreases, spinning detonation shifts to pulsating one as shown in Fig. 2.3. In present simulations, the critical channel width L_{cr} of spinning detonation in a square tube agrees with that of empirical critical channel width L_{cr}*. In the case of pulsating detonation, track angles are obtained at which spinning detonation appears transiently before its failure, and listed in Tables 2.4. Simulated results of pulsating detonations show that the propagation mechanism is almost the same in each tube. Therefore, detailed investigation is carried out using one set of conditions in each tube; initial pressure P_1 = 1.0 atm and diameter D = 0.2 mm for

a circular tube, and initial pressure P_1 = 1.0 atm and channel width L = 0.32 mm for a square tube. The detailed investigations on spinning detonation are described in Chapter 3.

2.3.2. Periodic behaviors in a longitudinal direction

The soot tracks on the tube wall were recorded in previous experimental studies [11] and showed remarkable insight for the propagation mechanism of detonations. I show the soot track images using the maximum pressure histories on the wall in Figs. 2.4 and 2.5 for circular and square tubes, respectively. Figures 2.4a and 2.5a also show pressure histories of shock front on the wall for a circular tube and on the corner for a square tube, to observe the oscillation features in a long period. Figures 2.4b and 2.5b denote one cycle of the pulsation, and notations A–F in Figs. 2.4b and 2.5b correspond to those in Figs. 2.4a and 2.5a. Pressure is normalized with respect to the von Neumann spike P_{vN} of one-dimensional steady detonation. Horizontal black lines in Fig. 2.5b indicate the corner of a square tube. Specific features of pulsating detonation such as strong fluctuations in the longitudinal direction are clearly observed in the shock pressure histories in Figs. 2.4a and 2.5a. Therefore, the propagation mechanism of one cycle in the pulsating detonation in a circular tube can be described using the observation of Fig. 2.4. First, see the soot track image in Fig. 2.4b. Around point A, there is no dark region, indicating that the detonation mode should be in the failed regime. Around point B, the whole region becomes dark. At point C, small cellular patterns appear, indicating the existence of a multi-headed detonation wave, and the cell size expands toward point D.

Beyond point D, the soot track image shows that the detonation propagates as spinning detonation with two triple points on the wave front, but it finally disappears before point E. After that, the detonation assumes single-headed spinning mode and travels steady for a while until point F. Eventually, there is no high pressure track on the wall after point F, as is the case for point A. See the shock pressure history in Fig. 2.4a, to confirm the propagation mechanism of the pulsating detonation explained with Fig. 2.4b. At time B, a sudden pressure jump occurs, and after that, high-frequency oscillation at the higher-pressure level than P_{vN} is observed. Regularly repeated pressure peaks are observed between time E and F. After time F, the amplitude of oscillation gradually decreases and the pressure settles down to a level lower than P_{vN}. The above-described mechanism is repeated during the long range of numerical simulation. Furthermore, the soot track image in Fig. 2.4b qualitatively agrees with the experimental image of galloping detonation by Vasil'ev [49], which showed cyclic behavior in longitudinal direction including three regions of multi-headed, single-headed, and no detonations. As for the simulated result in a square tube observed in Fig. 2.5, the basic propagation mechanism, such as sudden explosion, change of the multi-headed detonation to the single-headed spinning detonation, and the failure of detonation structure, has the same features as observed in a circular tube. However, during propagation, the spinning detonation in a square tube collides with the tube walls. Therefore, the disturbances as the reflected waves on the walls are observed in the soot track image in Fig. 2.5b.

In order to reveal the wave structure of pulsating detonation, the density distributions and velocity histories on the wall in circular and square tubes are examined. Figures 2.6

and 2.7 show the density distributions in one cycle of pulsation on the wall in circular and square tubes, respectively. Horizontal white lines in Fig. 2.7 indicate corners of a square tube. Figure 2.8 shows the velocity histories of pulsating detonation in (a) circular and (b) square tubes. Notations 2.6a–2.6f and 2.7a–2.7f in Fig. 2.8 correspond to a–f in Figs. 2.6 and 2.7, respectively. Figures 2.6, 2.7 and 2.8 show the characteristics of the pulsating detonation as follows. (a) Local explosion occurs in the induction zone near the flame front. In this phase, the premixed gas, compressed by the leading shock wave whose velocity is underdriven, is auto-ignited after the induction period. Figure 2.9 shows ten time-evolving instantaneous pressure distributions around local explosion in a circular tube. After long induction phase at failed regime, ignition occurs in Fig. 2.9b. Compression wave is generated and spherically propagates from ignition point in Fig. 2.9c. In a circular tube, compression wave rotates on the wall in circumferential direction. Compression waves superpose and reflect each other at some point (almost half round away from ignition point on the wall) in Fig. 2.9d. This induces successive explosion as shown in Fig. 2.9e. In this phase, ignition generates next ignition, and successively generated compression wave appears as shown in Fig. 2.9f – 2.9i. Complex flow patterns behind the shock wave appear due to the reflected wave on the wall. Unburned premixed gas is compressed, and ignition becomes stronger. As new compression wave is so strong to prompt the chemical reaction immediately, inner detonation at the overdriven velocity is generated and propagates to the leading shock wave as shown in Fig. 2.9j. (b) The inner detonation propagates to the leading shock front. In this phase, non-planar inner detonation is generated because re-ignition occurs

multi-dimensionally. It propagates through the disturbed premixed gas behind the shock wave and penetrates the shock front. After penetration, disturbed overdriven detonation appears, and small disturbances in shock front grow to new triple points and transfer into multi-cellular detonation. (c) The inner detonation penetrates the leading shock front. The detonation velocity suddenly increases from underdriven to overdriven as shown in Fig. 2.8. (d) The penetration causes the overdriven detonation, where the chemical length, such as half reaction length, is much smaller than that of CJ detonation. Consequently, multi-headed detonation appears, which makes smaller cells in the tube as shown in Fig. 2.4b. In this phase, the shock velocity gradually approaches to CJ one. The number of triple point decreases from Fig. 2.6d to Fig. 2.6e, and from Fig. 2.7d to Fig. 2.7e because cell width strongly depends on the shock velocity. (e) The single-headed spinning detonation appears after the attenuation of multi-headed detonation and maintains its rotation for a while. In this phase, the shock velocity keeps CJ one. Transverse detonation has an important role to maintain propagation of spinning mode because it completes the potential exothermicity. However, the transverse detonation cannot maintain stable rotation because channel width and diameter is smaller than a limit value of spinning detonation. (f) Shock wave separates from reaction front because transverse detonation decays. The shock velocity decreases to $0.8D_{CJ}$. Finally, detonation becomes a mode of the failed regime, where the velocity is underdriven. After a certain time, a new explosion occurs as explained in (a). A series of processes is repeated in the long history of pulsating detonation. Detonation velocity varies from 0.8 to 1.6 D_{CJ}. The averaged velocity in one cycle of pulsating detonation is

slightly (about 3%) less than that of inflow.

In the previous experiments [49], the galloping detonation is observed near extinction limit, and detonation velocity periodically changes from underdriven to overdriven. The leading shock is just too weak to cause re-ignition for the underdriven velocity phase of the cycle. Viscous boundary layer effects and turbulence play a crucial role in the cyclic process of a galloping detonation as well as in DDT process. In this thesis, I try to understand the fundamental behavior of the interaction of chemical reaction and shock waves in three dimensions. In the failed regime, the reaction front separates from the shock front, and chemical reaction hardly affects the propagation of shock wave. This feature resembles the solution of the Riemann problem in which CJ state and upstream conditions are two initial states separated by discontinuity [54, 55]. Therefore, I compared the shock velocity in the failed regime with result of the Riemann problem. The shock velocity estimated by Riemann problem is 0.796 D_{CJ} and agrees well with the shock velocity of the failed regime in the present results as shown in Fig. 2.8. Moreover, the induction time τ_{ind} of 0.796 D_{CJ} condition is estimated as 5.55 μs, which qualitatively agrees with the duration of failed regime in Fig. 2.8. This says that pulsation of the present pulsating detonation comes from the intermittent re-ignition by the shock compression, which is essentially different from that of the experimentally observed galloping detonation.

2.3.3. One-dimensional features of pulsating detonation

Previous numerical simulations of shock-induced combustion around a hypersonic

projectile in quiescent detonable gases [58, 59] revealed oscillation models of two regimes using an *x-t* diagram on the stagnation streamline; one is the regular regime and the other is the large-disturbance regime. Daimon and Matsuo [54, 55] investigated the one-dimensional detonation in detail using a one-step reaction model by the Arrhenius rate law and a detailed reaction model, and the unsteady features of simulated results were well explained using the oscillation models. Pulsating detonations showed cyclic oscillation in the longitudinal direction. Therefore, I carry out a simulation of one-dimensional detonation with one-dimensional Euler Equations to show the periodic behavior. This result is referred to as "one-dimensional detonation". The one-dimensional features of pulsating detonation in circular and square tubes are created by the cross-sectional average of simulated results. Therefore, *x-t* diagrams created by three-dimensional data are directly compared with that of one-dimensional detonation. Figure 2.10 shows *x-t* diagrams of density distribution of (a) one-dimensional detonation and cross-sectionally averaged density distributions in (b) circular and (c) square tubes. As mentioned above, the averaged detonation velocity is slightly (about 3%) less than that of inflow. Therefore, the detonation waves look propagating towards left in Figs. 2.10b and 2.10c. The behaviors in Fig. 2.10 are the same as that of the large-disturbance regime, which repeats the process of local explosion, overdriven state, and failed regime. This indicates that pulsating detonation is strongly caused by the longitudinal instability of detonation. The pulsating detonation is observed when the multi-dimensional detonation cannot maintain its propagation. As the multi-headed detonation decays, detonation structure has no transverse wave, and hence,

quasi-one-dimensional features appear with strong oscillation in the longitudinal direction. I discuss the characteristic values for each case; the re-ignition time defined as the duration of failed regime, the period between local explosions, and the velocity of the failed regime. These values are 5.41 μs, 18.6 μs, and 1564 m/s in the case of one-dimensional detonation; 5.41 μs, 18.0 μs, and 1545 m/s in the case of a circular tube; and 3.51 μs, 12.8 μs, and 1557 m/s in the case of a square tube. The velocity of the failed regime in circular and square tubes agrees well with that of one-dimensional detonation. However, the re-ignition time and the period between local explosions in a square tube are smaller than those in one-dimensional detonation. The reason is that many waves are generated by the collision of transverse wave and the wall in the flow field as shown in Fig. 2.7 in the case of a square tube, which induce shorter interval of local explosion. When the channel width becomes small, the effect of the collision of transverse wave and the wall weakens, and the re-ignition time and the period between local explosions approach to those in one-dimensional detonation. In the case of a circular tube, there is no collision with transverse wave and the wall in the regime of spinning mode as shown in Fig. 2.6, and the re-ignition time and the period between local explosions agree well with those of one-dimensional detonation. These features do not depend on tube diameter. Moreover, the duration over which the spinning detonation maintains its rotation in a circular tube is longer than that in a square tube. This reason is also explained by the additional disturbance. In a square tube, additional disturbance induces the decay of spinning detonation as well as the shorter interval of local explosion. Thus, propagation of spinning detonation in a square tube is much more

unstable than that in a circular tube.

2.4. Summary

Pulsating detonations in circular and square tube at various initial pressures are numerically investigated using three-dimensional Euler equations with a two-step chemical reaction model proposed by Korobeinikov *et al* [14].

Pulsating detonations show periodic behavior in a longitudinal direction. The soot track image of pulsating detonation is numerically obtained using the maximum pressure history on the tube wall, which qualitatively agrees with the soot track of galloping detonation experimentally obtained by Vasil'ev. Numerical results show strong pulsations with the intermittent local explosion under cyclic behavior, where the detonation velocity varies from underdriven to overdriven in one cycle. At the initial stage of each pulsation, a new explosion occurs in the induction zone near the flame front, which develops the inner detonation. It overtakes the leading shock wave and creates a highly overdriven detonation wave. The overdriven wave induces multi-headed detonation and is gradually attenuated from the multi-headed mode to a single-headed spinning mode. After that, the spinning detonation disappears, and the shock wave separates from the flame front with increasing length of the induction zone. These processes are repeated in each pulsation. As the pulsating detonation shows strong oscillation in the longitudinal direction, the cross-sectionally averaged *x-t* diagrams are compared with an *x-t* diagram of one-dimensional detonation. Flow features and characteristic values such as re-ignition time, the period of pulsating

detonation, and the velocity of the failed regime in a circular tube agree with those of one-dimensional detonation. Therefore, it is concluded that longitudinal instability is dominant in pulsating detonation after the lack of a transverse wave.

Table 2.1 Chemical parameters of two-step reaction model.

Q	2.33 MJ/kg
E_1/R	9850 K
E_2/R	2000 K
k_1	3.0×10^8 m^3/kg/s
k_2	4.185×10^{-5} m^4/N^2/s

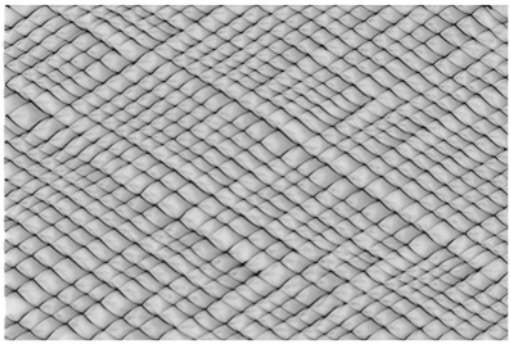

Fig. 2.1 Smoked track image at initial pressure P_1 = 1.0 atm and channel width L = 30 mm.

Table 2.2 Relation between initial pressure P_1, the simulated cell width λ, empirical critical diameter $D_{cr}^* = \lambda/\pi$ and empirical channel width $L_{cr}^* = \lambda/4$.

Initial pressure P_1 [atm]	cell width λ [mm]	empirical critical diameter D_{cr}^* [mm]	empirical critical length L_{cr}^* [mm]
1.0	1.62	0.516	0.405
0.60	3.33	1.06	0.833
0.20	10.2	3.25	2.56

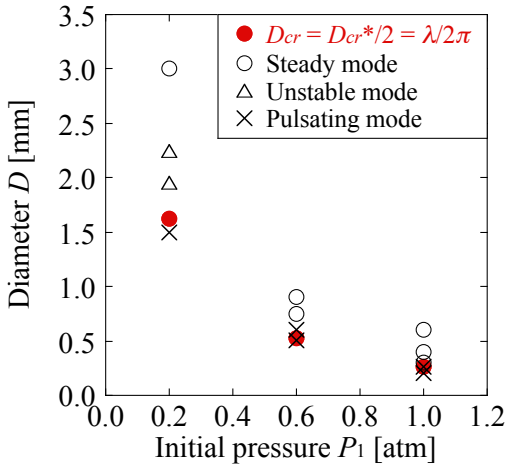

Fig. 2.2 Calculation conditions and propagation modes in a plane of initial pressure P_1 and diameter D; steady (○), unstable (△) and pulsating mode (×), for detonations in a circular tube. Red circles (●) show $D_{cr} = D_{cr}^*/2 = \lambda/2\pi$ (λ: simulated cell width).

Table 2.3 Relation of calculation conditions and propagation modes; steady (○), unstable (△) and pulsating (×), for detonations in a circular tube.

initial pressure P_1 [atm]	diameter D [mm]	propagation mode
1.0	0.20	×
1.0	0.26	×
1.0	0.30	○
1.0	0.40	○
1.0	0.60	○
0.6	0.51	×
0.6	0.60	×
0.6	0.75	○
0.6	0.90	○
0.2	1.50	×
0.2	1.95	△
0.2	2.25	△
0.2	3.00	○

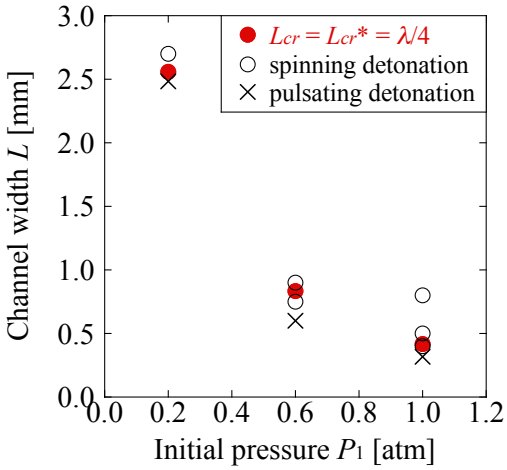

Fig. 2.3 Calculation conditions in a plane of initial pressure and channel width and propagation modes; spinning (○), and pulsating (×), for detonations in a square tube. Red circles (●) shows $L_{cr} = L_{cr}^* = \lambda/4$ (λ: simulated cell width).

Table 2.4 Relation of calculation conditions, track angle and propagation modes; spinning (○), and pulsating (×), for detonations in a square tube.

initial pressure P_1 [atm]	channel width L [mm]	track angle [º]	Propagation
1.0	0.32	44.3	pulsating
1.0	0.40	46.5	spinning
1.0	0.50	47.5	spinning
1.0	0.80	49.4	spinning
0.60	0.60	44.3	pulsating
0.60	0.75	46.7	spinning
0.60	0.90	47.5	spinning
0.20	2.48	44.6	pulsating
0.20	2.80	47.5	spinning

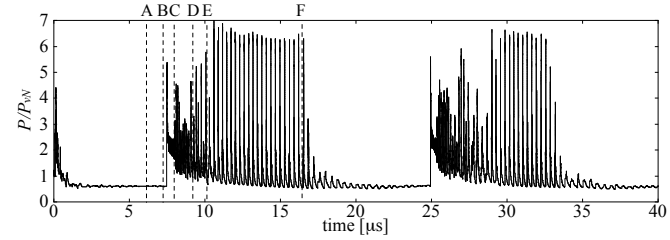

(a)

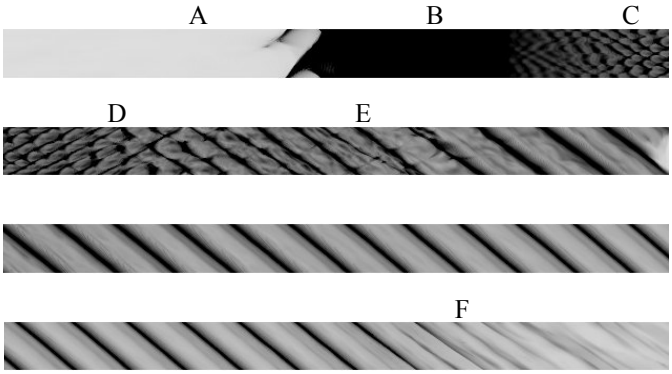

(b)

Fig. 2.4 (a) pressure history of shock front on the corner and (b) the soot track image on the wall in a circular tube. Notations A–F in (a) and (b) correspond.

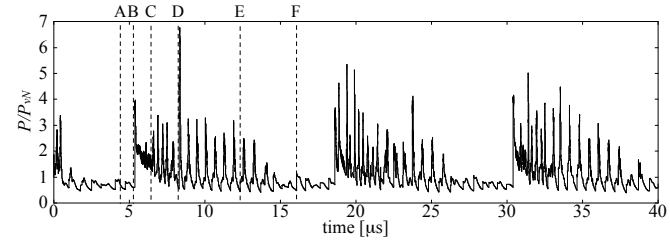

(a)

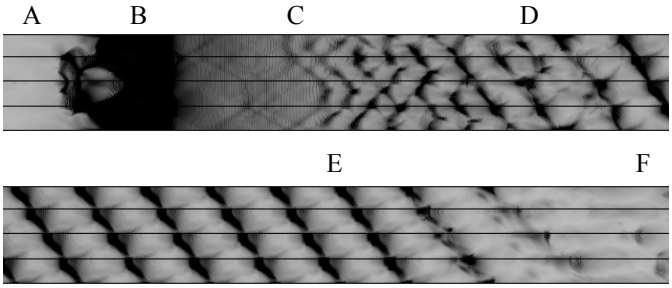

(b)

Fig. 2.5 (a) pressure history of shock front on the wall and (b) the soot track image on the wall in a square tube. Notations A–F in (a) and (b) correspond.

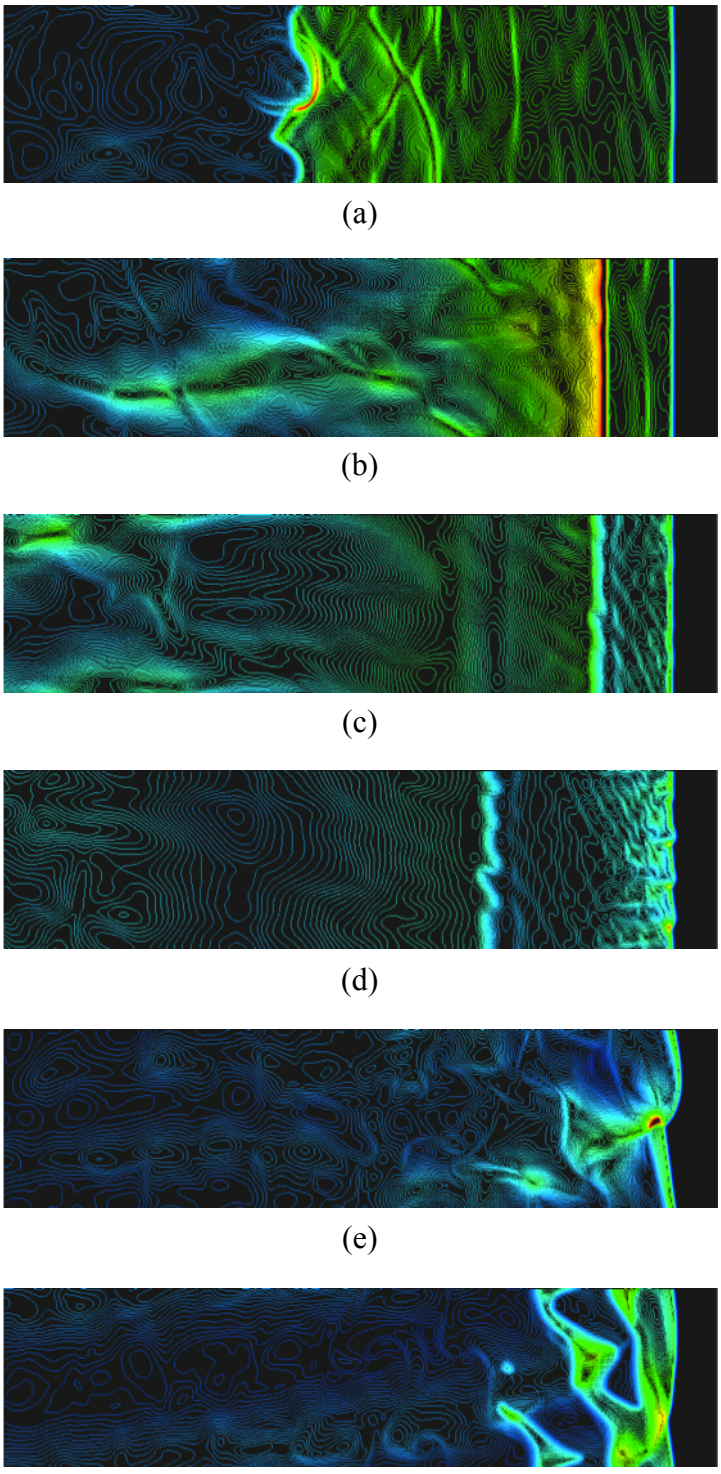

Fig. 2.6 Density distributions in one cycle of pulsations on the wall in a circular tube. Flow features are as follows: (a) local explosion occurs, (b) inner detonation propagates to the shock front, (c) inner detonation penetrates the shock front, (d) multi-headed detonations appear, (e) spinning detonations appear, and (f) transverse detonation decays.

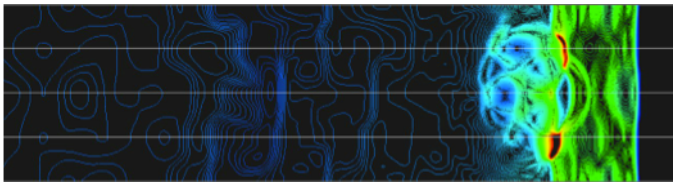

(a)

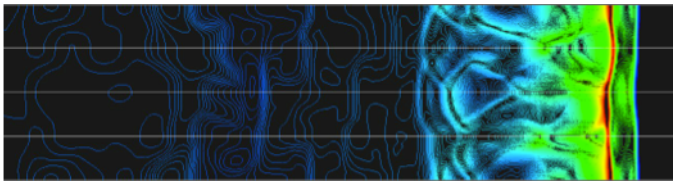

(b)

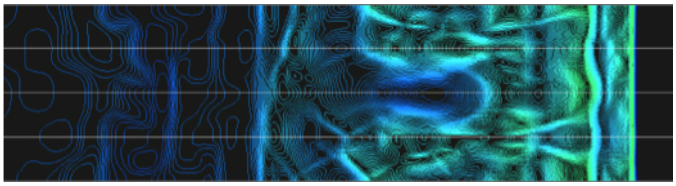

(c)

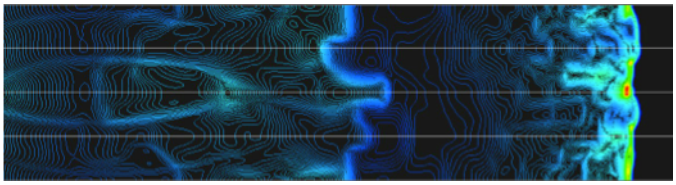

(d)

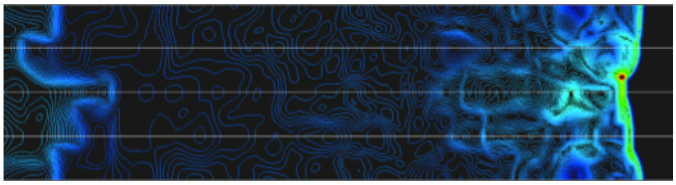

(e)

(f)

Fig. 2.7 Density distributions in one cycle of pulsations on the walls in a square tube. White lines indicate the corners of tube. Flow features are as follows: (a) local explosion occurs, (b) inner detonation propagates to the shock front, (c) inner detonation penetrates the shock front, (d) multi-headed detonations appear, (e) spinning detonations appear, and (f) transverse detonation decays.

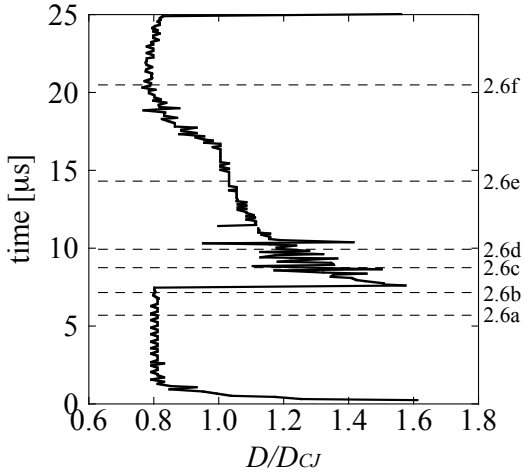

(a) Circular tube

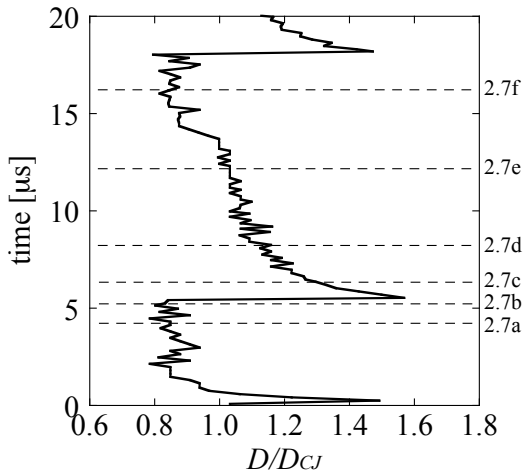

(b) Square tube

Fig. 2.8 Detonation velocity histories in (a) circular and (b) square tubes. Velocity is normalized with respect to that of CJ.

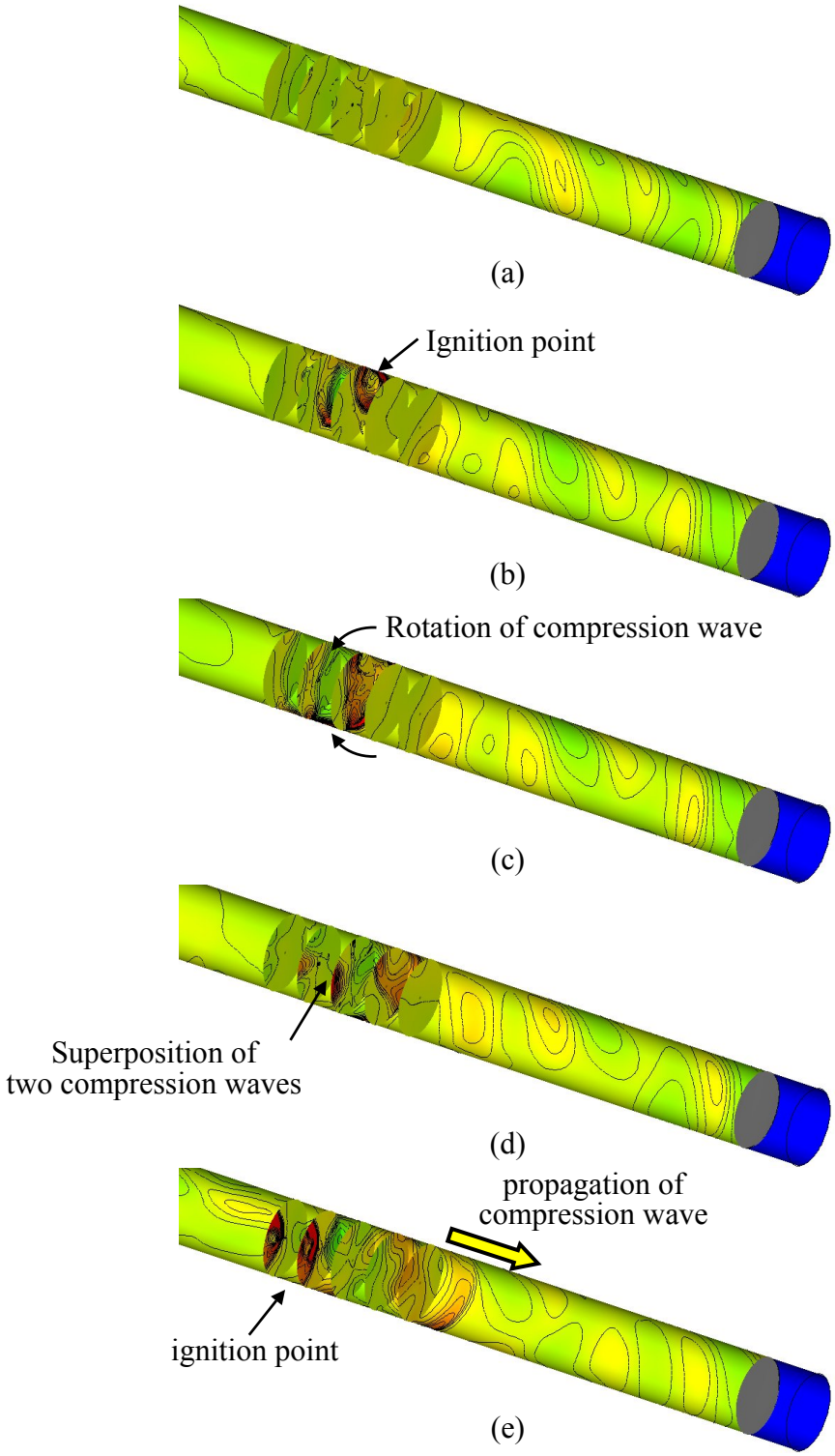

Fig. 2.9 Ten time-evolving instantaneous pressure distributions around local explosion in a circular tube.

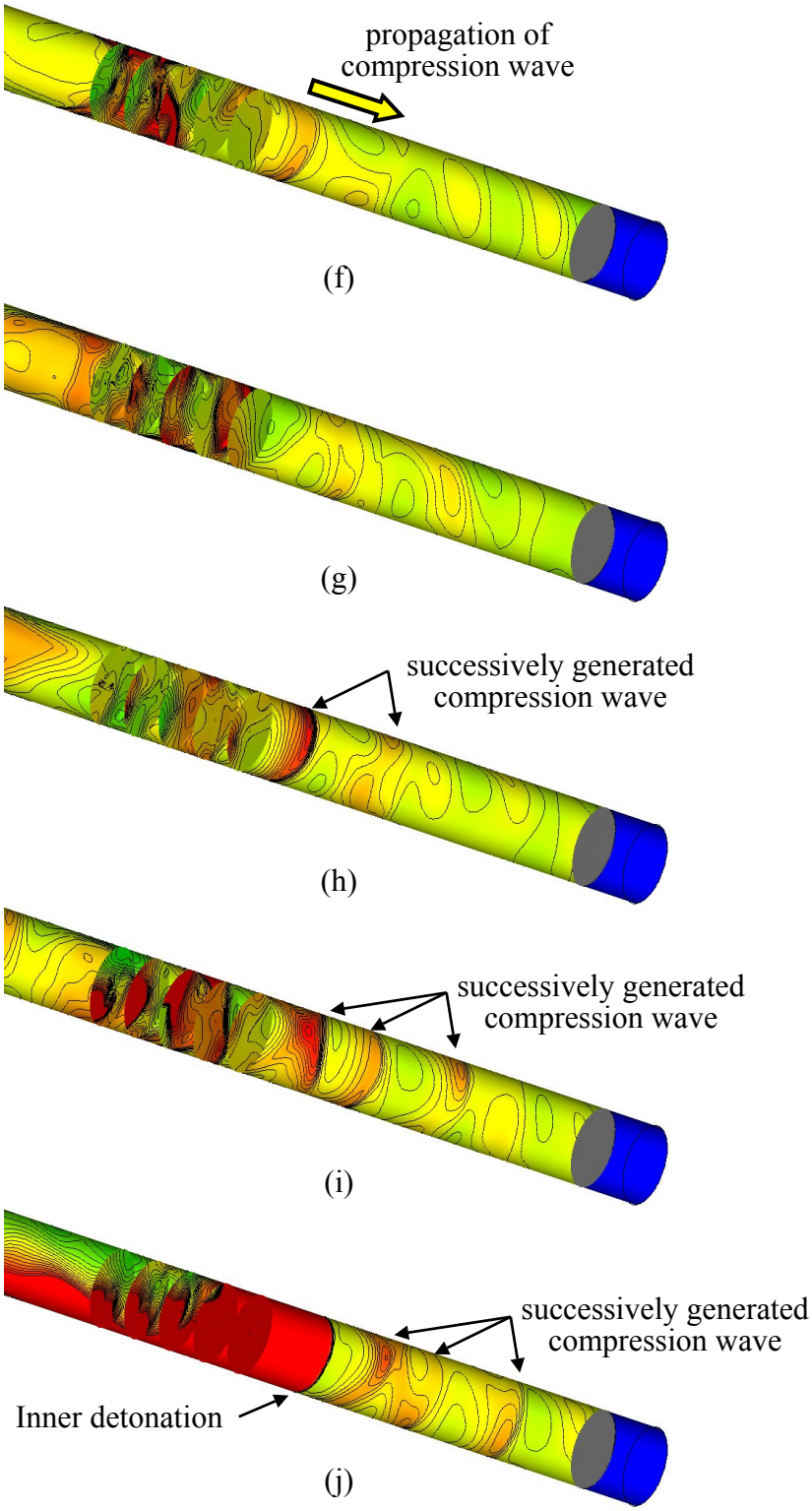

Fig. 2.9(cont.) Ten time-evolving instantaneous pressure distributions around local explosion in a circular tube.

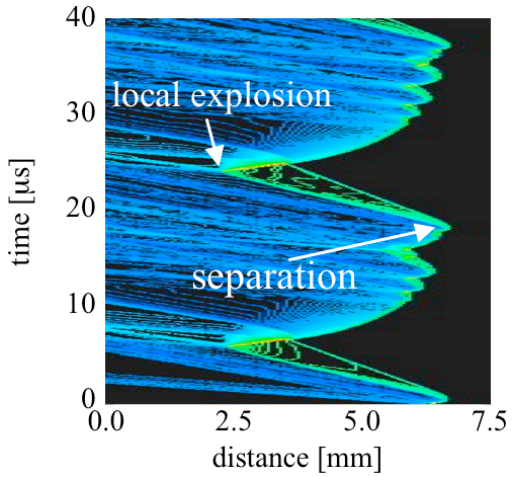

(a) One-dimensional detonation

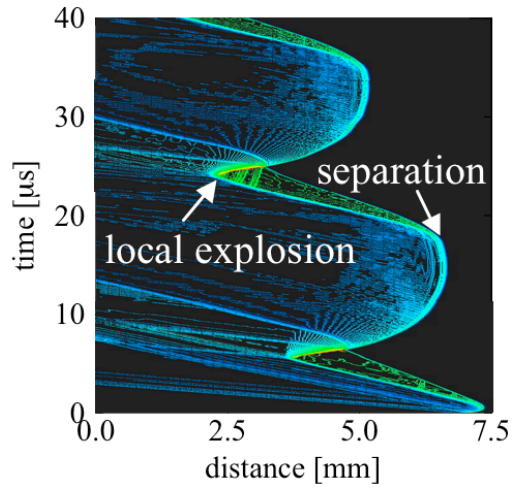

(b) Circular tube

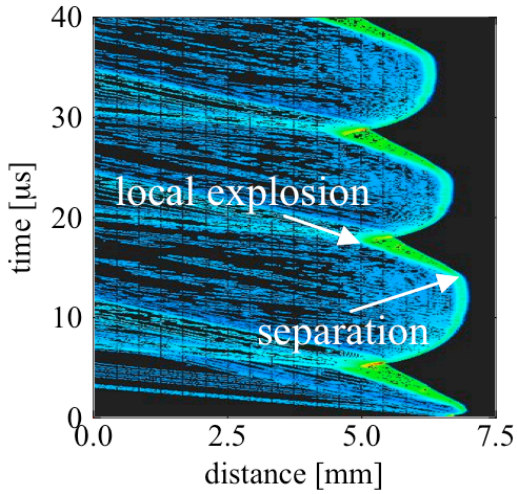

(c) Square tube

Fig. 2.10 *x-t* diagrams of density distribution by (a) one-dimensional detonation and cross-sectionally averaged *x-t* diagram of density distributions in (b) circular and (c) square tubes.

Chapter 3

Spinning detonations in circular and square tubes

3.1. Introduction

Shock structure of detonation is composed of incident shock wave, Mach stem and transverse waves which propagate perpendicular to the shock front. A few modes have been observed in detonation of circular tube such as spinning (single-headed), two-headed and multi-headed modes, and they are classified according to the number of transverse wave. Spinning detonation in circular tube, discovered experimentally in 1926 by Campbell and Woodhead [35] followed by a succession of papers by Campbell and Woodhead [36] and Campbell and Finch [37], is observed near detonation limit and the lowest mode that has only one transverse wave in a circumference direction, whereas two-headed detonation has two transverse waves along circumference and one transverse wave along a radius. Spinning detonation propagates helically on the wall, and transverse detonation rotates around the tube wall. It is also reported that the mean propagating velocity of spinning detonation is about 0.8 - 0.9D_{CJ}. A theoretical study by Fay [60] showed that the ratio of spin pitch to the tube diameter, 3.13, was derived from an acoustic theory. Its brief summary is described in Appendix E. The acoustic theory can explain the property of spinning detonation but cannot explain its structure. Schott [61] tried to understand the shock structure of spinning detonation, and they concluded that the shock front contains a complex Mach interaction. Voitekhovskii and his

co-workers [62] measured the Mach configuration by examining smoked disks attached to the end plate of the detonation tube. Their experimental observation says that shock front consists of a "leg" and one or two "whiskers." They also used the term "leg" as in "Mach leg." Topchian and Ul'yanitskii [63] investigated the instability of the spinning detonation and found three different types of pitch mode; stable pitch, periodical unstable pitch, and pitch covered with a cellular pattern. Huang *et al*. [64] tried to analyze the shock structure of spinning detonation using Rankine-Hugoniot relation and flow angle into incident shock wave, Mach stem and transverse detonation.

For detonations in a tube, the initial and boundary conditions play important roles for the propagation of detonation waves and for the limits where detonation waves fail. For small tubes, boundary layer introduces the heat and momentum losses that cause the detonation velocity deficits. Furthermore, the detonation wave will fail to propagate when the tube diameter is below a critical value. Diameter is important parameter to understand the effect of boundary layer. Theories for detonation limit with these losses have been developed in the past. Zel'dovich included heat and momentum loss terms in the equations for one-dimensional detonation and showed that the detonation velocity depends on losses [65] and diameter. Detonation limit should be considered with the boundary condition and instabilities of detonation. However, in numerical simulations, it is difficult to conduct three-dimensional calculations with full Navier-Stokes equations because of high grid resolution for boundary layer near the wall. Since the calculation with Euler equations can artificially eliminate the loss of heat and momentum, the effect of initial conditions, tube dimension and geometry could be

revealed in the simulations separately.

Chapter 3 clarifies the propagation behavior and stability of spinning detonation in circular and square tubes by three-dimensional numerical simulations and the effect of initial pressure P_1 and geometric length (diameter D of a circular tube and channel width L of a square tube) with Euler equations. The detailed discussion is carried out to explain the unsteady propagation behavior with time evolutions of the simulated results.

3.2. Numerical setup

The governing equations are the compressible and reactive two- and three-dimensional Euler equations with two-step reactions model by Korobeinikov *et al*. [14] as shown in Eqs. (2.1), (2.2), (2.3), (2.7), (2.8) and (2.9) and Eqs. (2.4), (2.5), (2.6), (2.7), (2.8) and (2.9) for three and two dimensions, respectively. The fluid is an ideal gas with constant specific heat ratio of 1.4, and all diffusive effects are neglected. The parameters of this model in the present work are listed in Table 2.1. Premixed gas is modeled as stoichiometric hydrogen-air. Initial pressure is chosen as a parameter (P_1 = 0.2, 0.6 and 1.0 atm), and initial temperature is fixed as T_1 = 293 K.

As discretization methods, Yee's Non-MUSCL Type 2nd-Order Upwind Scheme [56] is used for the spatial integration, and Point-Implicit Method that treats only source term implicitly is used for the time integration. The details of Yee scheme and Point-Implicit Method are described in Appendix A and B. Grid resolution is defined as the number of grid points in induction length L_{ind} calculated by one-dimensional steady solution. In Chapter 3, 17 grid points in induction reaction length L_{ind} are set in all directions,

respectively. Grid convergence study for detonation propagation is conducted in Appendix D, and grid resolution is determined by computational cost. In order to understand the effect of acoustic coupling in Sect. 3.3.1., two-dimensional channel calculation is conducted. The computational grid for channel flow is an orthogonal system. Initial pressure and channel width is fixed as P_1 = 1 atm and L = 5.8 L_{ind} (0.94 mm) The premixed gas velocity of incoming flow is 2000 m/s, which is slightly (about 3 %) overdriven with respect to CJ velocity in the present chemical parameters. Periodic boundary conditions are adopted for the lower and upper boundary conditions. The axial length in the computational grid is more than 500 L_{ind} to avoid disturbance from the outflow boundary proposed by Gamezo *et al.* [19].

In three-dimensional calculations, initial pressure P_1, channel width L and diameter D, are chosen as parameters. They are described in Fig. 2.2 and Table 2.3 for circular tube simulations and in Fig. 2.3 and Table 2.4 for square tube simulations. Initial condition and boundary conditions in circular and a square tubes are the same as those in Sect. 2.2.

3.3. Results and discussion

3.3.1. Acoustic coupling for the propagation of detonation

Before investigations of the propagation behavior of spinning detonation in circular and square tubes, I show that acoustic coupling plays an important role for the propagation of detonation. In this section, two-dimensional calculation is conducted. First, I

calculate the spinning detonation in the case of diameter D = 0.3 mm and initial pressure P_1 = 1.0 atm, respectively. In this condition, spinning detonation maintains its stable propagation. Using the physical values on the wall, two-dimensional calculation with periodic conditions at upper and lower boundaries are conducted in order to understand the importance of acoustic coupling between transverse wave and acoustic wave. This simulation shows the propagation of one-sided detonation with one transverse wave in a two-dimensional periodic boundary channel whose width L is 0.94 mm. Figure 3.1 shows the time variations of density distribution of two-dimensional calculation, and Fig. 3.1a shows the initial condition from the result on the wall of spinning detonation in a circular tube at initial pressure P_1 = 1.0 atm and diameter D = 0.3 mm. In Fig 3.1b to 3.1d, one-sided detonation propagates in two-dimensional channel with periodic boundary condition. After that, cellular detonation with two triple points appears and keeps stable propagation as shown in Fig. 3.1e. In the case of two-dimensional periodic channel, detonation cannot keep the one-sided propagation. Red and black arrows in Figs. 3.1b to 3.1d denote the positions of transverse wave and acoustic wave behind it, respectively. Time intervals between Figs. 3.1b and 3.1c and Figs. 3.1c and 3.1d are nearly constant at the one rotation of acoustic wave in the periodic boundary channel. Sound speed at CJ state a_{CJ} is calculated as

$$\frac{a_{CJ}}{D_{CJ}} = \frac{\gamma}{\gamma+1}\frac{\gamma M_{CJ}^2+1}{\gamma M_{CJ}^2} \approx \frac{\gamma}{\gamma+1}, \tag{3.1}$$

where M_{CJ} and γ are CJ Mach number and specific heat ratio, respectively. After restarting the calculation of two-dimensional periodic channel from the solution on the wall of the stable spinning detonation in a circular tube, long acoustic wave appears in Fig. 3.1b. The position of the transverse wave and the acoustic wave is in-phase in Fig. 3.1b but shifts to out-of-phase in Figs. 3.1c and 3.1d because the velocity of the transverse wave is faster than that of the acoustic wave. Acoustic theory says that acoustic wave behind transverse wave propagates at sound speed in CJ state in a two-dimensional channel. In the simulated case, the speed of the acoustic wave is 1197 m/s and agrees well with sound speed in CJ state (a_{CJ} = 1154m/s from Eq. (3.1)). Velocity of the transverse wave is 1589 m/s, which is much larger than that of the acoustic wave. Therefore, the transverse wave is located ahead of the acoustic wave in Figs. 3.1c and 3.1d. At Fig. 3.1d, a new disturbance propagating in the opposite direction of the transverse and the acoustic waves is generated and evolves into a new triple point as seen in Fig. 3.1e. When the coupling between transverse wave and acoustic coupling is not satisfied, the one-sided detonation cannot keep stable propagation in the two-dimensional periodic boundary channel. The above-mentioned simulations imply that the detonation propagation mechanism should be discussed with focusing on the acoustic coupling between transverse wave and acoustic wave.

3.3.2. Spinning detonations in a circular tube

Present calculations show three propagation modes, and they are discussed in 3.3.2.1., 3.3.2.2. and 3.3.2.3 from the viewpoint of acoustic coupling. After that, I discuss the

front structure of spinning detonation in a circular tube in 3.3.2.4.

3.3.2.1. Steady mode

This section shows the propagation behavior of steady mode. One condition (P_1 = 1.0 atm and D = 0.40 mm) is used to discuss the shock structure of steady mode since propagation behavior is essentially the same as other observed steady modes. Figure 3.2 shows (a) shock front, (b) density distribution on the wall and (c) exothermic reaction variable β on the wall of steady mode. Fay's acoustic theory [60] says that sound speed on the wall of circular tube is estimated as 2124m/s by Eqs. (3.1) and (3.2).

$$V_{acou} = 1.841 a_{CJ} \tag{3.2}$$

Present simulations in steady mode show that velocities of a wave behind transverse detonation are between $0.93V_{acou}$ and V_{acou} at various initial pressures P_1 and diameters D and agree with that by Fay's acoustic theory. Therefore, I describe the wave propagating in burned gas region as acoustic wave as shown in Fig. 3.2b. A white line as shown in Fig. 3.2c indicates the shock front on the wall. In the case of steady mode, shock front structure and physical distributions are independent of the time, and Fig. 3.2 shows representative images of steady mode. Mach leg that stands perpendicular to the wall exists on the shock front, and no whisker appears in Fig. 3.2a. Density distribution shows the transverse detonation on the wall, which completes the reaction of induction zone behind the shock wave in Fig. 3.2c. In the case of steady mode, acoustic wave,

connecting to the transverse detonation at the contact surface between burned and unburned gas, always keeps the rotation with transverse detonation in phase, which indicates that spinning detonation keeps stable propagation when coupling between transverse detonation and acoustic wave is always satisfied. Figure 3.3 shows the maximum pressure history on the wall imitating as the soot track images in the experiments. Black belt is the trajectory of transverse detonation on maximum pressure history, and the width of black belt is constant, which also denotes that detonation structure keeps the same shape. Track angle, α, is defined as arctangent of the pitch of the spin divided by length in circumference. The track angle in the experimental observation is about 45º under various experimental conditions, and the value is also derived by an acoustic theory as shown in Eq. (3.3).

$$\tan\alpha = 1.841\frac{a_{CJ}}{D_{CJ}} \tag{3.3}$$

where, a_{CJ} and D_{CJ} are sound speed at CJ state and CJ velocity, respectively. In present calculations, the simulated track angle in Fig. 3.3 is 46.9º, which agrees well with the theoretical one of 47.0º calculated by Eqs. (3.1) and (3.3). Figure 3.4 shows (a) the maximum pressure history of transverse detonation on the wall and (b) time history of detonation velocity. Pressures and velocities are normalized with respect to von Neumann spike of CJ condition of one-dimensional steady simulation and CJ velocity, respectively. Black line in Fig. 3.4b indicates a CJ velocity. Figure 3.4a shows that the

maximum pressure at transverse detonation is constant around $4.8P_{vN}$. Longitudinal velocity of steady mode is always constant at a CJ detonation velocity. I concluded that the spinning detonation in steady mode shows very stable propagation. Figure 3.5 shows schematics of shock structure of spinning detonation and definition of shock angle β, deflection angle θ and angle from triple point Θ on the wall. Huang *et al*. [64] conducted some experiments with two mixtures (H_2-O_2-Ar and C_2H_2-O_2-Ar) and tried to analyze the shock structure Their experiments showed track angle α and distribution of shock angle β_1. At Mach stem, shock angle β_1 becomes 90º, gradually decreases with increment of Θ and approaches around 30º. From experimental data, they investigated the shock structure of spinning detonation, which agrees with the analyzed data using Rankine-Hugoniot relation and flow angle into incident shock wave, Mach stem and transverse detonation. I also obtain the relation between flow angle β_1 and angle from triple point Θ on the wall as shown in Fig. 3.6. Present simulated data also shows that flow angle β_1 at Mach stem is 90º and approaches to 33 degrees. This analysis will be utilized in 3.3.2.3. from the viewpoint of the reason that transverse detonation fails and 3.3.2.4. from the viewpoint of the extent of Mach leg.

3.3.2.2. Unstable mode

Unstable mode is obtained when the diameter is smaller than that of steady mode as shown △ in Fig. 2.2 and Table 2.3. This section shows the propagation behavior of unstable mode, using the shock structure of one condition (P_1 = 0.2 atm and D = 2.25 mm). As unstable mode has periodicity during propagation of transverse detonation,

one cycle of unstable mode is used to explain the propagation behavior. Figure 3.7 is time evolutions of (a) the shock front from the front side, (b) density and (c) exothermic reaction variable on the wall. The moments A – E in Figs. 3.7a, 3.7b and 3.7c are the identical. A sequence in Figs. 3.7 schematically and quantitatively shows the generation and decay of the complex Mach interaction. The images of 'A' is almost the same as the images of 'E', and therefore the duration between 'A' and 'E' is the one cycle of unstable mode.

A series of events is explained, as follows with denotation in Fig. 3.7. (A) One Mach leg and two (front and rear in Fig. 3.7a) whiskers and complex Mach interaction are observed on the shock front. Transverse detonation completes the reaction of premixed gas behind the shock wave. Two acoustic waves 1 and 2 exist behind the transverse detonation in density distribution, and they connect with each other at the contact surface between burned and unburned gas. (B) Front whisker disappears because of the collision with the wall. Acoustic waves 1 and 2 are connected as acoustic wave 1' as shown in Fig. 3.7B-b and detaches from transverse detonation at contact surface between burned and unburned gas. In this moment, velocities of acoustic wave 1' and transverse detonation are 2104 m/s and 1951 m/s, respectively. Therefore, acoustic wave exists ahead of transverse detonation. This indicates that acoustic coupling between them is not satisfied. Large unreacted pocket between them is generated as shown in Fig. 3.7B-c. (C) The shock front structure is similar to that of 'B'. Unburned gas pocket becomes small because the second transverse detonation is generated and propagates to unburned gas pocket as shown in Fig. 3.7C-c. (D) Since the second

transverse detonation propagates in radial direction as well as in circumferential direction, it appears as a new whisker in the radial direction as shown in Fig. 3.7D-a, and the complex Mach interaction is generated. The unburned gas pocket is fully consumed by the second transverse detonation. Since no premixed gas exist in front of the second transverse detonation, a new acoustic wave 2', which is shifted from the second transverse detonation, appears. In this moment, velocities of acoustic waves 1' and 2' and transverse detonation are 2103 m/s, 2151 m/s and 2151 m/s, respectively. Transverse detonation is accelerated by the consumption of unburned gas pocket and catches up with the acoustic wave 1'. Acoustic coupling is satisfied between transverse detonation and acoustic waves 1' and 2'. This indicates that periodicity of unstable mode is caused by the periodic generation of the second transverse detonation. (E) Shock front structure is the same as that of moment (A). Since consumption of unburned gas pockets accelerates the transverse detonation, acoustic coupling between transverse detonation and acoustic wave is temporally satisfied in (A), (D) and (E). Compared with the steady mode, spinning detonation slightly becomes unstable due to the repetition of coupling and decoupling of transverse detonation and acoustic wave.

Figure 3.8 shows the maximum pressure history on the wall imitating the soot track images in the experiment. Black belt is the trajectory of transverse detonation on maximum pressure history. The width of black belt repeatedly becomes large and small, and its period is the same as that of the generation and decay of complex Mach interaction as shown in Fig. 3.8. Averaged track angle 47.6º agrees well with the theoretical value of 47.0º by Eq. (3.6). Figure 3.9 shows (a) the maximum pressure

history of transverse detonation on the wall and (b) time history of detonation velocity. Pressures and velocities are normalized with respect to von Neumann spike P_{vN} of one-dimensional steady simulation and CJ velocity D_{CJ}, respectively. Black line in Fig. 3.9b indicates a CJ velocity. The strength of transverse detonation periodically changes because of periodical generation of unburned gas pocket, transverse detonation and whisker, which induces the fluctuation of peak pressure in Fig. 3.9a. As calculation condition becomes lower initial pressure, spinning detonations become unstable and show the periodical propagation behavior. Longitudinal velocity of unstable mode shows fluctuation around a CJ velocity. Lee *et al.* [66] reported the velocity fluctuation near extinction limit and five modes of propagations; stable detonation mode, rapid fluctuations mode, stuttering mode, galloping mode and low-velocity stable mode (fast flame). Longitudinal velocity is constant near D_{CJ} at stable detonation mode, fluctuating around D_{CJ} at rapid fluctuation mode, periodically changes from $0.6D_{CJ}$ to D_{CJ} with repetition of failure and reignition at stuttering mode, and periodically changes from $0.4D_{CJ}$ to $1.5D_{CJ}$ with periodical local explosion at galloping mode and is constant near $0.5D_{CJ}$ at low-velocity stable mode, respectively. In the case of unstable mode, since the velocity fluctuation appears around CJ detonation velocity, it is classified as rapid fluctuation mode.

3.3.2.3. Pulsating mode

The details of propagation behavior of pulsating mode are described in Chapter 2. Here, I show the failure mechanism of spinning detonation with the viewpoint of acoustic

coupling between transverse detonation and acoustic wave behind it using one simulated condition (P_1 = 1.0atm, D = 0.20mm).

Figure 3.10 shows distributions of (a) the density and (b) exothermic reaction variable β on the wall at the moment of the failure of spinning detonation. White arrows and dashed lines denote the position of transverse wave and the acoustic wave, respectively. Moment (A) is used as reference time, and moments (B), (C) and (D) denote the density distribution after one, two and three rotations from moment (A), respectively. Although transverse detonation and acoustic wave are coupling at (A), they are decoupling, and acoustic wave is ahead of transverse detonation at (B) to (D). The velocity of acoustic wave is 2104m/s, which agrees well with that estimated by Fay's theory, whereas the velocity of transverse detonation is 1770m/s and much smaller than that of acoustic wave. Therefore acoustic coupling is not satisfied. Transverse detonation is suddenly decayed between (C) and (D). In the case of unstable mode, after decoupling of transverse detonation and acoustic wave, new transverse detonation is generated and consumes the unburned gas pocket, whereas, in the case of pulsating mode, transverse detonation decays as shown in (D) after collapse of acoustic coupling, and new transverse detonation is not generated. Disappearance of transverse detonation brings incomplete exothermicity, and eventually spinning detonation fails.

Figure 3.11 shows schematics of shock structure of spinning detonation without acoustic coupling on the wall. In the case of pulsating mode, since acoustic wave is faster than transverse detonation, acoustic wave is located in front of transverse detonation, and enters into unburned gas region behind incident shock wave as shown in

Fig. 3.10. Since the velocity of the acoustic wave (2104 m/s) is larger than sound speed of unburned gas, the acoustic wave becomes a secondary shock wave and physical values such as pressure and temperature discontinuously changes. Here, I analyze the effect of the secondary shock wave. I made some of assumptions below. These are: that track angle α is 45 degrees and Mach number into the leading shock wave is $\sqrt{2}\times M_{CJ}$ (=6.80); that shock angle at incident wave β_1 near triple point ($\Theta \sim 360^{\circ}$) is 34º as shown in Fig. 3.6; that transverse detonation angle β_3 in Fig. 3.5 is 90º if the secondary shock wave does not exist (This indicates that transverse detonation angle β_3 is simply estimated using the deflection angle θ_2 by the secondary shock wave and becomes 90 – θ_2 degrees); that the secondary shock angle is a function in this analysis. From the above assumptions, pressure, density and temperature and induction time after transverse wave without chemical reaction are calculated. Here, induction time is estimated by these values using the steady solution as Eq. (3.4). They are described red lines in Fig. 3.12a – 3.12d.

$$t_{ind} = \frac{1}{k_1 \rho_{tran} \exp\left(-\dfrac{E_1}{RT_{tran}}\right)} \tag{3.4}$$

In Fig. 3.12, left end of secondary shock angle denote the Mach angle of 19.2º and therefore, the values of left end in Fig. 3.12 are the same as those without the secondary shock wave. Right end of secondary shock angle is critical shock angle of 45.4º that Mach number after secondary shock wave becomes 1.0 and transverse detonation

cannot exist. As compared with induction time without (β_2 = 19.2º) and with the secondary shock wave (β_2 > 19.2º), Fig. 3.12d shows that chemical reaction is prompted at 19.2 < β_2 ≤ 36.5º and is inhibited at 36.5º < β_2 ≤ 45.4º. This indicates that it is possible that the secondary shock wave inhibits the chemical reaction after transverse detonation, and spinning detonation fails. Figure 3.13 shows relation between streamline and secondary shock wave angle β_2 on the wall (a) when transverse detonation maintains its rotation and (b) just before transverse detonation fails. When spinning detonation rotates, the flow is almost steady in a circumferential direction, and streamline is described in Fig. 3.13. Now, I focus on the red colored streamlines. Since the premixed gas experiences secondary shock wave, streamline is deflected. The secondary shock angle β_2 ~ 40º is observed, and transverse detonation can exist as shown in Fig. 3.12. However, it is supposed that chemical reaction is inhibited. After the moment at Fig. 3.13b, chemical reaction induced by transverse detonation is inhibited, and transverse detonation fails. Transverse detonation has an important role to maintain propagation of spinning detonation because it completes the potential exothermicity. Therefore, spinning detonation fails. Physical value changes by the secondary shock wave are very sensitive for the propagation of transverse detonation. This is to say that spinning detonation maintains its propagation at the condition that acoustic coupling is satisfied.

3.3.2.4. Mach leg in a radial direction

As discussed before, acoustic coupling with transverse detonation and acoustic wave in

circumferential direction has important role to keep the propagation of spinning detonation. I analyze the effect of acoustic coupling in radial direction using the acoustic theory and the extent of Mach leg. Ul'yaniskii [67] carried out experimental measurements and proposed an extent of the Mach leg of 0.5*R*. Voitsekhovskii *et al.* [62] reported that the extent of the Mach leg was 0.6*R* and that his experiments show a uniform spinning detonation. Tsuboi *et al.* [39] showed that the extent of the Mach leg changes between 0.2 and 0.5*R*. Here, I discuss the transverse detonation attached coordinate as shown in Fig. 3.5.

It is assumed that acoustic coupling between transverse detonation and acoustic wave on the wall. In the shock front described in Fig. 3.2a, the velocity V_{tran} of the transverse wave and Mach leg in circumferential direction at radius r is calculated by Eq. (3.5) from Fay's acoustic theory.

$$V_{tran} = 1.841 a_{CJ} \frac{r}{R} \tag{3.5}$$

where, a_{CJ} is the sound speed at CJ state, and R is radius of a tube, respectively. Therefore the velocity of premixed gas entering into incident shock wave is a function of r/R as

$$V\left(\frac{r}{R}\right) = \sqrt{D_{CJ}^2 + \left(1.841 a_{CJ} \frac{r}{R}\right)^2}\,. \tag{3.6}$$

Figures 3.14 shows the relation between distance from tube axis r/R, incident shock angle β_1 and Mach number M_1 into incident shock wave. Incident shock angle β_1 decreases with increasing r/R. Figure 3.15 denotes the $d\beta_1/d(r/R)$ and it suddenly increases at r/R = 0.4. Using Rankine-Hugoniot relation, sound speed a_2 and Mach number M_2 behind incident shock wave are calculated as shown in Fig. 3.16. Although sound speed a_2 behind incident shock wave shows sudden change at r/R = 0.40 due to discontinuous change of $d\beta_1/d(r/R)$, it becomes nearly constant value around 790 m/s. Mach number M_2 behind incident shock wave becomes always larger than 1.0 and linearly increases by r/R because the velocity of premixed gas entering into incident shock wave also increases by r/R. Figure 3.17 shows circumferential distributions of density and reaction progress variables at various radii r. As r/R becomes small, transverse detonation decays and unburned gas pocket behind transverse wave is observed at $r = 0.2R$, $0.4R$ and $0.6R$. Figure 3.18 shows distributions of (a) density and reaction progress variables at surface "A" described in Fig. 3.17. White dotted and dashed lines denote r/R = 0.40 and 0.56, respectively. In Fig. 3.18, transverse detonation rotates in a circumferential direction at $0.56 \leq r/R \leq 1$ because reaction front attaches with it. On the other hand, at $0.40 \leq r/R \leq 0.56$, transverse wave, which does not induces chemical reaction, is observed. When r/R is smaller than approximately 0.40, no transverse wave is observed in Fig. 3.18. Here, I discuss the reason that transverse wave disappears at $r/R < 0.40$ from the movement of disturbance. Figure 3.19 shows the schematic pictures of propagation of small disturbance into uniform flow at (a) subsonic, (b) sonic and (c) supersonic conditions. Symbol 0 (●) indicates a generated point of

disturbance at $t = 0$, and symbols 1, 2 and 3 denote the position of the generated point, which propagates with the velocity of uniform flow u, after $t = \Delta t$, $2\Delta t$ and $3\Delta t$, respectively. Numbers i, ii and iii denotes the propagating disturbance with the sound speed a at $t = \Delta t$, $2\Delta t$ and $3\Delta t$, respectively. Generally, only when flow is supersonic ($u \geq a$), shock wave can be generated because the effective region is limited inside Mach cone, and disturbance can be accumulated. Therefore, sonic condition of M = 1 is important parameter to discuss the shock wave. In the case of disturbance propagating in a circumferential direction in circular tube, it rotates $1.841a$ from acoustic theory, which is faster than sound speed a. This indicates that only when the Mach number in a circular tube is larger than 1.841, shock wave can be generated. Figure 3.20 shows Mach number M_2 of premixed gas behind incident shock wave. Red line indicates $M_2 = 1.841$. M_2 is smaller than 1.841 at $r/R < 0.40$, and therefore, shock wave rotating in a circumferential direction cannot be generated. As shown in Fig. 3.18, transverse wave vanishes at $r/R < 0.40$ and agrees with the present data estimated from $M_2 \leq 1.841$. Mach number behind incident shock wave may be important parameter to discuss the shock wave rotating in a circular tube. Since Mach leg is a line of triple points and connects with transverse wave, extent of Mach leg is equivalent to that of transverse wave at $r/R = 0.40$ from acoustic theory in a circular tube.

3.3.3. Spinning detonations in a square tube

As detailed propagation behavior of spinning detonation in a square tube is essentially the same as that at the previous paper by Tsuboi *et al.* [34], this section focuses on the

propagation behavior for a square tube with the viewpoint of acoustic coupling between transverse detonation and acoustic wave between walls.

3.3.3.1. Propagation behavior

Propagation behavior is essentially different between spinning detonations in circular and square tubes. Spinning detonation in a circular tube shows that transverse detonation always rotates on the wall as shown in Fig. 3.2a. Figure 3.21 shows the quarter cycle of shock front from the front side. Two triple lines that are parallel and orthogonal to the sidewalls emanate from the shock front and move partially out of phase. Focused on the intersection zone of two triple lines, it reflects walls at an angle of 45 degrees and seems to rotate on the shock front. Therefore, spinning detonation in a square tube shows that transverse detonation collides with the wall repeatedly and that intersection zone between two triple lines makes spinning detonation.

In order to show the difference of spinning and pulsating modes, I used two conditions; P_1 = 1.0 atm, L = 0.40 mm for spinning mode and P_1 = 1.0 atm, L = 0.32 mm for pulsating mode. In the case of pulsating mode, spinning detonation does not keep the propagation but transiently appears as well as the pulsating mode in a circular tube. Figures 3.22 and 3.23 show the one cycle of density distribution on the wall at spinning and pulsating modes, respectively, and their images denote the moments at which transverse detonation collides on (a) wall AB, (b) wall BC, (c) wall CD and (d) wall DA. White lines and arrows denote the corners of the square tube and the position of acoustic wave that is generated by the collision with top corner A and transverse

detonation at Figs. 3.22a and 3.23a, respectively. In the case of spinning mode, the transverse detonation couples with acoustic wave, which reflects between corners A and D, at the moment of collision with wall AD as shown in the white arrow at Fig. 3.22d. They propagate to corner A together. Transverse detonation always couples with acoustic wave propagating between corners and re-couples with different one in every reflection on walls. This indicates that acoustic coupling with transverse detonation and acoustic wave is always satisfied on walls and that spinning detonation can keep stable propagation. In the case of pulsating mode, acoustic wave reflecting corners denoted by white arrow at Fig. 3.23d propagates to corner D. After Fig. 3.23d, acoustic wave collides with transverse detonation. They are not coupled with each other. After Fig. 3.23d, transverse detonation collides with acoustic wave. This indicates that coupling between transverse detonation and acoustic wave is not satisfied.

3.3.3.2. Acoustic coupling on walls

Spinning detonation in a square tube shows that transverse detonation collides with the wall repeatedly and that interaction between two triple lines makes spinning detonation. Therefore, transverse detonation and acoustic wave traveling between walls are schematically discussed. Figure 3.24 shows schematic pictures of (a) fully coupling, (b) barely coupling at the corner A and (c) no coupling with the transverse detonation projected on walls and acoustic wave. Red, blue and black arrows are trajectories of intersection point of two triple lines, transverse detonation projected on walls and acoustic wave at wall AD. Figures 3.24a and 3.24c correspond to Figs. 3.22 and 3.23.

The moment that transverse detonation collides on the wall AB is used as the reference time, and plots (●) denotes the start point of trajectory of transverse detonation. Here, I discuss the acoustic coupling between acoustic wave (black arrows) and transverse detonation projected on walls (blue arrows). Acoustic wave caused by the reflection with the wall AB is generated at the reference time and propagates back and forth between corners A and D. In the case of Fig. 3.24a, acoustic wave connects with the transverse detonation at the moment of its collision with the wall AD. After that, transverse detonation propagates with acoustic wave. In the case of Fig. 3.24b, acoustic wave barely connects with the transverse detonation just before the collision with transverse detonation and the wall AB. And then, this denotes the limit case to satisfy the acoustic coupling. In the case of Fig. 3.24c, acoustic wave collides with transverse detonation at the wall AD.

Acoustic theory says that acoustic wave behind transverse wave propagates at sound speed in CJ state in a square channel. The horizontal component of the velocity of transverse detonation in order to keep the propagation is as

$$1.75a_{CJ} \le V_{tran} \le 2.00a_{CJ}. \tag{3.7}$$

where upper and lower limit is calculated by Figs. 3.24a and 3.24b.

Using Eqs. (3.1) and (3.7), track angle $\alpha = \tan^{-1}(V_{tran}/D_{CJ})$ is derived as ($\gamma = 1.4$)

$$45.6^{\circ} \le \alpha \le 49.4^{\circ}. \tag{3.8}$$

Table 2.4 shows that maximum track angle is 49.4º and that spinning detonation cannot keep the propagation in case that track angle is smaller than 45.6º. This indicates that the acoustic coupling between transverse detonation and acoustic wave on the wall is also important to discuss the propagation behavior of spinning detonation in a square tube as well as in a circular tube.

3.4. Summary

Spinning detonations in circular and square tube at various initial pressures are numerically investigated using three-dimensional Euler equations with a two-step chemical reaction model proposed by Korobeinikov *et al* [14].

Spinning detonation in a circular tube, two distinct propagation modes are obtained namely steady mode, unstable mode. Steady mode shows stable propagation without change in the shock structure. The maximum pressure history of transverse detonation on the wall and velocity history of detonation remained nearly constant, and a Mach leg always existed on the shock front and rotated at a constant speed. Coupling with transverse detonation and acoustic wave is always satisfied. Meanwhile, unstable mode shows periodical change in the shock structure. Complex Mach interaction periodically appears due to periodical generation of transverse detonation. Its velocity history shows the fluctuation, which qualitatively agrees with that of rapid fluctuation mode by Lee *et al*. Coupling and decoupling with transverse detonation and acoustic wave is repeated, which induce the periodical flow field. In the case of pulsating mode, spinning

detonation cannot keep its propagation due to decoupling of acoustic wave and transverse detonation. In order to discuss the physics of transverse detonation in a radial direction, I analyze the effect of acoustic coupling in radial direction using the acoustic theory and the extent of Mach leg. Acoustic theory says that transverse wave and Mach leg can rotates in a circumferential direction when Mach number behind incident shock wave is larger than 1.841.

In the case of square tube, maximum and minimum track angle in order to keep the propagation of spinning detonation in a square tube is analyzed from the viewpoint of acoustic coupling between transverse detonation projected on walls and reflecting acoustic wave. Present results show that acoustic coupling with transverse detonation and acoustic wave traveling between walls is also important to keep the propagation as well as in the case of circular tube.

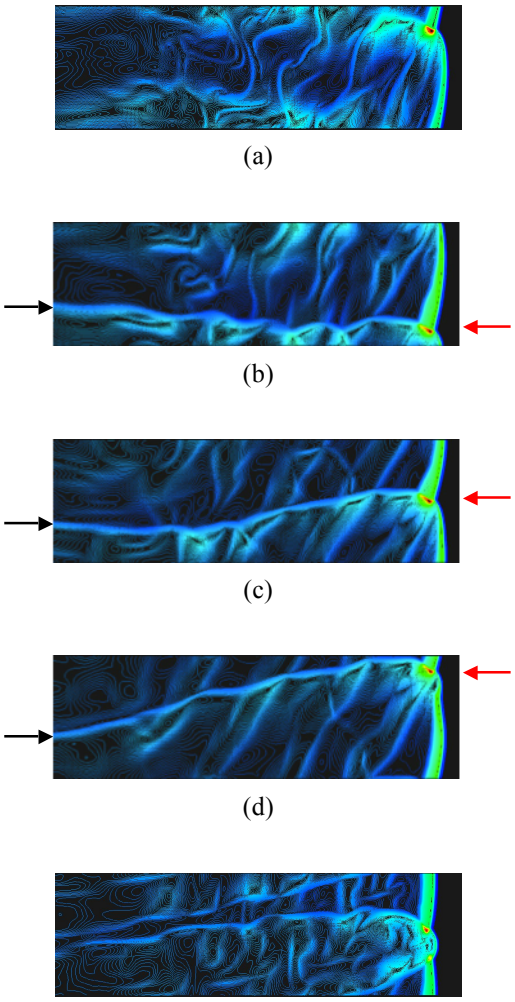

Fig 3.1 Time variations of density distribution in two-dimensional channel with periodic condition at upper and lower boundaries. (a) initial condition, (b) – (d) propagation of one-sided detonation and (e) cellular detonation with two triple point shifted from one-sided detonation.

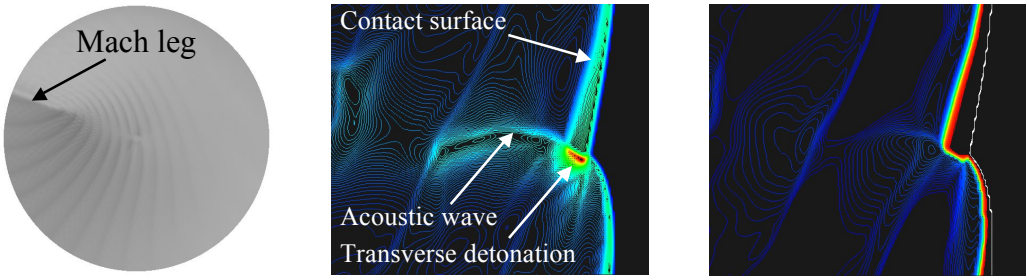

(a) Shock front (b) Density (c) Exothermic reaction valuable

Fig. 3.2 (a) shock front, (b) density distribution on the wall and (c) exothermic reaction variable on the wall in the case of steady mode.

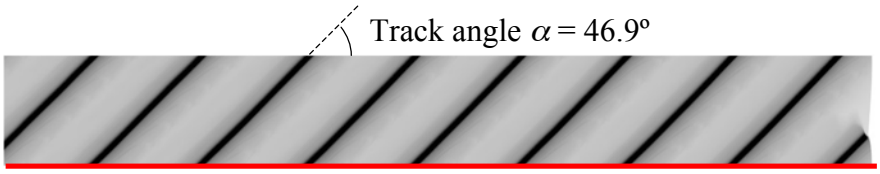

Fig. 3.3 The maximum pressure history on the wall in the case of steady mode.

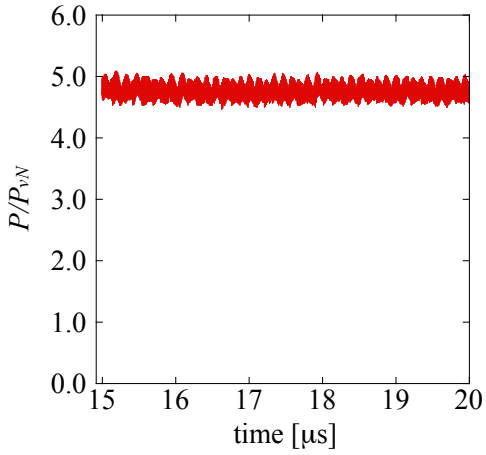

(a) Maximum pressure history on transverse detonation

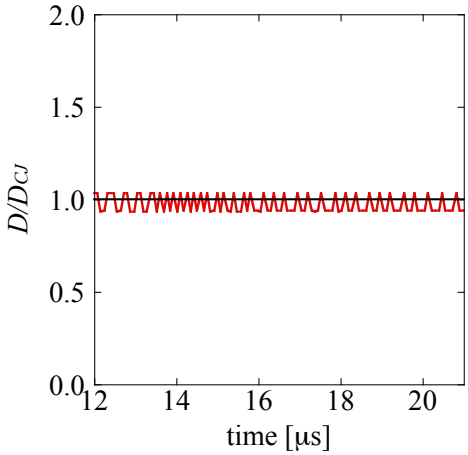

(b) Time history of detonation velocity

Fig. 3.4 (a) the maximum pressure history of transverse detonation on the wall and (b) time history of detonation velocity.

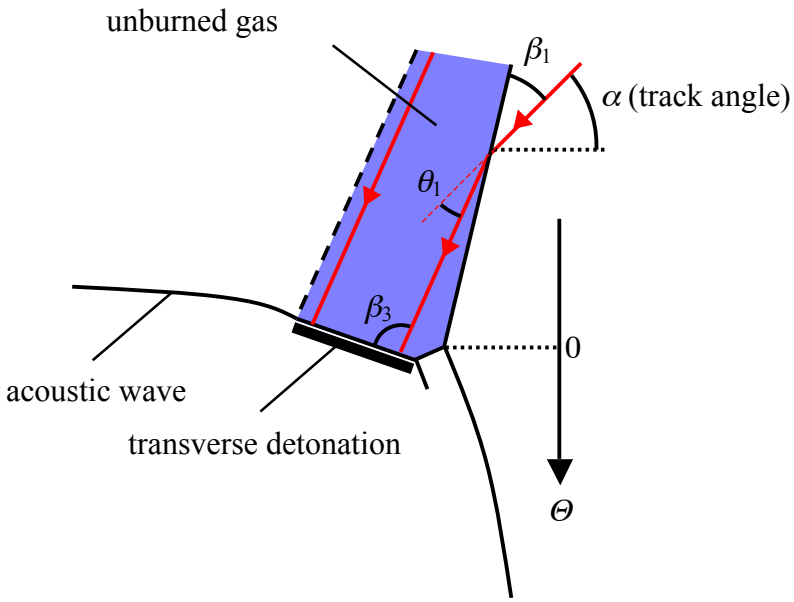

Fig. 3.5 Schematics of shock structure of spinning detonation and definition of shock angle β, deflection angle θ and angle from triple point Θ on the wall.

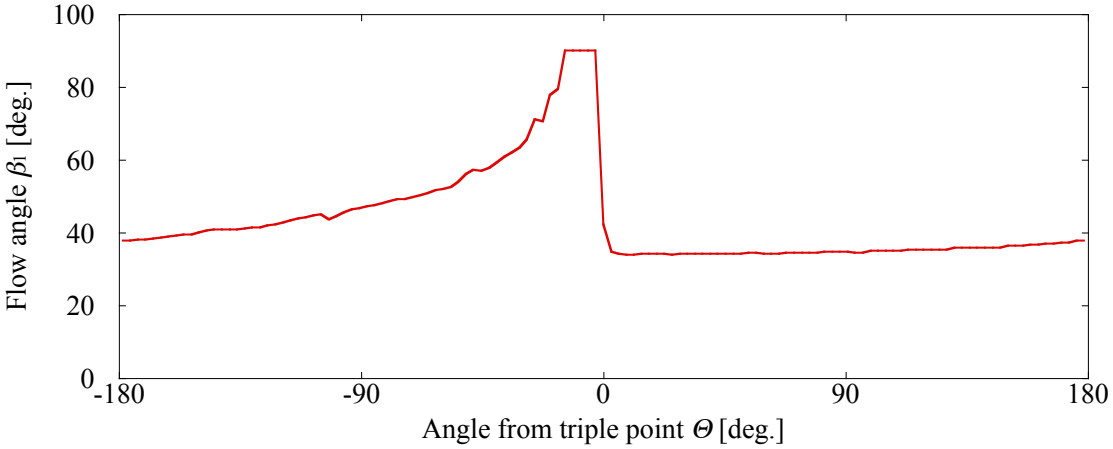

Fig. 3.6 Relation between flow angle β_1 and angle from triple point Θ on the wall.

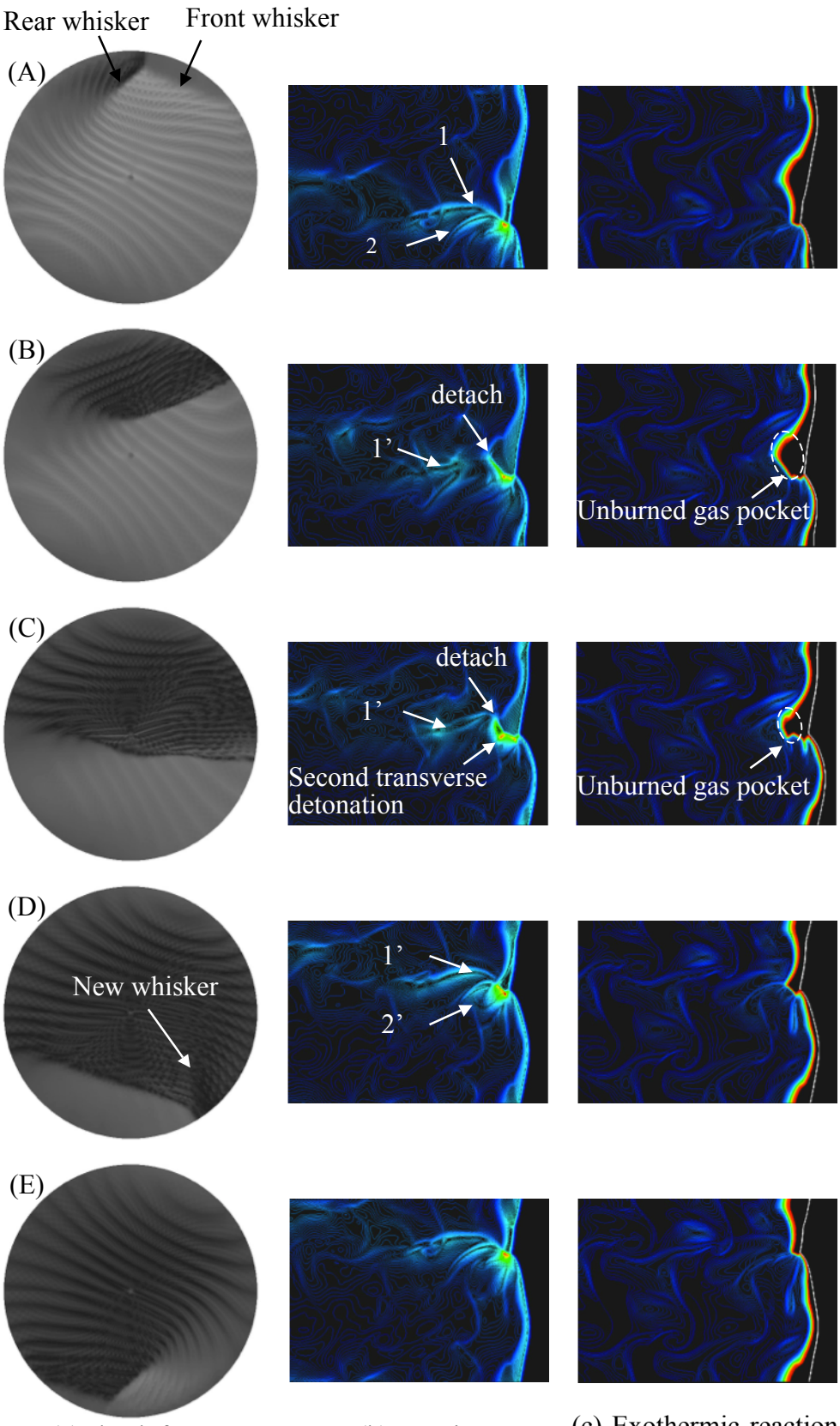

Fig. 3.7 Time evolutions A - E of (a) the shock front from the front side, (b) density and (c) exothermic reaction variable on the wall.

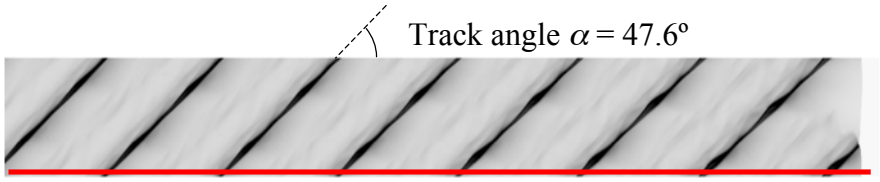

Fig. 3.8 The maximum pressure history on the wall in the case of unstable mode.

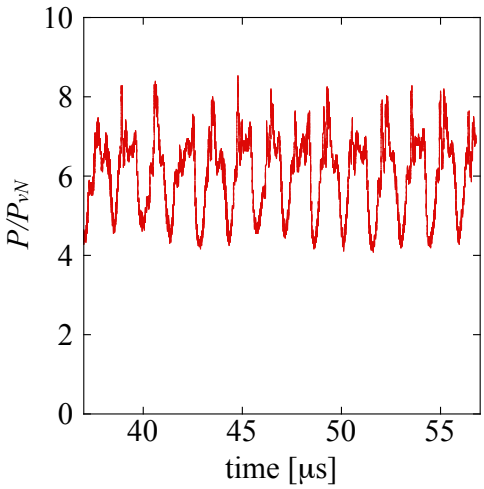

(a) Maximum pressure history of transverse detonation

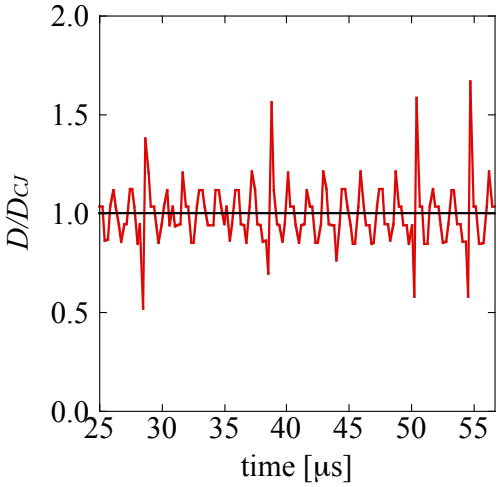

(b) Time history of detonation velocity

Fig. 3.9 (a) the maximum pressure history of transverse detonation on the wall and (b) time history of detonation velocity.

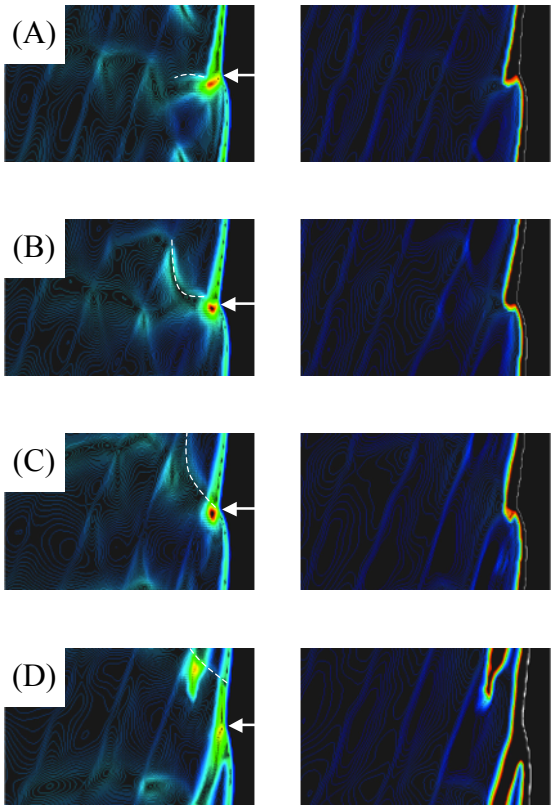

Fig. 3.10 Instantaneous distributions of (a) the density and (b) exothermic reaction variable on the wall at the moment of the failure of spinning detonation. White arrows and dashed lines denote the position of transverse wave and the acoustic wave, respectively.

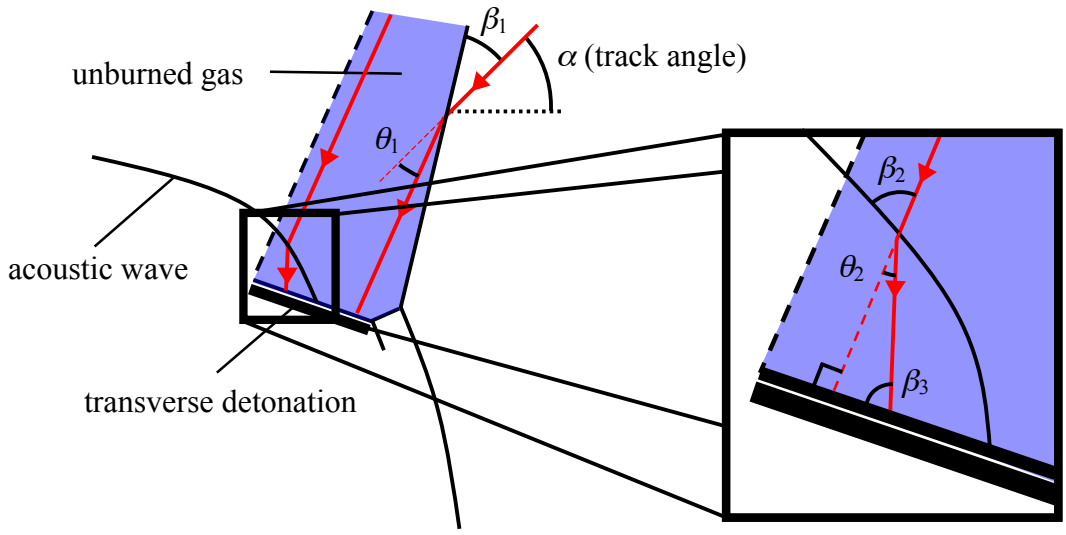

Fig. 3.11 Schematics of shock structure of spinning detonation without acoustic coupling on the wall.

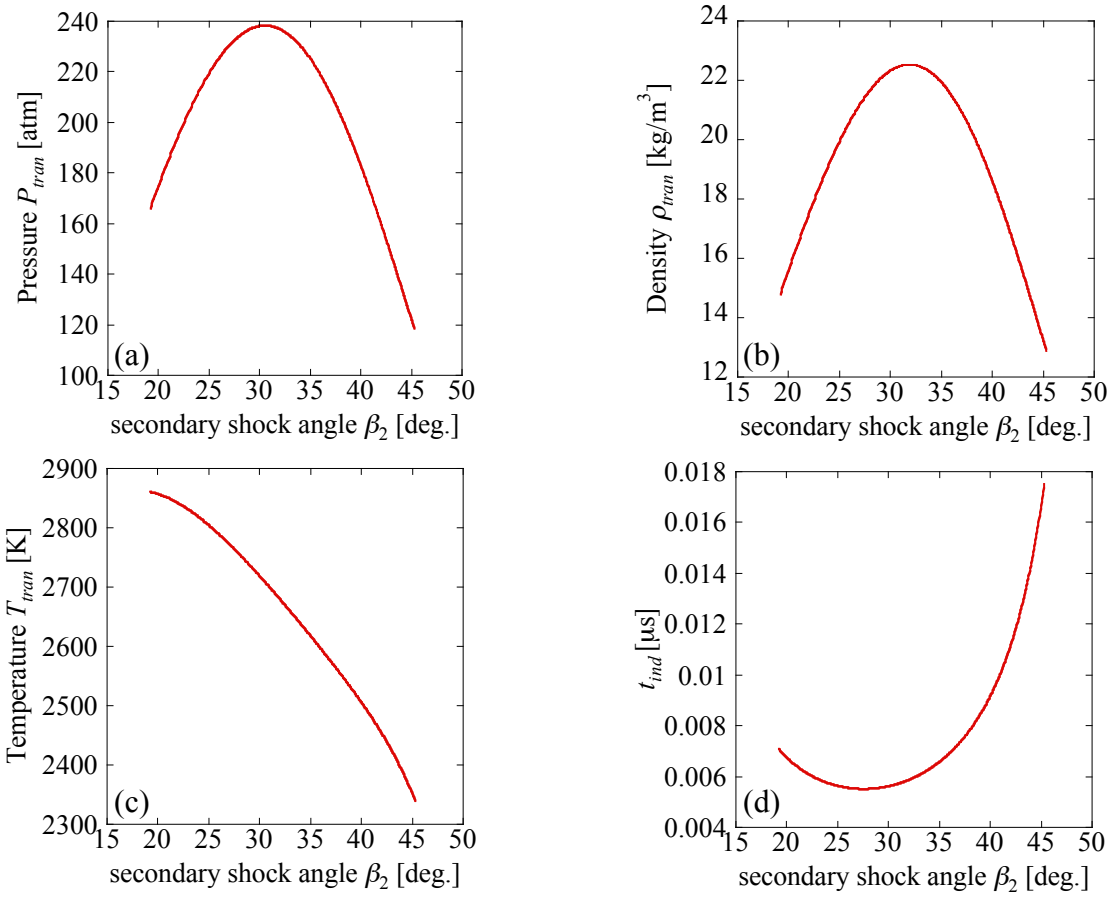

Fig. 3.12 (a) pressure, (b) density, (c) temperature and (d) induction time. Left and Right ends of the secondary shock angle β_2 indicate Mach angle and the critical shock angle that Mach number after the secondary shock wave becomes 1.0.

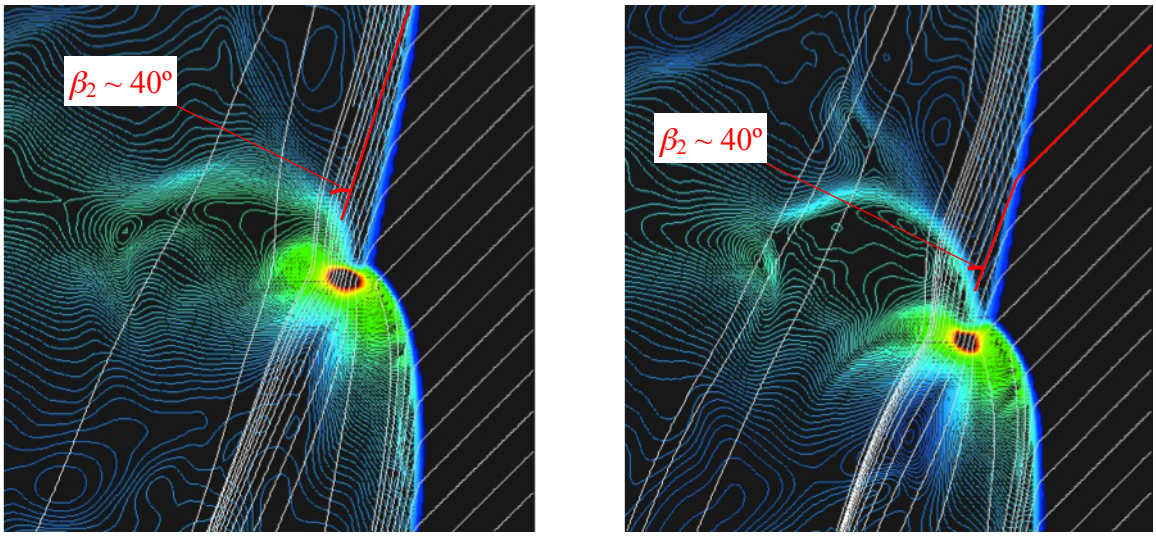

(a) (b)

Fig. 3.13 Relation between streamline and secondary shock wave angle β_2 on the wall (a) when transverse detonation maintains its rotation and (b) just before transverse detonation fails.

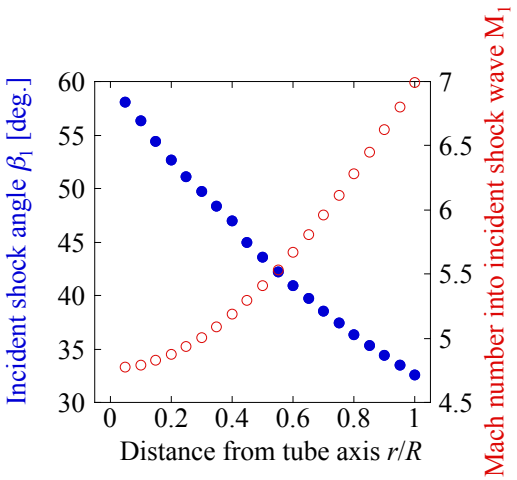

Fig. 3.14 Relation between distance from tube axis r/R, incident shock angle β_1 and Mach number into incident shock wave M_1.

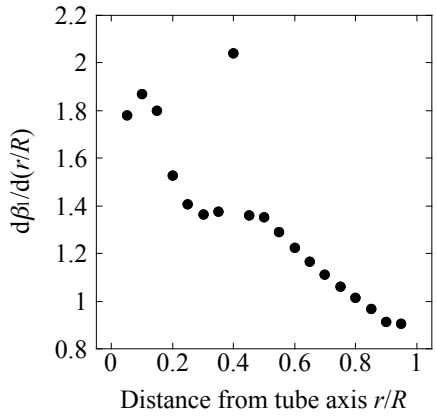

Fig. 3.15 Relation between $d\beta_1/d(r/R)$ and distance from tube axis r/R.

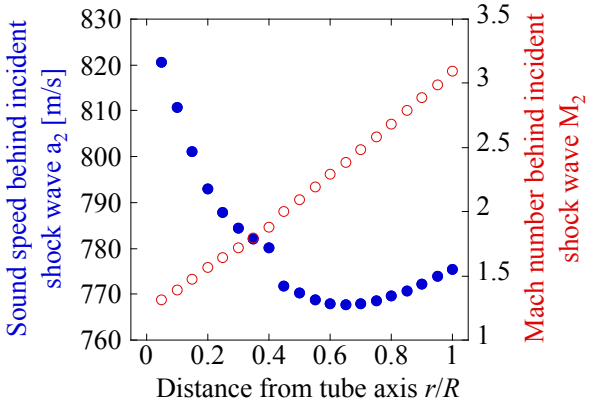

Fig. 3.16 Relation between distance from tube axis r/R, sound speed a_2 and Mach number M_2 behind incident shock wave.

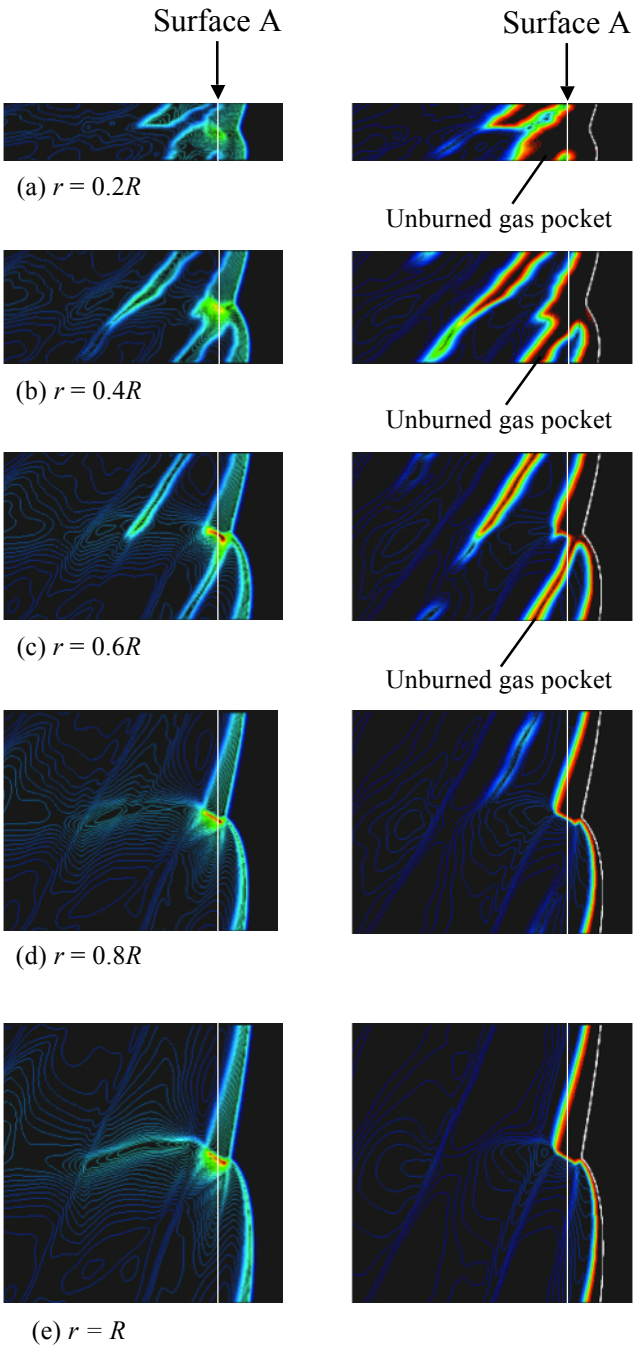

Fig. 3.17 Circumferential distributions of density and reaction progress variables at various radii r. White lines in (b) denote shock fronts.

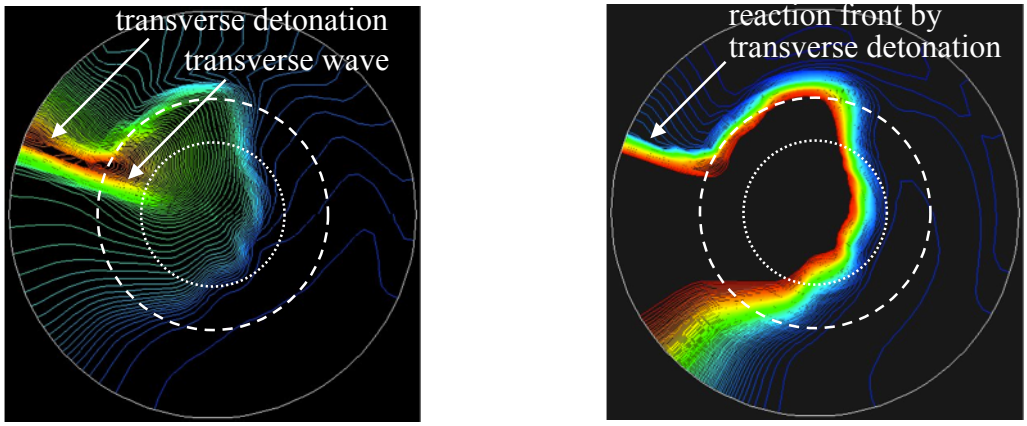

(a) density (b) mass fraction of reactant

Fig. 3.18 Distributions of (a) density and (b) mass fraction of reactant at surface "A" described in Fig. 3.17. Radius r/R of dotted and dashed circles are 0.40 and 0.56, respectively.

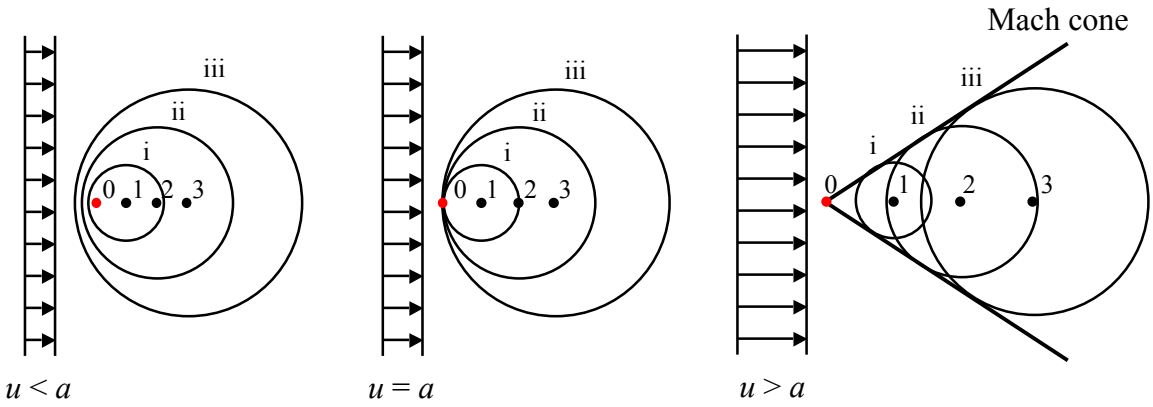

(a) subsonic (b) sonic (c) supersonic

Fig. 3.19 Propagation of small disturbance into uniform flow at (a) subsonic, (b) sonic and (c) supersonic conditions, respectively. Symbol 0 (●) indicates a generated point of disturbance at t = 0, and symbols 1, 2 and 3 denote the position of the generated point after time = Δt, $2\Delta t$ and $3\Delta t$. Numbers i, ii and iii denotes the propagating disturbance at time = Δt, $2\Delta t$ and $3\Delta t$.

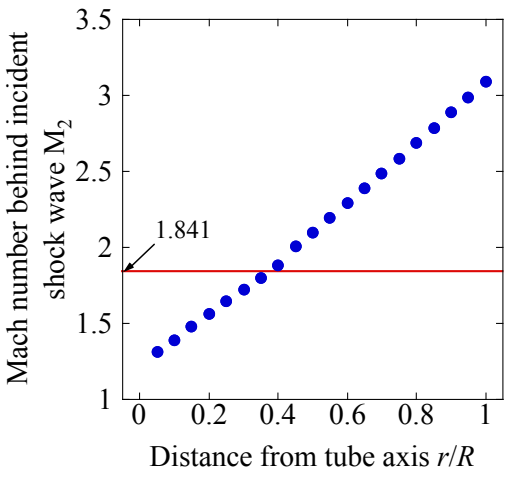

Fig. 3.20 Relation between Mach numbers behind incident shock wave and distance front tube axis r/R.

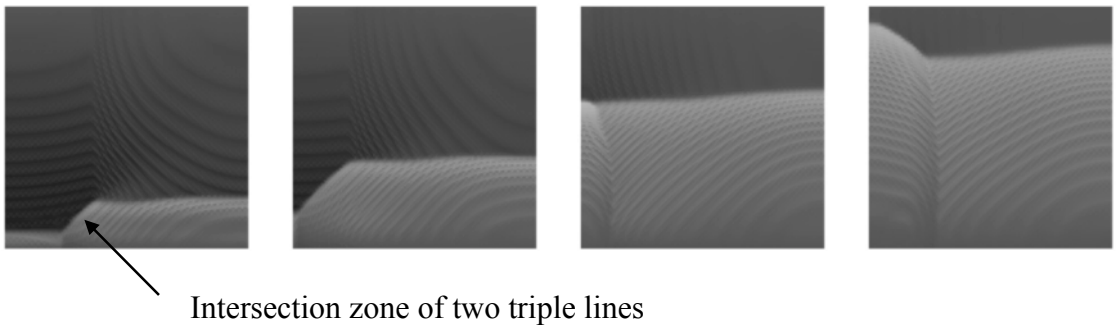

Fig. 3.21 Quarter cycle of shock fronts from the front side of spinning detonation in a square tube.

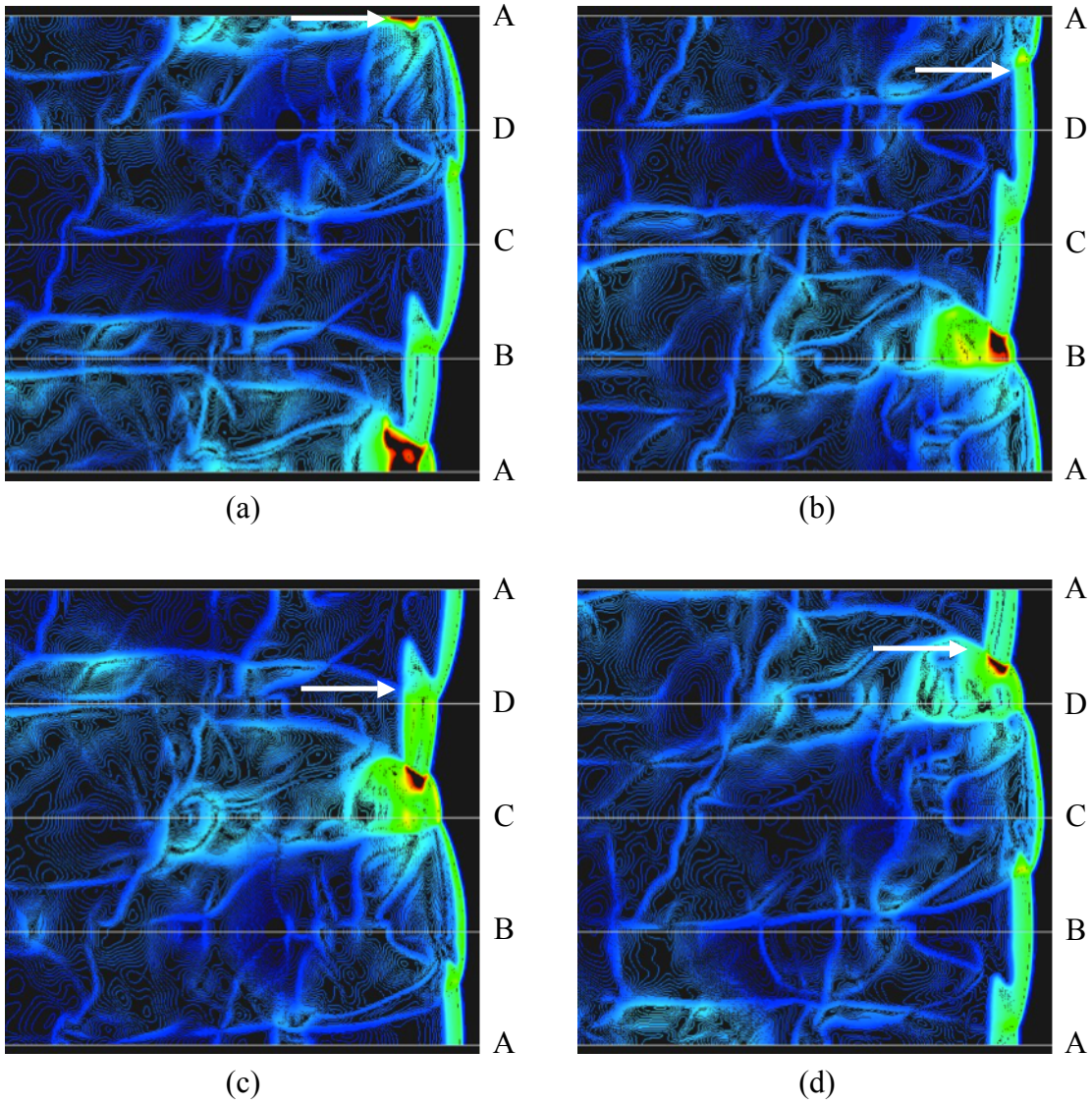

Fig. 3.22 One cycle of density distribution on the wall at spinning mode.

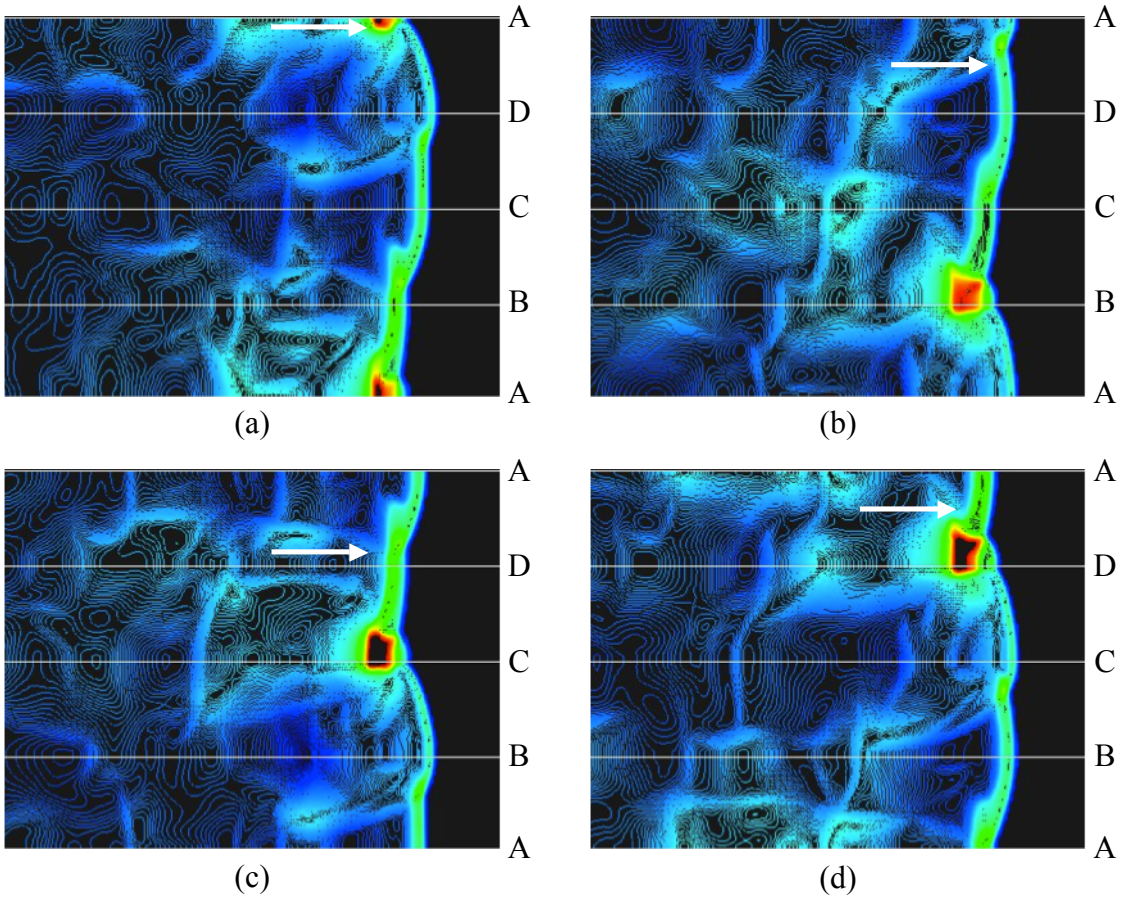

Fig. 3.23 One cycle of density distribution on the wall at pulsating mode.

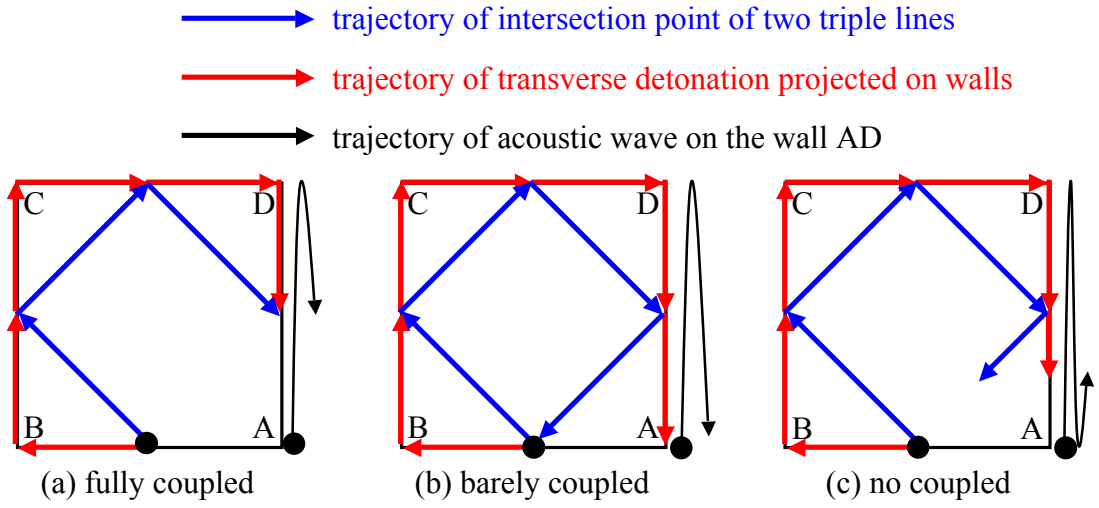

Fig. 3.24 Schematic pictures of (a) fully coupling, (b) barely coupling at the corner A and (c) no coupling with the transverse detonation and acoustic wave. Blue, red and black lines are trajectories of intersection point of two triple lines, transverse detonation projected on walls and acoustic wave at wall AD, respectively.

Chapter 4

Curved detonations in a two-dimensional curved channel

4.1. Introduction

In recent years, significant results were obtained by a detailed research on the concept of Pulse Detonation Engine (PDE) that creates thrust by burning the fuel in a combustion chamber where a detonation wave is periodically initiated and propagates [44, 45, 68-70]. However, it seems difficulties of fast exhaust of the combustion products, recharging of the combustion chamber with fresh combustible gases in high frequencies in order to obtain full efficiency. The Rotating Detonation Engine (RDE) is a new type of continuous detonation engine in which detonation always maintains its propagation in a circumferential direction of annular combustor, and unlike the PDE, it does not have to initiate a detonation many times in a second. Once detonation is initiated, it keeps its propagation in a circumferential direction of annular chamber with automatically recharging of fresh combustible gas. RDE provides a stable thrust, and therefore it may be an attractive to engineers as a new propulsive device [46, 47]. Some numerical simulations are conducted to reveal the characteristics of detonation in RDE [71 – 74]. However, they mainly investigated propagation behavior by two-dimensional calculations in circumferential and longitudinal directions and by three-dimensional calculations. However, a width of annular combustion chamber is too narrow to

investigate the three-dimensional effect such as diffraction and accumulation effects from inner and outer walls on a radial direction in three-dimensional calculations. It is evident that the circumferential velocity of detonation wave near the outer wall should be higher than that near the inner wall if angular velocity of detonation in a circumferential direction is constant. When self-sustaining detonation propagates with CJ velocity, it should have an oblique shock front relative to incoming premixed gas flow. Moreover, as a circumferential velocity of detonation rotating in annular combustion chamber linearly increases with the distance from its axis, self-sustaining detonation front should be curved in order to maintain a CJ oblique detonation front at each radius. For the practical use of RDE, propagation behavior of detonation with the effect in radial direction should be revealed. Several experimental and numerical studies in a curved channel have been performed [75-81] for the effect of diffraction and accumulation effects in a curved channel. However, the curved channel used in previous study is limited in a circumferential direction around 180°. Previous results [75-78] showed unsteady features just after detonation waves enters into curved section. By contrast, only a few studies of steady detonation waves in a curved channel [79-81] have been conducted. In a large channel, Kudo *et al.* [79] and Nakayama *et al.* [80, 81] discussed the stable propagation condition and shock front structure in curved detonations at some kinds of premixed gas composition in the curved channel that is limited in a circumferential direction around 180°. They showed that propagation mode is classified by the ratio of inner radius and cell width R_{in}/λ. In a large R_{in}/λ, curved detonation steadily propagates in a two-dimensional curved channel, which indicates

that detonation is not affected by the diffraction effect from the inner wall. As the R_{in}/λ decreases, a collapse of the detonation cell structure occurs, and detonation seems to be reinitiated after the generation of the strong transverse detonation at a certain point of shock front and its reflection at the inner wall. This indicates that diffraction effect from inner wall affects the detonation propagation and tends to make detonation decay. However, there are no concluding results that R_{in}/λ and channel widths L are so small that diffraction effect from inner wall becomes a dominant role in detonation propagation.

In order to reveal the self-sustaining propagation mechanism of detonations in a curved channel, I simulate curved detonations in a two-dimensional curved channel that continues at least 2 rounds in a circumferential direction in order to obtain fully developed two-dimensional curved detonations. The aim of Chapter 4 is to clarify the effect of the size of curved channel and the stable detonation limit. Here, I will show two series of calculations. One is described in Sect. 4.3. as that channel width L is equivalent to 0.5λ (λ: simulated cell width obtained in Chapter 2) and that the ratio of outer and inner radii R_{out}/R_{in} is chosen as a parameter in order to understand curvature effect of two-dimensional curved channel. I show the characteristics of steady detonation depending on the curvature of curved channel. The other is described in Sect. 4.4. as that the ratio of outer and inner radii R_{out}/R_{in} is fixed as 1.5 and 2 and that inner radius normalized by cell width R_{in}/λ is chosen as a parameter in order to understand the size effect. I show the characteristics of unstable and stable detonation propagation depending on the size of curved channel.

4.2. Numerical Setup

The governing equations are the same as those used in Chapter 3. The details of the compressible and reactive two-dimensional Euler equations with two-step reactions model by Korobeinikov *et al*. [14] as shown in Eqs. (2.4), (2.5), (2.6), (2.7), (2.8) and (2.9). The parameters of the chemical reaction model in the present work are listed in Table 2.1. Premixed gas is modeled as stoichiometric hydrogen-air. Initial pressure and temperature are fixed as P_1 = 1.0 atm and T_1 = 293 K, respectively.

As discretization methods, Yee's Non-MUSCL Type 2nd-Order Upwind Scheme [56] is used for the spatial integration, and Point-Implicit Method that treats only source term implicitly is used for the time integration. The details of Yee scheme and Point-Implicit Method are described in Appendix A and B. Grid resolution is defined as the number of grid points in induction length L_{ind} calculated by one-dimensional steady solution. 17 and 9 grid points in induction reaction length L_{ind} are set in all directions for calculations in Sects. 4.3. and 4.4., respectively. Grid convergence study for detonation propagation is conducted in Appendix D, and grid resolution is determined by computational cost. Figure 4.1 shows an example of the computational grids and initial conditions in the case of the ratio of outer and inner radii R_{out}/R_{in} = 3. Computational grid is composed of the straight and curved channel regions. In a straight tube region, more than 200 times of induction zone length of CJ detonation L_{ind} is set to avoid disturbance from the outflow boundary, which is proposed by Gamezo *et al.* [19]. Inner and outer wall boundaries are adopted to adiabatic and slip conditions. I confirmed that the dependency of initial condition is small for observation of fully developed flows in a

curved region. Therefore, the results of one-dimensional steady simulation of CJ condition are used as an initial condition, and initial shock front is located at joint of straight and curved channels. After a detonation wave enters into curved channel, diffraction from inner wall makes detonation weak, and curved front appears. Reaction front separates from leading shock front. Accumulation from outer wall generates Mach reflection, and Mach stem stands perpendicular to the outer wall and rotates in a circumferential direction. I describe the above results in Appendix D in order to compare with experimental results. In Chapter 4, fully-developed detonation in a two-dimensional curved channel is discussed. Figure 4.2 shows calculation parameters of the ratio of outer and inner radii R_{out}/R_{in} and channel width L/λ (λ; simulated cell width obtained in Chapter 2). In Sect. 4.3., I simulated the propagation of detonation in a small curved channel in order to understand the effect of the ratio of outer and inner radii R_{out}/R_{in}. In Sect. 4.4., the effect of channel width L/λ is investigated in a small R_{out}/R_{in} of 1.5 and 2.

4.3. Fully developed detonation structures in two-dimensional small curved channel

Parameter in Sect. 4.3. is the ratio of outer and inner radii R_{out}/R_{in}. Channel width L is equivalent to 0.5λ (λ; simulated cell width obtained in Chapter 2). I simulate various values of R_{out}/R_{in} between 2 and 17, and general characteristics of fully developed detonation structures in two-dimensional curved channels are discussed in 4.3.1. After that, in 4.3.2., the shock front structures are discussed in detail using Whitham theory

[82] and three-shock theories with and without chemical reaction to determine the shock front shape and position of triple point observed in 4.3.1.

4.3.1. Propagation behavior of steady detonation

The effect of the ratio of outer and inner radii R_{out}/R_{in} is described in this section. Specific features of steady detonation in a small curved channel are described using the observation of a series of figures below. Figure 4.3 indicates the definition of shock angle ω, the angle from the reference line θ and the normal detonation velocity D_n. Figures 4.4 – 4.7 show time-evolving three snapshots A – C of (a) density ρ and (b) mass fraction of reactant β in cases of R_{out}/R_{in} = 2, 3, 6 and 9 when detonations in the two-dimensional curved channel are fully developed. Red lines in Fig. 4.4 – 4.7 denote heads of wave that density becomes 1.01 times larger than that of upstream condition. Figure 4.8 denotes superimposed pictures of instantaneous shock fronts at (a) R_{out}/R_{in} = 2, (b) R_{out}/R_{in} = 3 (c) R_{out}/R_{in} = 6 and (d) R_{out}/R_{in} = 9. Shock fronts described as 4.4A – 4.4C, 4.5A – 4.5C, 4.6A – 4.6C and 4.7A – 4.7C in Fig. 4.8 correspond to those at A – C in Figs. 4.4, 4.5, 4.6 and 4.7, respectively. As R_{out}/R_{in} increases, shock front spreads in a circumferential direction between inner and outer walls. Soot tracks on the tube wall were recorded in previous experimental studies [11] and showed remarkable insight for the propagation mechanism of detonations. I show the soot track images using the maximum pressure histories and traces of triple points are described in Fig. 4.9 in cases of (a) R_{out}/R_{in} = 2, (b) R_{out}/R_{in} = 3 (c) R_{out}/R_{in} = 6 and (d) R_{out}/R_{in} = 9. Dark regions show high-pressure region and denote trajectories of transverse wave. Figure 4.10 shows

instantaneous density distributions of (a) R_{out}/R_{in} = 2, (b) R_{out}/R_{in} = 3 (c) R_{out}/R_{in} = 6 and (d) R_{out}/R_{in} = 9 at various radii R in the moment of Figs. 4.4C, 4.5C, 4.6C and 4.7C. Solid and dashed lines indicate that radius R is located at Mach stem and incident wave, respectively. In the present results, since detonation velocities in a circumferential direction are almost constant at each R_{out}/R_{in} case, I use time-averaged Mach number of incoming flow in a circumferential direction at (a) center of channel $R = (R_{out}+R_{in})/2$, (b) inner wall $R = R_{in}$ and (c) outer wall $R = R_{out}$ in shock-attached coordinate in Fig 4.11. Blue line in Fig. 4.11b indicates Mach number 1.0. As R_{out}/R_{in} increases, Mach number at $R = (R_{out}+R_{in})/2$ asymptotically approaches to 3.8, whose value is smaller than CJ one of 4.81, and Mach numbers at $R = R_{in}$ and $R = R_{out}$ gradually tends to decrease and increase, respectively. In Fig. 4.11b, Mach numbers at $R = R_{in}$ is smaller than 1.0 when R_{out}/R_{in} is larger than 7. When a shock wave without chemical reaction enters into a curved channel, a curved shock gradually becomes weak by the diffraction effect from inner wall, and Mach number at $R = (R_{out}+R_{in})/2$ continue to decrease. However, in the present simulations, chemical reaction supports the propagation of detonation waves with a certain steady Mach number as shown in Fig. 4.11a. I use above figures in order to discuss fully developed detonations in a two-dimensional curved channel.

In the case of R_{out}/R_{in} = 2, shock front generally stands perpendicular to walls as well as that propagating in a straight tube. Mach number in a circumferential direction linearly becomes larger with increasing distance from R = 0, and Mach numbers are 3.06 and 6.12 at inner and outer walls, respectively. Density discontinuously increases by shock wave in Fig. 4.10a. Since Mach stem stands perpendicular to walls, shock fronts in all

radius R described in Fig. 4.10a are located in angle difference θ_{in} - $\theta \sim 0$ deg. Since induction length strongly depends on Mach number, reaction front attaches to shock front near outer wall, whereas, reaction front detaches from shock front near inner wall as shown in Fig. 4.4b. The zig-zag chemical reaction zone, which is caused by the reflection of compression wave at inner and outer walls, appears behind shock front. Chemical reaction intermittently occurs in the zig-zag chemical reaction zone, and generated compression wave affects the shock front and reflects on inner and outer walls. This induces periodical change of shock front shape as shown in Fig. 4.8a, and makes cellular-like pattern in Fig. 4.9a. The complex interaction of chemical reaction in zig-zag chemical reaction zone and shock front structure is observed.

When a plane shock has oblique surface, two types of reflection are possible: regular reflection in which the incident and reflected shocks meet on the reflecting surface such as a wall, and Mach reflection in which the incident and reflected shock intersect at triple point and transverse wave is observed. In the case of $R_{out}/R_{in} = 3$, Mach reflection structure is observed, and a triple point is located around $R = 1.53R_{in}$ as shown in Fig. 4.8b. At inner and outer walls, Mach numbers are 2.06 and 6.18. Density discontinuously increases by shock wave in Fig. 4.10b. Since Mach stem stands perpendicular to outer wall, shock fronts at $R = 1.5R_{in}$, $2R_{in}$. $2.5R_{in}$ and $3R_{in}$ is located the same angle difference θ_{in} - $\theta \sim 10$ deg. Incident shock angle ω_i and Mach number of incident shock wave at triple point ($R = 1.53R_{in}$) are 55º and 3.16. As calculated from the above data, Mach number of premixed gas behind incident shock wave is 1.23, and therefore, transverse wave from the triple point is too weak to be observed in Fig. 4.5a.

Soot track image shows a trace of the weak transverse wave described as a blue arrow of Fig. 4.9b in a circumferential direction. Reaction front attaches with shock front near outer wall as shown in Fig. 4.5b. As well as in the case of $R_{out}/R_{in} = 2$, zig-zag chemical reaction zone and intermittently generated compression wave are observed, and the compression waves periodically propagate from outer to inner walls. However, it weakens near inner wall because of stronger diffraction effect from inner wall than that in the case of $R_{out}/R_{in} = 2$. The reflection of compression wave from inner wall is not observed as shown in Fig. 4.9b, and shock front almost keeps the same shape. The above described zig-zag chemical reaction zone is well observed in the simulated cases of $R_{out}/R_{in} \leq 5$ because there exist a region that reaction front separates from shock front near Mach stem as shown in Figs. 4.4a and 4.5a.

In the case of $R_{out}/R_{in} = 6$, Mach reflection structure is observed, and a transverse wave and a triple point is observed around $R = 4.44R_{in}$ in Fig. 4.8c. Soot track image also shows a trace of a transverse wave as shown in Fig. 4.9c. At inner and outer walls, Mach numbers are 1.12 and 6.73. Density discontinuously increases by shock wave in Fig. 4.10c. Since Mach stem stands perpendicular to outer wall, shock fronts at $R = 4.75R_{in}$ and $6R_{in}$ is located the same angle difference $\theta_{in} - \theta \sim 135$ deg. Mach number of incident shock wave at triple point ($R = 4.44R_{in}$) is overdriven value of 4.98. Zig-zag chemical reaction zone are observed in Fig. 4.6c. Intermittent compression wave generated at zig-zag chemical reaction zone affects the width of high-pressure region, which denotes the structure of transverse wave, changes periodically as shown in Fig. 4.9c. However, overall shock front structure keeps almost the same as shown in Fig.

4.8c. At Mach stem, reaction front attaches with shock front, and overdriven detonation without a cellular structure steadily propagates in a circumferential direction.

In our simulations, Mach number of incoming flow in a circumferential direction of shock-attached coordinate at inner wall becomes smaller with increasing R_{out}/R_{in}, and is below 1.0 in cases of $R_{out}/R_{in} \geq 7$ as shown in Fig. 4.11b. Flow structures in cases of $R_{out}/R_{in} \geq 7$ show the similar one in the case of $R_{out}/R_{in} = 9$. Therefore, I only show the result in the case of $R_{out}/R_{in} = 9$ as a reference data. In the case of $R_{out}/R_{in} = 9$, the simulated results are similar to that of $R_{out}/R_{in} = 6$. Mach reflection structure, a trace of transverse wave and intermittent compression wave generated from zig-zag chemical reaction zone are observed in Figs. 4.7, 4.8d and 4.9d. At inner and outer walls, Mach numbers are 0.752 and 6.77. Since Mach number of incoming flow is subsonic near inner wall $R \sim R_{in}$, compression wave generated by chemical reaction can propagate upstream of detonation front. However propagating compression wave becomes weak because of diffraction effect, and therefore, its effect is limited in the present simulation. In the case of incident wave at $R = 3R_{in}$ and $5R_{in}$ in Fig. 4.10d, Mach number of incoming flow is supersonic, but density continuously increases. This indicates that incident wave becomes weak by diffraction effect and is continuous compression wave. Whereas, at $R = 7R_{in}$, it discontinuously increases by shock wave. This indicates that characteristics of incident wave are dependant on distance R. Mach number in circumferential direction at triple point $R = 7.40R_{in}$ is calculated as an overdriven value of 5.49, and Mach stem propagates as an overdriven detonation without cellular structure. At Mach stem, reaction front attaches with shock front, and overdriven

detonation without a cellular structure steadily propagates in a circumferential direction. Difference from the simulated data of R_{out}/R_{in} = 6 is that Mach number at inner wall is smaller than 1.0. Unlike cases of R_{out}/R_{in} = 2, 3, and 6 as shown in Figs. 4.10a – 4.10c, incident wave near inner wall becomes weak due to the diffraction effect from inner wall, and density shows continuous increases by incident wave. In cases of $R_{out}/R_{in} \geq 7$, steady overdriven detonation at Mach stem without cellular structure, and continuous compression wave at incident wave near inner wall are observed.

4.3.2. Theoretical discussion of shock front structure and the position of triple point

In cases of $R_{out}/R_{in} \geq 3$, a shock front contains Mach reflection with curved incident shock wave. I discuss its characteristics in detail using Whitham theory [82] and three-shock theories with and without chemical reaction. Whitham theory [82] is an approximate treatment that gives information on the shape of a diffracting shock wave. It ignores the perturbed region and outer wall behind the shock wave. Since, kinematic relations are written in characteristic form, it is adapted only when Mach number is larger than 1.0. The predictions of shock front shape by Whitham theory [82] have been very successful and have been applied to a variety of situations, including the diffraction of shock wave over a curved arc. Skews [83] investigated the two-dimensional diffraction of a shock wave over a wall made up of a series of plane and/or curved sections. His experimental results say that the radius of arc has no apparent effect on the overall shock shape for a given Mach number, and that shock

angle does not depend on R/R_{in}. Therefore, I show distributions of shock angle between inner and outer walls focusing on (a) $3 \leq R_{out}/R_{in} \leq 7$ and (b) $8 \leq R_{out}/R_{in} \leq 17$ as described by color lines in Fig. 4.12 whose horizontal axis represents R/R_{in}. Shock angles are calculated by the density isosurface of 1.01 times larger than that of upstream condition. Its range is determined by that Mach number in circumferential direction at inner wall is larger or smaller than 1.0 in (a) and (b), respectively. Incident wave and Mach stem are separated by a triple point at which causes a sudden increase of shock angle ω as shown in Fig. 4.12. A line by Whitham theory [82] in Fig. 4.12a is also described in order to discuss shock angle theoretically. In cases of Fig. 4.12a, the profiles of shock angle between inner wall and triple point follow the unique one as well as experimental results by Skews [83]. However, distribution of shock angle is different between the simulated data and Whitham theory because the theory ignores the perturbed region and the effect of outer wall behind the wave. Skews also referred its importance such as terminator and slipstream as described in Fig. 10 of Ref. 82. In cases of $R_{out}/R_{in} \geq 8$ when Mach number in a circumferential direction at inner wall is smaller than 1.0, the profile of shock angle in Fig. 4.12b depends on R/R_{in}, and therefore, the characteristics of incident wave differs from that in cases of $R_{out}/R_{in} \leq 7$. This indicates that the knowledge from shock dynamics without chemical reaction is also adapted to those with chemical reaction only when Mach number at inner wall is larger than 1.0. Figure 4.13 shows shock angles focusing on $R_{out}/R_{in} \geq 8$, and distance R is normalized with respect to $(R-R_{in})/(R_{out}-R_{in})$. Shock angles are well characterized by distance $(R-R_{in})/(R_{out}-R_{in})$. Figure 4.14 shows the relation between shock angles and Mach

number in a circumferential direction. Mach angle $\theta_M = \sin^{-1}(1/M)$, is also described in Fig. 4.14 and good agreement with shock angles near inner wall as shown in Fig. 4.14. Figure 4.10d shows continuous increase of density near inner wall, which indicates that continuous compression waves from weakest (Mach wave) to some strong waves are observed from the head of wave described as dashed lines near inner wall ($R = R_{in}$, $3R_{in}$ and $5R_{in}$) in Fig. 4.10d. Therefore, shock angle ω at incident wave near inner wall agrees well with Mach angle θ_M. As the distance $(R-R_{in})/(R_{out}-R_{in})$ increases, the head of wave becomes stronger, and shock angle distribution departs from and becomes larger than Mach angle θ_M. In the case that Mach number of incoming flow in a circumferential direction of shock-attached coordinate at inner wall is below 1.0, Mach angle $\theta_M = \sin^{-1}(1/M)$ and distance $(R-R_{in})/(R_{out}-R_{in})$ are important factor to decide shock front angle near inner wall.

Figure 4.15 shows schematic pictures of three shock intersections at a triple point (a) without and (b) with chemical reaction. In order to obtain an analytical solution of the three-shock configuration, I made some of assumptions below. These are: that the three shocks can be considered as planar close to the triple point; that Mach number of uniform flow in a circumferential direction is constant at that of a triple point although it depends on the distance from $R = 0$; that instantaneous chemical reaction occurs only behind Mach stem when Mach number of triple point is larger than CJ one; that the pressure behind the reflected shock is equal to that behind the Mach stem ($P_r = P_m$), and that the flows on the two sides of the slip surface are parallel ($\theta_m = \theta_i - \theta_r$). Using instantaneous flow patterns such as Figs. 4.4 – 4.7, I compare shock angles calculated

by three-shock theory and the position of triple point with those of the simulated data. Figure 4.16 shows the relation between R_{out}/R_{in}, Mach number of triple point and the simulated Mach stem angle ω_m. Mach number of triple point and the simulated Mach stem angle enlarge with increasing R_{out}/R_{in}. As R_{out}/R_{in} increases, they become plateau value around 6.0 and 95 degrees, respectively. Using Mach number and Mach stem angle ω_m at each R_{out}/R_{in} in Fig. 4.16, I calculate incident shock angle ω_i from three-shock theories with and without chemical reaction. Figure 4.17 shows the calculated incident shock angles ω_i in cases of (a) R_{out}/R_{in} = 3, (b) R_{out}/R_{in} = 6, (c) R_{out}/R_{in} = 9, and (d) R_{out}/R_{in} = 17. Red line denotes the shock angle from simulated data. Blue and green lines denote the theoretical incident shock angle ω_i at which a triple point stands. As Mach number and distance from inner radius increases, shock angle decreases and comes close to the solutions of three-shock theories. Triple point appears at intersection point of the simulated shock angle and the solution of three-shock theories. Figure 4.18 shows the relation between R_{out}/R_{in} and incident shock angle ω_i of simulated data, three-shock theories without and with chemical reaction. Since Mach number of triple point is larger than that of CJ, I plot incident shock angle ω_i calculated by three-shock theory with chemical reaction at $R_{out}/R_{in} \geq 6$. First, I focus on the difference of incident shock angles by three-shock theories with and without chemical reaction. See plots of $\times$ and $\triangle$ at R_{out}/R_{in} = 6 and 8 in Fig. 4.18. Since chemical reaction behind shock wave makes pressure decrease, incident shock angle by three-shock theories without chemical reaction is different from and larger than that with chemical reaction. Rankine-Hugoniot relation says that the pressure decrease by

chemical reaction becomes small when Mach number of detonation increases. Therefore, As Mach number of triple point increases, the difference of incident shock angles by three-shock theories with and without chemical reaction becomes close to 0. As $R_{out}/R_{in} \leq 5$ and Mach number of triple point is smaller than CJ one, chemical reaction does not occur at Mach stem near triple point as shown in Fig. 4.5. The simulated incident shock angles agree well with those by three-shock theory without chemical reaction. As $R_{out}/R_{in} \geq 6$ and Mach number of triple point is larger than CJ one, overdriven detonation appears at Mach stem as shown in Figs. 4.6 and 4.7. The simulated incident shock angles agree well with those by three-shock theory with chemical reaction. In Fig. 4.16, when Mach number of triple point becomes larger than CJ one from $R_{out}/R_{in} = 5$ to 6, Mach stem angle suddenly decreases. This is caused by the difference in characteristics of unreactive and reactive Mach stems. My analysis says that pressure decrease by chemical reaction at Mach stem should be considered in order to determine three-shock configurations of Mach reflection structure.

4.4. Propagation behavior of detonations in a two-dimensional large curved channel

Figure 4.19 shows calculation parameters of ratio of outer and inner radius R_{out}/R_{in} and inner radius R_{in}/λ. Although some numerical study [72, 73] showed the propagation behavior of three-dimensional annular tube, R_{out}/R_{in} is not so large (for example, 1.15 in Ref. 72 and 1.29 in Ref. 73) to observe the radial effect such as curved shock front with multi-cellular structure. I use two types of two-dimensional channel at $R_{out}/R_{in} = 1.5$ and

2. R_{in}/λ is varied from 5 to 60 at R_{out}/R_{in} = 1.5 and 5 to 50 at R_{out}/R_{in} = 2. Two detonation modes are observed; one is stable mode (○) and the other is unstable mode (×). As the normalized inner radius R_{in}/λ becomes larger, the detonation shows stable propagation as well as the previous experimental results [79 - 81]. Propagation modes seem to be independent of the ratio of outer and inner radius R_{out}/R_{in} as shown in Fig. 4.19. The propagation characteristics of unstable and stable modes do not depend on inner radius R_{in}/λ. Detailed investigations are carried out using two sets of calculation conditions; R_{in}/λ = 40 at R_{out}/R_{in} = 1.5 and R_{in}/λ = 20 at R_{out}/R_{in} = 2 for unstable mode in Sect. 4.4.1., and R_{in}/λ = 60 at R_{out}/R_{in} = 1.5 and R_{in}/λ = 50 at R_{out}/R_{in} = 2 for stable mode in Sect. 4.4.2. The time evolutions of the simulation results were utilized to reveal the propagation mechanism of unstable and stable modes. In Sect. 4.4.3, stable detonation limit propagating in a curved two-dimensional channel is discussed with quasi-steady solution with curvature effect of shock front.

4.4.1. Unstable mode

The soot tracks on the tube wall were recorded in previous experimental studies [11] and showed remarkable insight for the propagation mechanism of detonations. I show the soot track images using the maximum pressure histories in Figs. 4.20 in cases of (a) R_{in}/λ = 40 at R_{out}/R_{in} = 1.5 and (b) R_{in}/λ = 20 at R_{out}/R_{in} = 2, in order to observe the propagation features of unstable mode in a long period. Notations 1 – 5 shows the characteristic patterns of unstable mode discussed below. In Fig. 4.20, detonation propagates in a counterclockwise direction. Triple points periodically repeat its

generation and disappearance. Figure 4.20 clearly shows specific features of unstable mode such as re-ignition, propagation and decay. Therefore, the propagation mechanism of one cycle of unstable mode can be described using the notations 1 - 5 of Fig. 4.20. (1) Small cells patterns appear, indicating the existence of a multi-headed detonation wave. Detonation maintains its propagation. (2) As detonation propagates in a circumferential direction from (1), the number of triple point decreases, and cell size expands. Soot track images become disturbed patterns. (3) Triple point disappears near the inner wall. This spreads or reaches to outer wall. In the case of propagation in a curved channel, diffraction effect always appears near the inner wall. In periods between (1) and (3), transverse waves, which have important roles to complete the potential exothermicity, become weak, and chemical reaction stops near the inner wall. Since its effect spreads, triple point disappears from inner wall to outer wall. (4) After that, large black belt indicating transverse detonation is generated near the outer wall and propagates to inner wall as shown in Fig. 4.20. Transverse detonation consumes the potential exothermicity of unburned gas pocket near inner wall. (5) After the propagation of the transverse detonation to inner wall, new small cells are generated, and multi-headed cellular detonation re-appears. In this phase, re-ignition is completed. The above-described mechanism is repeated during the long range of numerical simulation in the unstable mode. In the case of R_{out}/R_{in} = 2, since the diffraction effect from inner wall is stronger than that of R_{out}/R_{in} = 1.5, soot track image in Fig. 4.20b seems to be more complex, and detonation propagates much more unstably.

Unstable mode shows repetitions of re-ignition and decay of detonation in a curved

channel as shown in Fig. 4.20. Therefore, its propagation behavior is described using a series of figures, which denote one cycle of re-ignition and decay. In order to reveal the wave structure of unstable mode, and velocity histories and instantaneous distributions of physical values are examined. Figures 4.21 and 4.22 show detonation velocity histories in a circumferential direction at the center of channel $R = (R_{out}+R_{in})/2$ in cases of $R_{in}/\lambda = 40$ at $R_{out}/R_{in} = 1.5$ and $R_{in}/\lambda = 20$ at $R_{out}/R_{in} = 2$, respectively. Blue lines denote a CJ velocity of planar detonation $D_{CJ,planar}$ in Figs. 4.21 and 4.22. Detonation velocities in the unstable mode repeat underdriven and overdriven ones. Figs. 4.21b and 4.22b are close up view of Fig. 4.21a and 4.22a, where sudden changes of detonation velocities are observed. Figures 4.23 and 4.24 show instantaneous distributions A – H of (a) density ρ, (b) pressure P and (c) mass fraction of reactant β in cases of $R_{in}/\lambda = 40$ at $R_{out}/R_{in} = 1.5$ and $R_{in}/\lambda = 20$ at $R_{out}/R_{in} = 2$, respectively. White lines in Figs. 4.23c and 4.24c denote shock fronts. Figures 4.23A – 4.23H and 4.24A – 4.24H are a sequence of decay and re-ignition, and notations A – H in Figs. 4.23 and 4.24 correspond to those in Figs. 4.21b and 4.22b. Flow patterns in Figs. 4.23 and 4.24 are observed in arrows in Fig. 4.20a and 4.20b, respectively. Although detonations are rotating in counterclockwise direction, the position of shock front is fixed in Figs. 4.23 and 4.24. I use notations A – H in Figs. 4.21 – 4.24 in explanation of flow features in unstable mode. As detonation propagates in a two-dimensional curved channel, curved detonation front and intricate reflections of wave at outer walls behind detonation front are observed. Behind reflected shock wave on the outer wall, pressure shows higher value as shown in Figs. 4.23 and 4.24. Reflection and accumulation effect on the outer

wall is key point to discuss the detonation propagation in unstable mode. When detonation maintains its propagation at (A), (B), (G) and (H) in Figs. 4.23 and 4.24, multi-cellular curved detonation front appears, and its velocity at the center of channel becomes overdriven as shown in Figs. 4.21 and 4.22. As detonation propagates from moments (A) to (B), the number of triple point decreases, which denotes gradual decay of detonation. Detonation front becomes distorted shape. At moment (C), since detonation always diffracts near inner wall and tend to become weak, shock wave separates from reaction front, and unburned gas pocket is generated near inner wall. The detonation velocity in a circumferential direction decreases to underdriven one as shown in Figs. 4.21b and 4.22b. Moment (D) is just before the generation of transverse detonation near the outer wall. Transverse wave will develop to transverse detonation in the case of R_{out}/R_{in} = 1.5 in Fig. 4.23. Reflected shock wave on the outer wall makes higher pressure behind it, which easily induces the chemical reaction. Reflected shock wave will evolve to transverse detonation at outer wall in the case of R_{out}/R_{in} = 2 as shown in Fig. 4.24. In this phase, a large amount of unburned gas is observed. In Fig. 4.24D-c, two sets of unburned gas pocket are generated. Since diffraction effect in the case of R_{out}/R_{in} = 2 is stronger than that of R_{out}/R_{in} = 1.5, unstable and complex flow patterns tend to be observed in the present simulations. At moment (E), in the case of R_{out}/R_{in} = 1.5, transverse detonation is propagating to inner wall and consuming unburned gas behind shock wave. In the case of R_{out}/R_{in} = 2, transverse detonation, which is transformed from reflected shock wave on the outer wall, is propagating to inner wall. Reactive Mach stem, which is extended from triple point behind detonation

front as shown in Fig. 4.24A, is also propagating to detonation front and consumes the unburned gas near inner wall. Detonation is reignited by transverse detonation propagating to inner wall and reactive Mach stem propagating to detonation front. Therefore, re-ignition process is more complicated than that in the case of R_{out}/R_{in} = 1.5. At moment (F), transverse detonation and reactive Mach stem consume all unburned gas pocket, and new triple points are generated. Detonation velocities finish their recovering as shown in Figs. 4.21b and 4.22b, and re-ignition phase is completed. At moment (G) and (H), multi-cellular curved detonation maintains its propagation with decreasing the number of triple point. A series of processes is repeated in the long history of unstable mode.

When detonation propagates from narrow tubes or two-dimensional channel to open area [84 - 87], diffraction of wave makes detonation weak, and shock front separates from reaction front. In order to occur re-ignition of detonation at expansion area, previous study says that geometric lengths such as a diameter of circular tube and a width of two-dimensional channel should be larger than the critical value. Once detonation re-ignites at some point, spherical or cylindrical detonations will continue its propagation. In the case of unstable mode in a curved two-dimensional channel, diffraction effect from inner wall is comparatively strong and always affects detonation propagation. Detonation tends to fail. However, in a curved channel, accumulation effect at outer wall makes transverse detonation propagating to inner wall and reflected shock wave. Therefore, re-ignition is easily observed near outer wall. Detonation in unstable mode periodically shows decay due to diffraction effect from inner wall and

re-ignition due to accumulation effect and reflection from outer wall. Therefore, the detonation in unstable mode in a curved channel may be named as “outer wall supported detonation”.

4.4.2. Stable mode

Detonation maintains its propagation with almost constant velocity in a circumferential direction, and the same shape of detonation front structure and multi-headed cellular structures in stable mode. I show its propagation behavior using a series of figures. Figure 4.25 shows soot track images of (a) $R_{in}/\lambda = 60$ at $R_{out}/R_{in} = 1.5$ and (b) $R_{in}/\lambda = 50$ at $R_{out}/R_{in} = 2$, respectively, in order to observe the propagation features of stable mode in a long period. Triple points disappear near the inner wall, and transverse detonations described as black large belts reflect on the inner wall as well as unstable mode. However, unlike unstable mode as shown in Fig. 4.20, disappearance of triple point does not spread far away from inner wall, and multi-headed detonation maintains its stable propagation in a curved channel. Figure 4.25 clearly shows specific features of stable mode such that detonation always maintains its propagation with multi-headed cellular structure.

In order to reveal the wave structure of stable mode, velocity histories and instantaneous distributions of physical values are examined. Figures 4.26 and 4.27 show detonation velocity histories in a circumferential direction at the center of channel $R = (R_{out}+R_{in})/2$ in cases of $R_{in}/\lambda = 60$ at $R_{out}/R_{in} = 1.5$ and $R_{in}/\lambda = 50$ at $R_{out}/R_{in} = 2$, respectively. Blue lines denote a CJ velocity of planar detonation $D_{CJ,planer}$ in Figs. 4.26 and 4.27.

Detonation velocities in the stable mode show almost constant value around $1.1D_{CJ,planar}$ in Fig. 4.26 and $1.3D_{CJ,planar}$ in Fig. 4.27. They sometimes decrease due to disappearance of triple point near inner wall as shown in Fig. 4.25 but are always more than CJ value. Figs 4.26b and 4.27b are close up view of Fig. 4.26a and 4.27a near detonation velocity changes. Figures 4.28 and 4.29 show eight distributions A – H of (a) density ρ, (b) pressure P and (c) mass fraction of reactant β in cases of $R_{in}/\lambda = 60$ at $R_{out}/R_{in} = 1.5$ and $R_{in}/\lambda = 50$ at $R_{out}/R_{in} = 2$, respectively. White lines in Figs. 4.28c and 4.29c denote shock fronts. Figures 4.28A – 4.28H and 4.29A – 4.29H are a sequence of detonation velocity change, and notations A – H in Figs. 4.26b and 4.27b correspond to those in Figs. 4.28 and 4.29. Flow patterns in Figs. 4.28 and 4.29 are observed in arrows in Fig. 4.25a and 4.25b, respectively. Although detonations are rotating in counterclockwise direction, the position of shock front is fixed in Figs. 4.28 and 4.29. I use notations A – H in Figs. 4.26 – 4.29 in explanation of flow features in stable mode. As well as unstable mode, curved detonation front and intricate reflections of wave at outer walls behind detonation front are observed. In stable mode, similar shock structure with multi-cellular curved front and Mach reflection appear as shown in Figs. 4.28 and 4.29. Transverse wave consumes premixed gas behind detonation front at (A) – (C), a curved detonation maintain its propagation. When the detonation velocity decreases at moment (D) in Fig. 4.26b and 4.27b, diffraction effect makes transverse wave weak, and chemical reaction stops near inner wall. Unburned gas exists near the inner wall. Unlike unstable mode, it does not spread far away from inner wall, and curved detonation at outer side of channel propagates with multi-cellular structure. After the

propagation of transverse detonation to inner wall at (E), detonation velocities finish their recovering. Multi-cellular curved detonation propagates with similar shock fronts at (F) – (G) as well as (A) – (C). As detonation propagates in a curved channel, diffraction effect is also observed in stable mode as well as unstable mode, but seems to be relatively small for detonation propagation. I discuss the diffraction effect and the reason that detonation is stabilized with increase of inner radius R_{in}/λ, qualitatively. Here, I neglect accumulation effect from outer wall and propagation of transverse waves because of simplification in discussion below. Arrival time, at which expansion wave propagates with the characteristic speed from inner wall to outer wall, linearly becomes longer with increase of channel width. However, shock dynamics says that diffraction effect does not depend on channel width L at constant R_{out}/R_{in} of a curved channel, and that the arrival time of expansion wave to outer wall is constant when time τ is properly normalized, for example, by $\tau = t/t^* = t/(2\pi R_{in}/D_{CJ,planar})$. Normalized time $\tau = 0$ denotes the time that planar detonation enters into a curved channel from a straight one. As detonation propagates in a two-dimensional curved channel, diffraction effect causes the decrease of temperature T and density ρ. The region, at which detonation front experiences expansion wave, and at which chemical reaction stops, spreads from the inner wall to outer wall. I qualitatively estimate the re-ignition time τ_{ig} at inner wall after shock front separates from reaction front from $\tau = 0$. Equation (4.1) shows the induction reaction rate described by normalized time.

$$\omega_{\alpha}^{*} \equiv \frac{d\alpha}{d\tau} = \frac{d\alpha}{dt}\frac{dt}{d\tau} = -\frac{1}{\tau_{ig}} = -k_1 \rho \exp\left(-\frac{E_1}{RT}\right) \times \frac{2\pi R_{in}}{V_{CJ}} \tag{4.1}$$

Equation (4.1) says that, with increase of inner radius R_{in}/λ, normalized ignition time τ_{ig} shortens. Therefore, at larger inner radius R_{in}/λ, before expansion wave propagates far away from inner wall, re-ignition may occur at inner wall, and that diffraction effect is limited only near the wall. Detonation in a curved channel is further stabilized from the viewpoint of re-ignition after experience of diffraction.

In order to discuss the effect of R_{out}/R_{in}, shock front structure is discussed using Fig. 4.3 as Nakayama *et al.* [80, 81] conducted. Figure 4.30 shows distributions of (a) shock angle ω, (b) angle difference θ_{in} - θ, and (c) the normal detonation velocity $D_n/D_{CJ,planar}$ on normalized radius R/R_{in}. Detonation velocity is normalized with respect to planar CJ one $D_{CJ,planar}$ of one-dimensional steady solution. As the normalized radius R/R_{in} increases, shock angle ω and angle difference $\theta_{in} - \theta$ changes. The normal detonation velocity approaches to CJ value. In the previous study of oblique detonation, shock angle, in which gas flows into detonation front, depends on Mach number of premixed gas in order to satisfy that the normal premixed gas velocity into detonation front D_n becomes close to CJ one $D_{CJ,planar}$. In the case of detonation in a curved channel, premixed gas velocity linearly enlarges with increase of the normalized radius R/R_{in}, and shock angle ω decreases in order to satisfy CJ velocity condition. In our simulated data, detonation velocity at inner radius does not depend on R_{out}/R_{in} (1693 m/s for R_{out}/R_{in} = 1.5, 1699 m/s for R_{out}/R_{in} = 2). Therefore, Distributions described in Fig. 4.30

do not depend on R_{out}/R_{in} as well as the previous analysis by Nakayama *et al*. Detonation in a curved channel has self-similar shock front structure.

4.4.3. Theoretical investigation of stable detonation limit in a two-dimensional curved channel

Detonation in a two-dimensional curved channel shows almost steady propagation with constant detonation velocity and the same detonation front shape in stable mode. I assume detonation in the stable mode steadily propagates with constant shock radius distribution and discuss the stable detonation limit in a two-dimensional curved channel using the steady solution with shock front curvature [88 – 91]. Schematic picture of steady curved detonation with shock radius R_s is described in Fig. 4.31. In one dimension, the quasi-steady governing equations in the shock-attached frame are

$$\frac{\mathrm{d}\left(\rho u_n\right)}{\mathrm{d}n} + \kappa\rho\left(D_n + u_n\right) = 0, \tag{4.2}$$

$$u_n \frac{\mathrm{d}\left(u_n\right)}{\mathrm{d}n} + \frac{1}{\rho}\frac{\mathrm{d}p}{\mathrm{d}n} = 0, \tag{4.3}$$

$$\frac{\mathrm{d}}{\mathrm{d}n}\left(\frac{e}{\rho}\right) - \frac{p}{\rho^2}\frac{\mathrm{d}\rho}{\mathrm{d}n} = 0, \tag{4.4}$$

$$u_n \frac{\mathrm{d}\alpha}{\mathrm{d}n} + \omega_\alpha = 0, \tag{4.5}$$

and

$$u_n \frac{\mathrm{d}\beta}{\mathrm{d}n} + \omega_\beta = 0. \tag{4.6}$$

Here, ω_α and ω_β denote reaction rate of induction and exothermic periods as shown in Eqs. (2.8) and (2.9). D_n and u_n are detonation and gas velocity in shock-attached frame. e indicates total energy per unit volume. κ shows curvature of detonation front and is calculated by shock front radius R_s as $1/R_s$ in a two-dimensional curved channel. Initial condition is post shock values such as density and pressure calculated by Rankine-Hugoniot condition, and I calculate CJ detonation velocity with shock radius R_s by numerically solving Eqs. (4.2) – (4.6) and the generalized CJ criterion [88]. Figure 4.32 shows the relation between shock radius R_s/λ and the detonation velocity normalized with respect to planar CJ detonation velocity. The normalized detonation velocity depends on shock radius R_s/λ. As shock radius is smaller than $R_s/\lambda = 27.2$, the solution of quasi-steady detonation disappears. This indicates that CJ detonation with shock front whose radius is smaller than $R_s/\lambda = 27.2$ cannot maintain its propagation. The shock radius is important factor to discuss the propagation of detonation in a curved channel. Therefore, $R_s/\lambda = 27.2$ is defined as critical shock radius. I applied the idea of quasi-steady solution to the numerical results of detonation propagating in a two-dimensional curved channel. Figure 4.33 shows the relation of the normalized radius R/R_{in} and shock radius R_s/λ in the case of stable mode at $R_{in}/\lambda = 60$ at $R_{out}/R_{in} =$

1.5 and $R_{in}/\lambda = 50$ at $R_{out}/R_{in} = 2$. Shock radius shows monotonically increasing with the normalized radius R/R_{in} and does not depend on R_{out}/R_{in} as well as data in Fig. 4.30.

As discussed in 4.4.1. and 4.4.2., diffraction effect from inner wall makes detonation weak, and shock front separates from reaction front, which spreads from inner wall. Therefore, I focus on the shock radius at inner wall in order to determine that detonation can maintain its propagation or not. Figure 4.34 shows the relation between propagation modes (○; stable mode and ×; unstable mode), inner radius R_{in}/λ and shock radius R_s/λ at inner wall. Blue line indicates $R_s/\lambda = 27.2$ calculated by quasi-steady solution. Red and Black symbols show the numerical results in cases of R_{out}/R_{in} = 1.5 and 2, respectively. In unstable mode, I calculate shock radius R_s/λ when detonation transiently maintains its propagation. I confirm that shock front structure does not depend on the normalized radius R/R_{in} in unstable mode as well as in stable mode. Therefore, shock radius R_s/λ shows linear increase with inner radius R_{in}/λ. The criterion that detonation in a curved detonation propagates as stable mode or unstable mode is well described by $R_s/\lambda = 27.2$. This says that the idea of quasi-steady solution is available to a steadily propagating curved detonation. In unstable mode, since steady solution of curved CJ detonation does not exist, the detonation cannot maintain its propagation, and cyclic behavior of re-ignition, propagation and decay is observed.

4.5. Summary

Detonations with curved shock front propagating in a curved channel were numerically investigated using two-dimensional Euler equations and two-step reaction model by

Korobeinikov *et al.* In order to reveal the self-sustaining propagation mechanism of detonations in a curved channel, two series of calculations were conducted.

The effect of the ratio of outer and inner radii R_{out}/R_{in} of detonation propagation in a small curved channel is investigated. In a small two-dimensional curved channel whose width is equivalent to 0.5λ (λ: simulated cell width), steady detonations with curved shock front are obtained. In the case of R_{out}/R_{in} = 2, shock front generally stands perpendicular to walls. Chemical reaction intermittently occurs in the zig-zag chemical reaction zone, and generated compression wave affects the shock front. This induces periodical change of shock front shape and makes cellular-like pattern. In cases of $R_{out}/R_{in} \geq 3$, a steady shock front shows Mach reflection with curved incident shock and Mach stem. As R_{out}/R_{in} increases, Mach number of incoming flow in a circumferential direction of shock-attached coordinate at inner wall gradually decreases and is smaller than 1.0 in cases of $R_{out}/R_{in} \geq 6$. In cases of $R_{out}/R_{in} \leq 6$ and $R_{out}/R_{in} \geq 7$, incident waves becomes shock wave and continuous compression waves, respectively. Shock front characteristics are discussed in detail using Whitham theory and three-shock theories with and without chemical reaction. In cases of $R_{out}/R_{in} \leq 7$, distribution of shock angle between inner wall and triple point does not agree with that by Whitham theory. However, the knowledge from shock dynamics without chemical reaction, that distribution of shock angle is independent of R/R_{in}, is also adapted to those with chemical reaction only when Mach number at inner wall is larger than 1.0. In cases of $R_{out}/R_{in} \geq 8$, shock angle does not depend on $(R-R_{in})/(R_{out}-R_{in})$, and the shock characteristics differ from those in cases of $R_{out}/R_{in} \leq 7$. As Mach number at inner wall

is smaller than 1.0, continuous compression waves from weakest (Mach wave) to some strong waves are observed. Therefore, Mach wave is important propagation mechanism to decide shock front angle. I investigate structure of three-shock configuration using three-shock theories with and without chemical reaction. Depending on Mach number of triple point, the simulated incident shock angles agree well with those by three-shock theory with (at larger than CJ Mach number) and without (at smaller than CJ Mach number) chemical reaction.

In a large two-dimensional curved channel, propagation behavior and stable detonation limit are investigated. I simulate detonations with various channel widths in two types of two-dimensional curved channels, where the ratios of inner and outer radii R_{out}/R_{in} are 1.5 and 2. Two propagation modes, namely unstable and stable modes, are observed depending on the normalized inner radius R_{in}/λ. In unstable mode, diffraction and accumulation effects from inner and outer wall complexly appear in detonation propagation. A curved detonation propagates with repetition of decay, re-ignition and propagation. Its velocity varies from underdriven to overdriven in one cycle. In stable mode, the detonation propagates steadily with keeping a curved shock front structure with multi-cellular pattern and a constant detonation velocity in circumferential direction. Shock front structures do not depend on R_{out}/R_{in} as well as the previous experimental studies. Since quasi-steady solution exists when the shock radius of CJ detonation front is larger than the critical value, I apply the idea of quasi-steady solution to the numerical results of detonation propagating in a two-dimensional curved channel. I confirm that the detonation propagates steadily in the case of larger shock radius of

detonation front than the critical value. This says that the idea of quasi-steady solution is available to a steadily propagating curved detonation and gives the stable detonation limit in a curved channel.

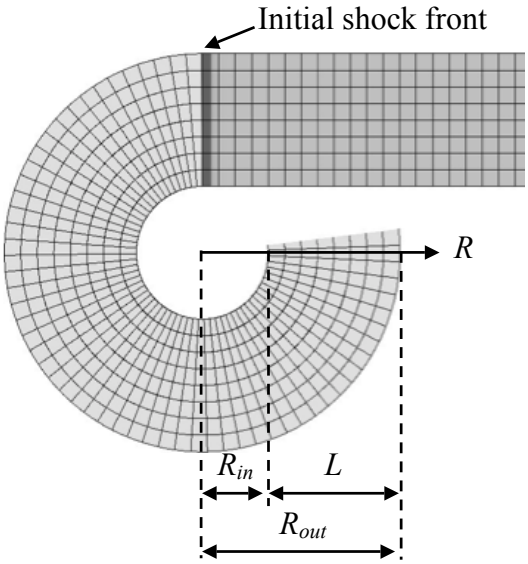

Fig. 4.1 An example of the computational grids and initial conditions in the case of the ratio of outer and inner radii R_{out}/R_{in} = 3. In Sect. 4.3., channel width L is equivalent to $\lambda/2$ (λ: the simulated cell width in Chapter 2), and the ratio of outer and inner radii R_{out}/R_{in} is chosen as a parameter. In Sect. 4.4., the ratio of outer and inner radii R_{out}/R_{in} is 1.5 and 2, and the normalized inner radius R_{in}/λ is chosen as a parameter.

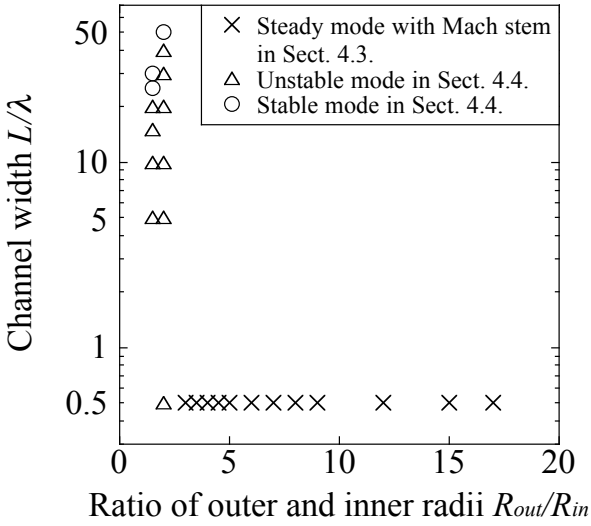

Fig. 4.2 Calculation parameters of Ratio of outer and inner radii R_{out}/R_{in} and channel width L/λ.

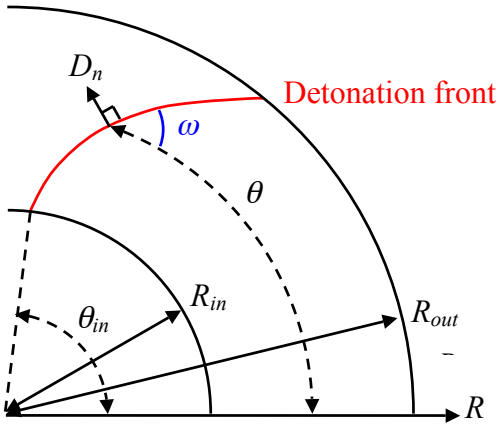

Fig. 4.3 Definitions of shock angle ω, the angle from the reference line θ and the normal detonation velocity D_n.

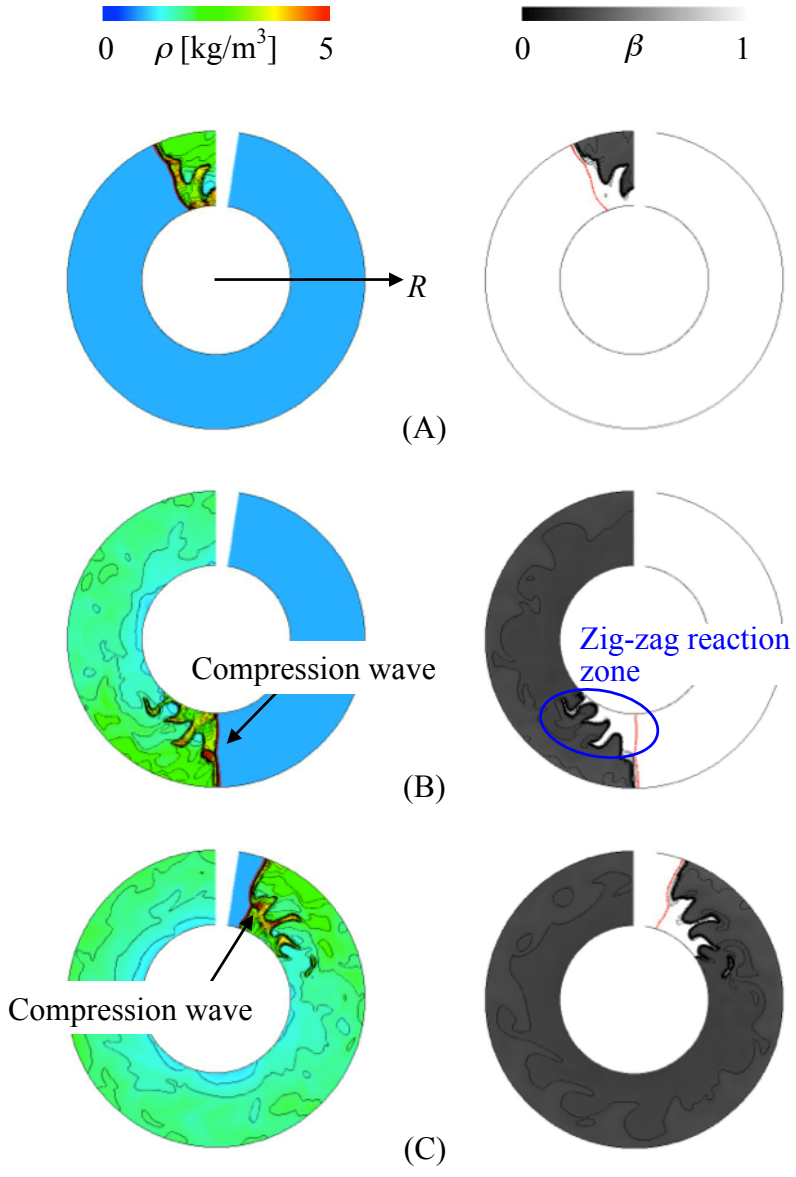

Fig. 4.4 Time-evolving three snapshots A – C of (a) density ρ and (b) mass fraction of reactant β in the case of $R_{out}/R_{in} = 2$.

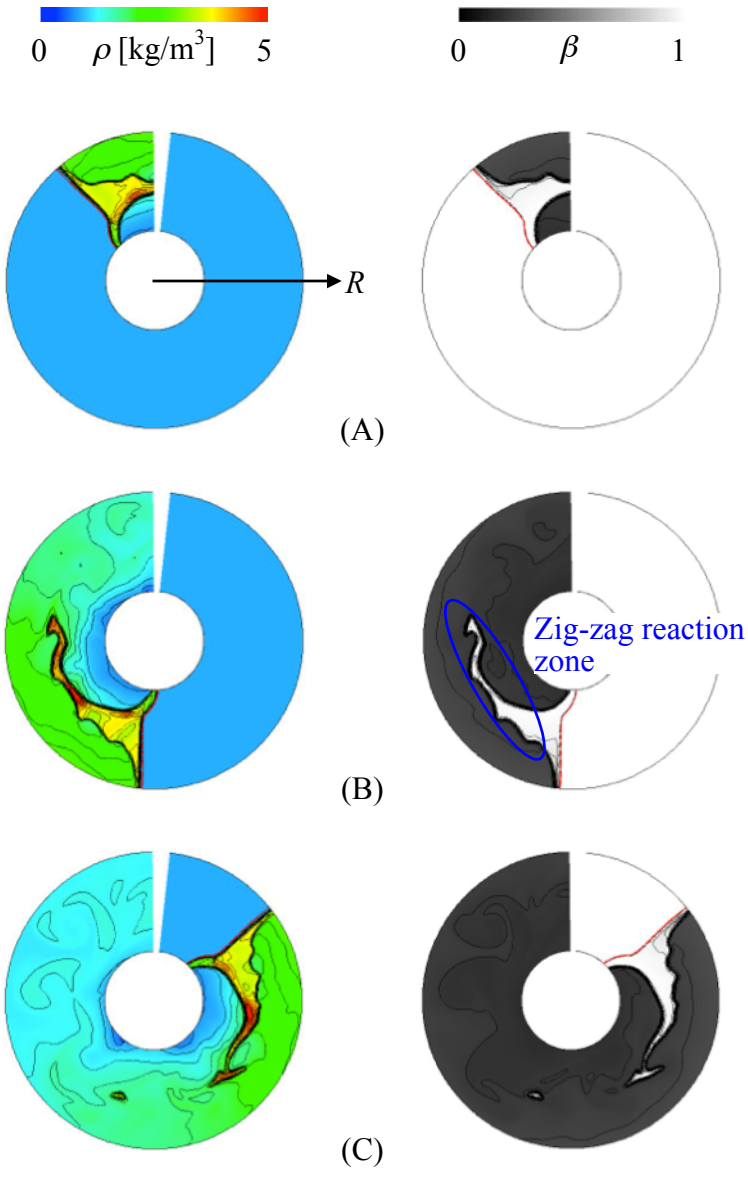

(a) density (b) mass fraction of reactant

Fig. 4.5 Time-evolving three snapshots A – C of (a) density ρ and (b) mass fraction of reactant β in the case of $R_{out}/R_{in} = 3$.

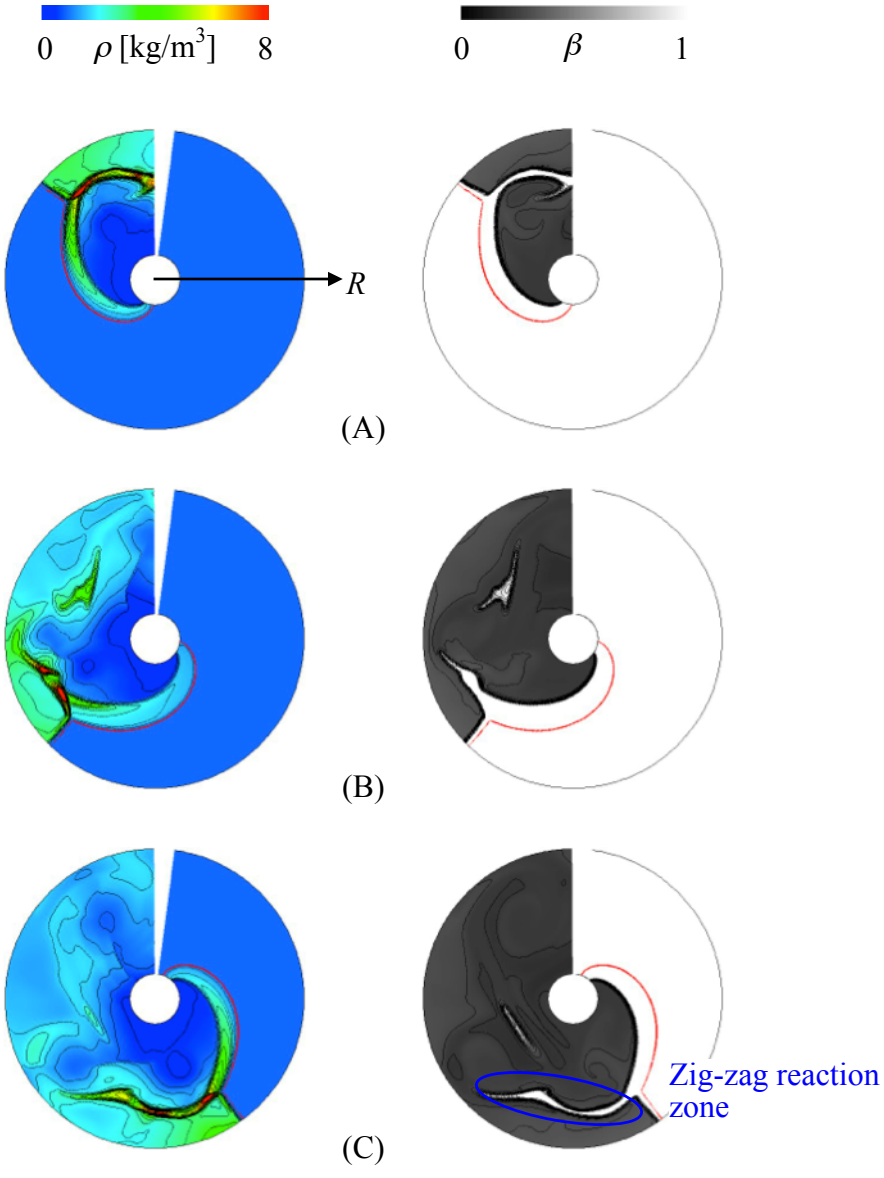

(a) density (b) mass fraction of reactant

Fig. 4.6 Time-evolving three snapshots A – C of (a) density ρ and (b) mass fraction of reactant β in the case of $R_{out}/R_{in} = 6$.

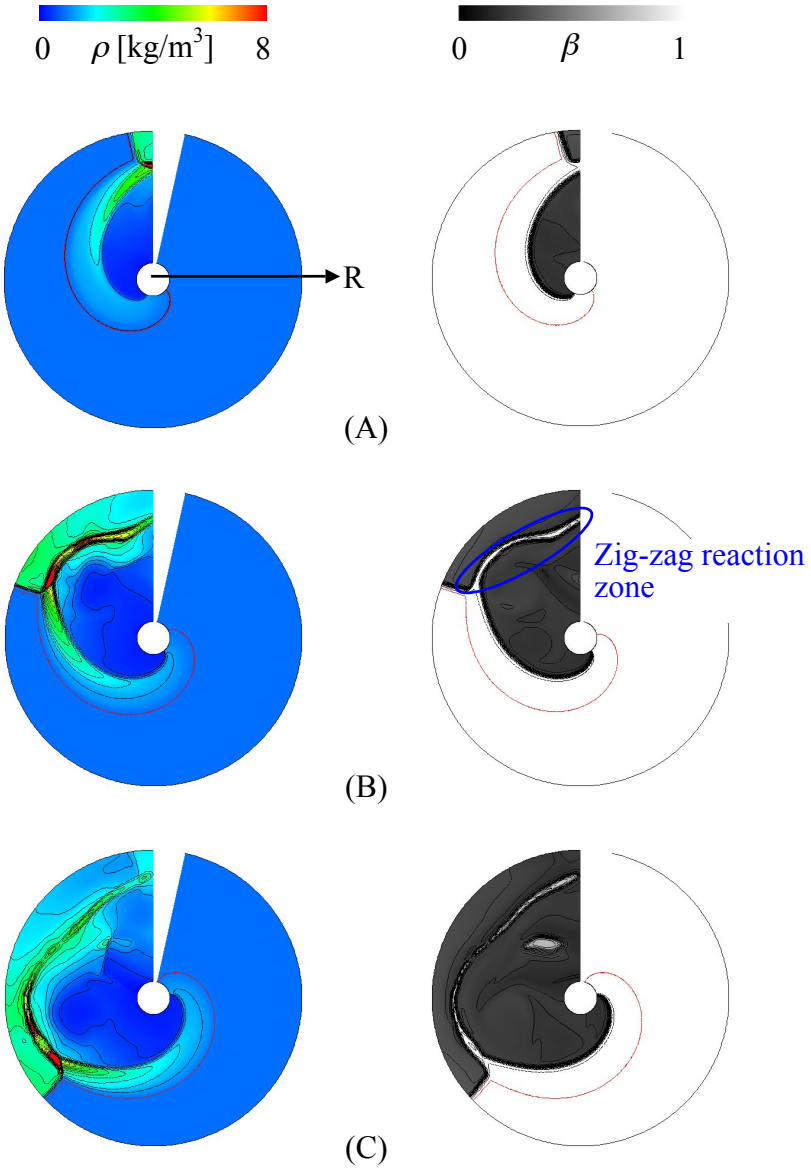

(a) density (b) mass fraction of reactant

Fig. 4.7 Time-evolving three snapshots A – C of (a) density ρ and (b) mass fraction of reactant β in the case of $R_{out}/R_{in} = 9$.

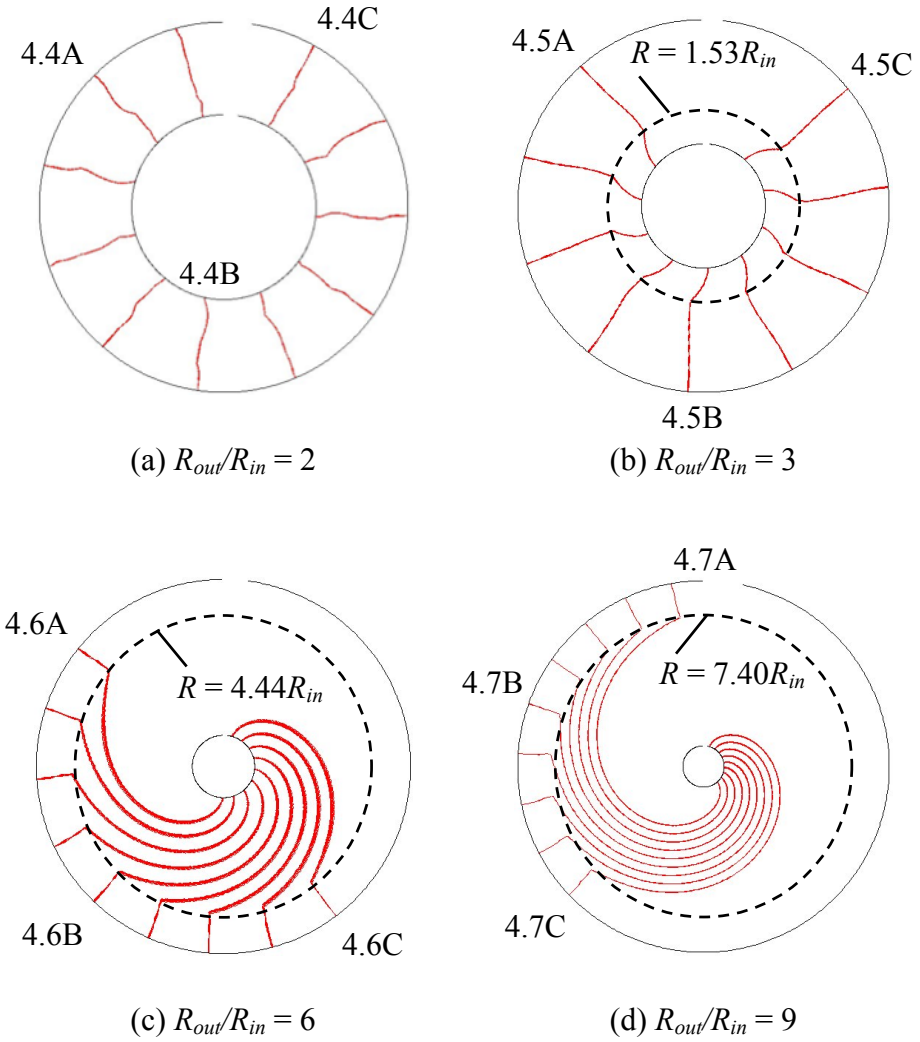

(a) $R_{out}/R_{in} = 2$ (b) $R_{out}/R_{in} = 3$

(c) $R_{out}/R_{in} = 6$ (d) $R_{out}/R_{in} = 9$

Fig. 4.8 Superimposed pictures of instantaneous shock fronts at (a) R_{out}/R_{in} = 2, (b) R_{out}/R_{in} = 3, (c) R_{out}/R_{in} = 6 and (d) R_{out}/R_{in} = 9. Shock fronts described as 4.4A – 4.4C, 4.5A – 4.5C, 4.6A – 4.6C and 4.7A – 4.7C in Fig. 4.8 correspond to those at A – C in Figs. 4.4, 4.5, 4.6 and 4.7, respectively.

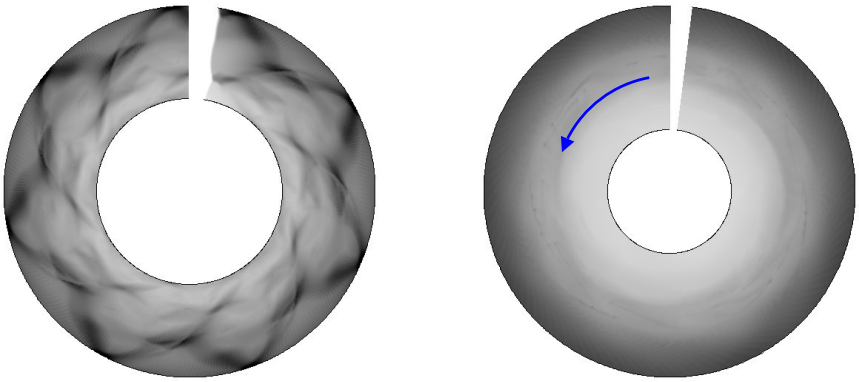

(a) $R_{out}/R_{in} = 2$ (b) $R_{out}/R_{in} = 3$

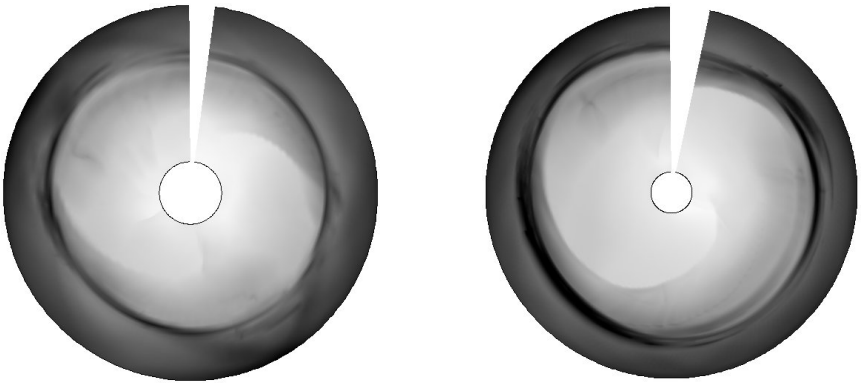

(c) $R_{out}/R_{in} = 6$ (d) $R_{out}/R_{in} = 9$

Fig. 4.9 Soot track images using the maximum pressure histories and traces of triple points are described in cases of (a) $R_{out}/R_{in} = 2$, (b) $R_{out}/R_{in} = 3$, (c) $R_{out}/R_{in} = 6$ and (d) $R_{out}/R_{in} = 9$.

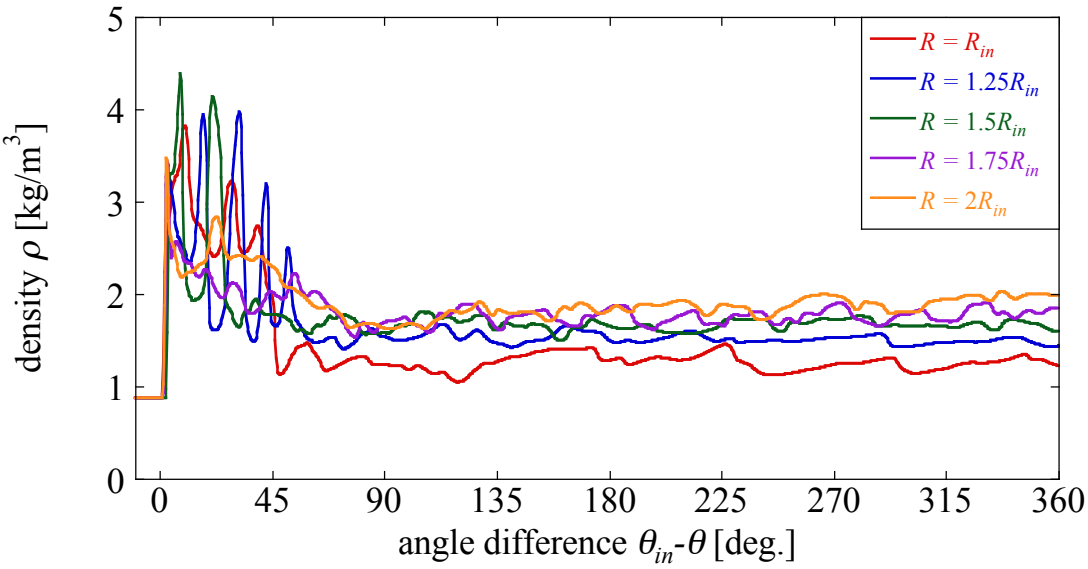

(a)

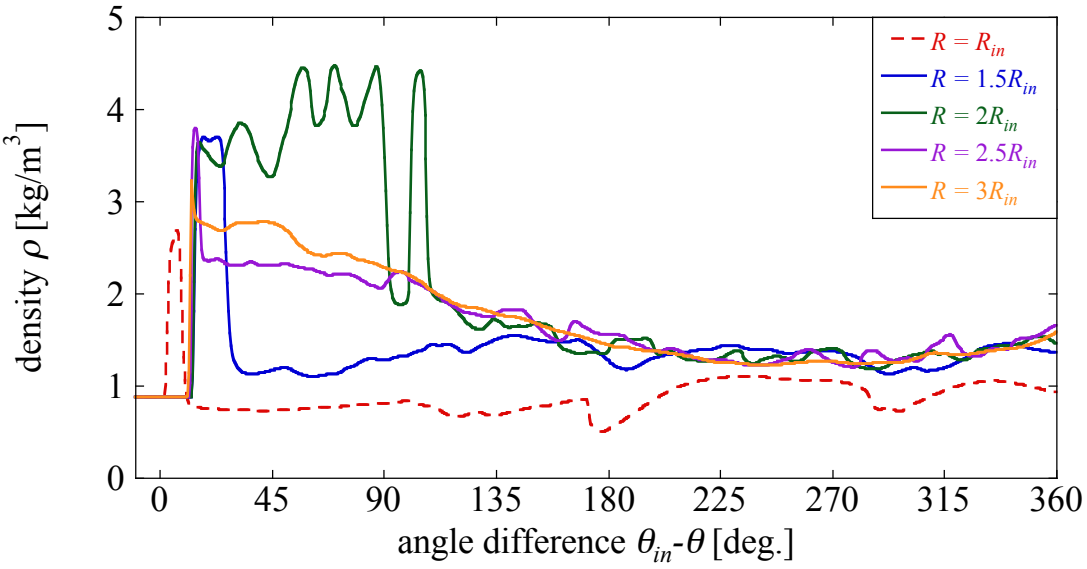

(b)

Fig. 4.10 Instantaneous density distributions of (a) R_{out}/R_{in} = 2, (b) R_{out}/R_{in} = 3. (c) R_{out}/R_{in} = 6 and (d) R_{out}/R_{in} = 9 at various radii R in the moment of Figs. 4.4C, 4.5C, 4.6C and 4.7C. Solid and dashed lines indicate that radius R is located at Mach stem and incident wave, respectively.

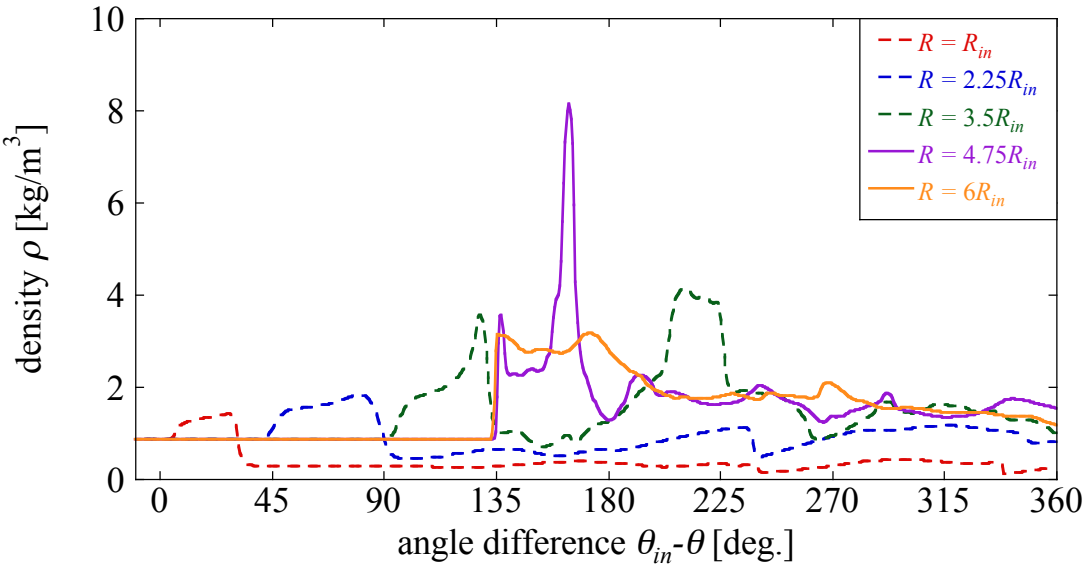

(c)

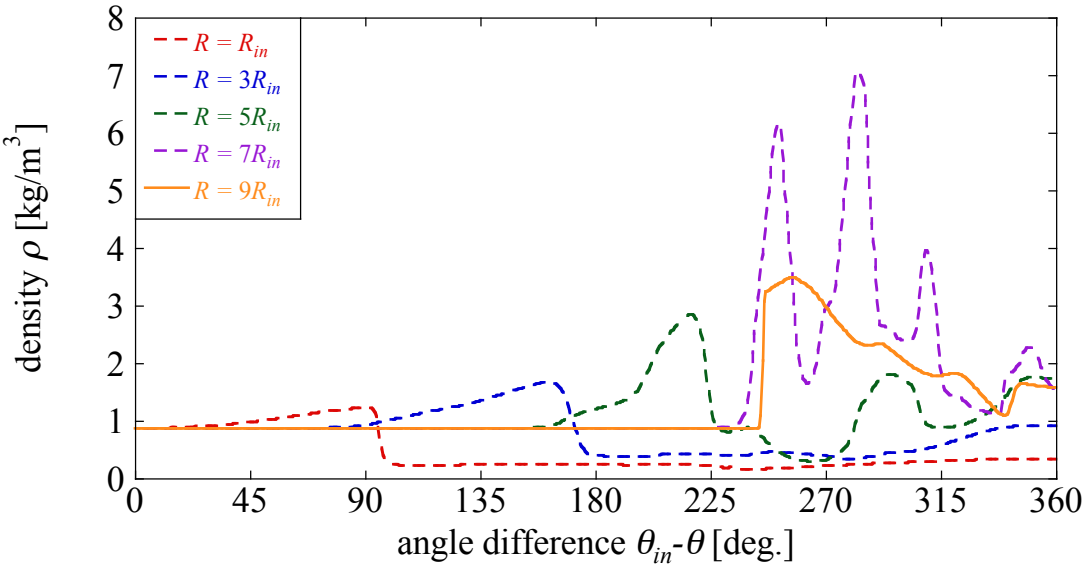

(d)

Fig. 4.10(cont.) Instantaneous density distributions of (a) R_{out}/R_{in} = 2, (b) R_{out}/R_{in} = 3, (c) R_{out}/R_{in} = 6 and (d) R_{out}/R_{in} = 9 at various radii R in the moment of Figs. 4.4C, 4.5C, 4.6C and 4.7C. Solid and dashed lines indicate that radius R is located at Mach stem and incident wave, respectively.

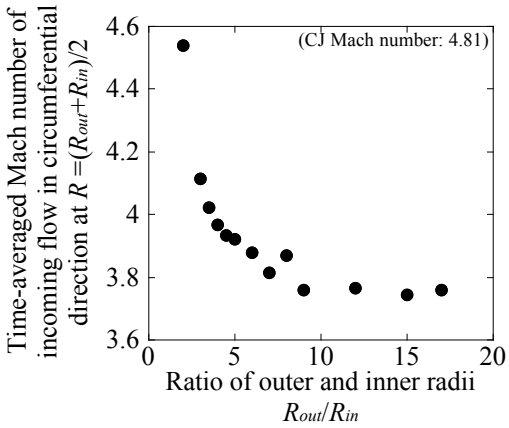

(a)

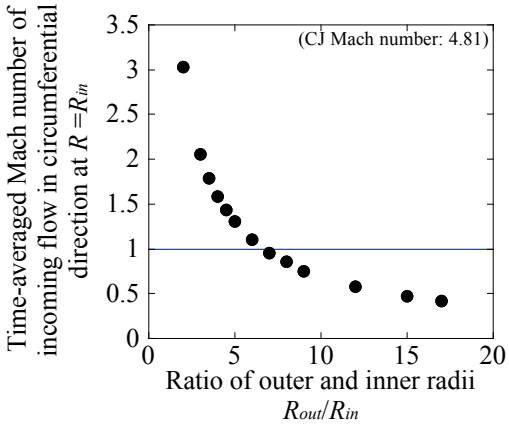

(b)

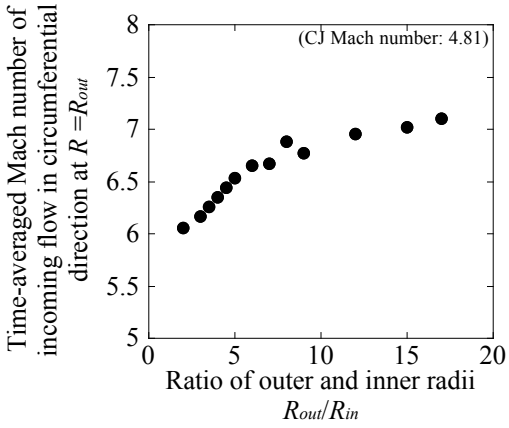

(c)

Fig. 4.11 Time-averaged Mach number of incoming flow in a circumferential direction at (a) center of channel $R = (R_{out}+R_{in})/2$, (b) inner wall $R = R_{in}$ and (c) outer wall $R = R_{out}$ in shock-attached coordinate.

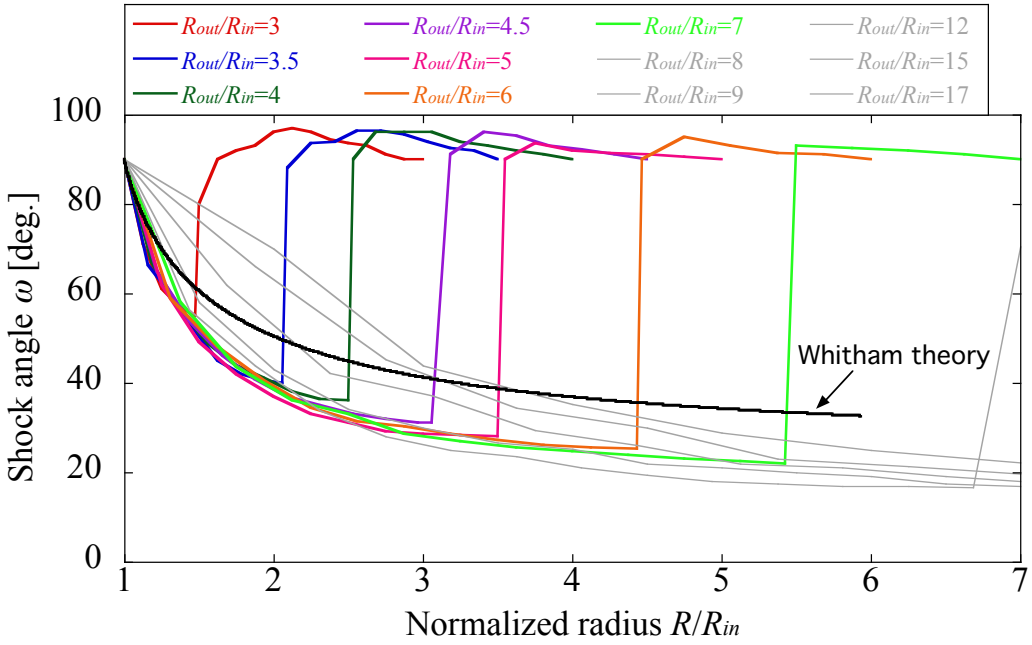

(a) focusing on $3 \leq R_{out}/R_{in} \leq 7$

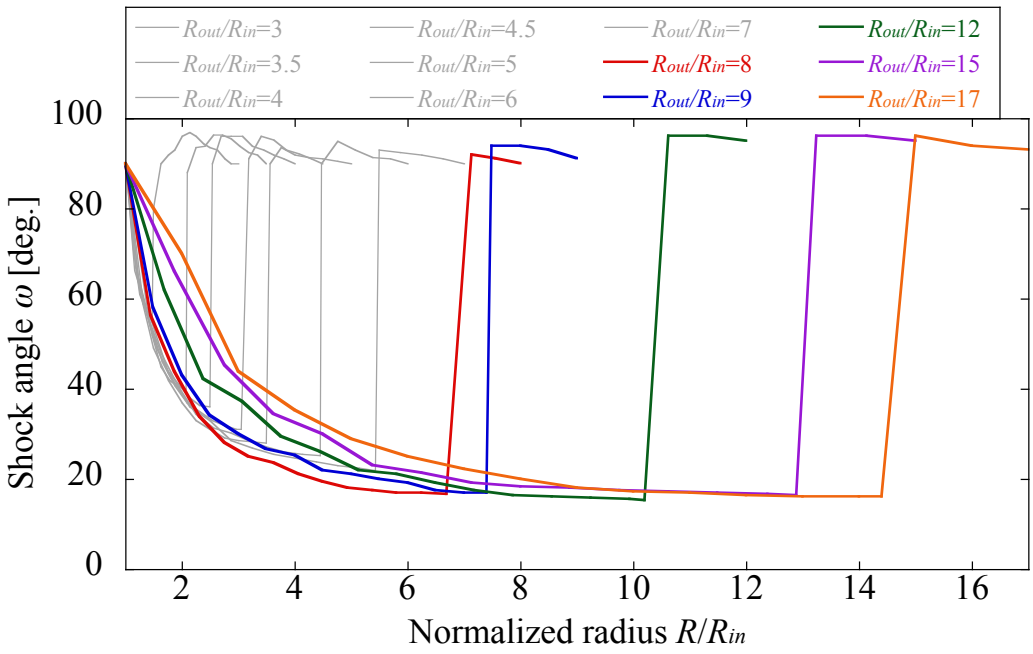

(b) focusing on $8 \leq R_{out}/R_{in} \leq 17$

Fig. 4.12 Distributions of shock angles ω between inner and outer walls focusing on (a) $3 \leq R_{out}/R_{in} \leq 7$ and (b) $8 \leq R_{out}/R_{in} \leq 17$ as described by color lines. Horizontal axis represents R/R_{in}.

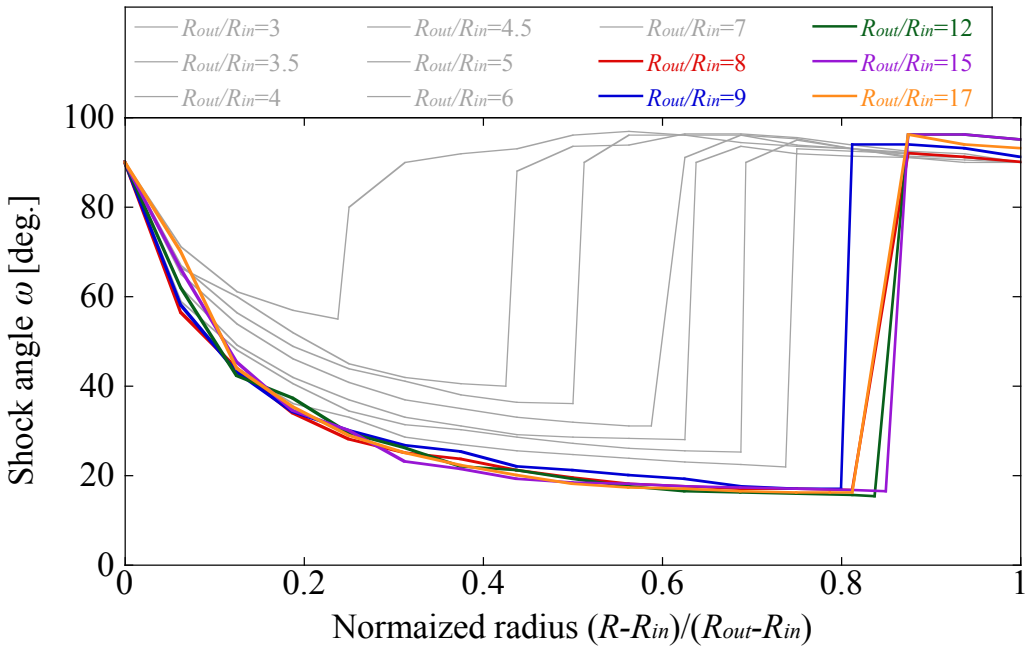

Fig. 4.13 Distributions of shock angle ω between inner and outer walls focusing on $R_{out}/R_{in} \geq 8$. Horizontal axis represents $(R\text{-}R_{in})/(R_{out}\text{-}R_{in})$.

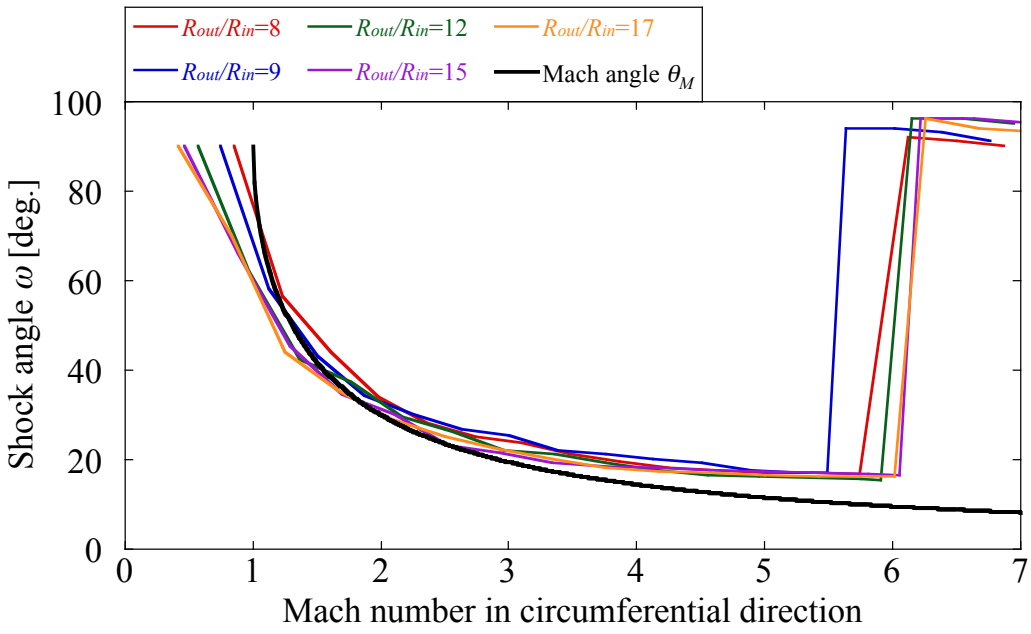

Fig. 4.14 Relation between shock angles ω, Mach number of incoming flow in a circumferential direction of shock attached coordinate and Mach angle θ_M.

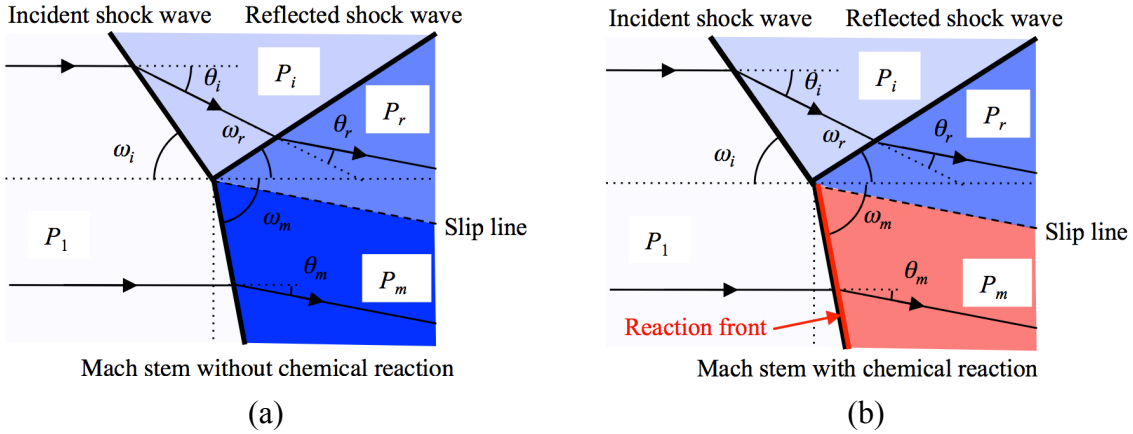

Fig. 4.15 Schematic pictures of three shock intersections at a triple point (a) without and (b) with chemical reaction.

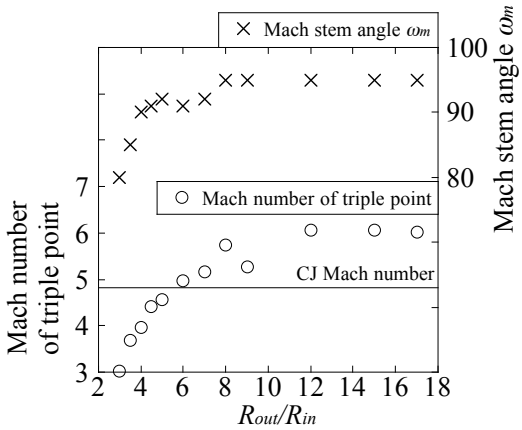

Fig. 4.16 Relation between R_{out}/R_{in}, Mach number of triple point and Mach stem angle ω_m.

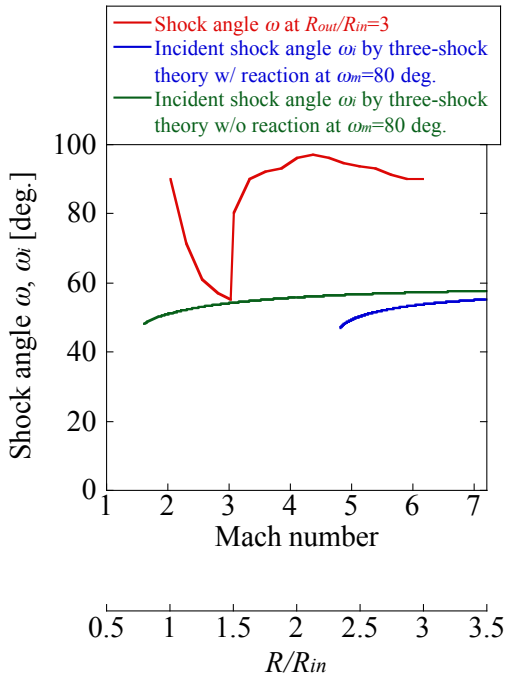

(a) $R_{out}/R_{in} = 3$

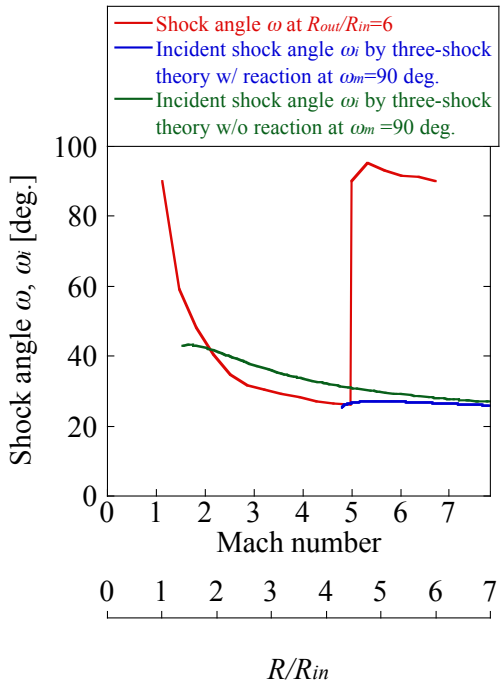

(b) $R_{out}/R_{in} = 6$

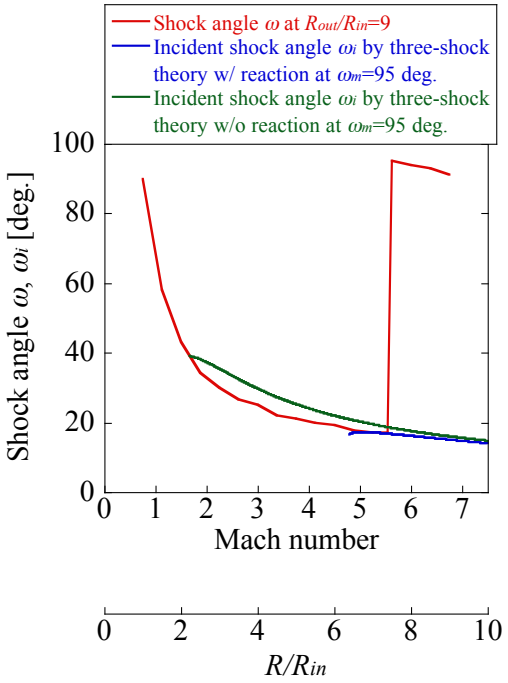

(c) $R_{out}/R_{in} = 9$

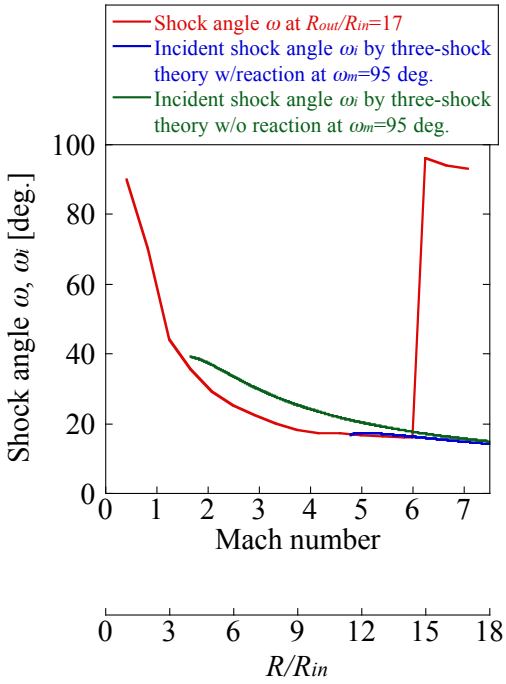

(d) $R_{out}/R_{in} = 17$

Fig. 4.17 Shock angles ω from the simulated data and incident shock angles ω_i by three-shock theories with and without chemical reaction in cases of (a) $R_{out}/R_{in} = 3$, (b) $R_{out}/R_{in} = 6$, (c) $R_{out}/R_{in} = 9$ and (d) $R_{out}/R_{in} = 17$.

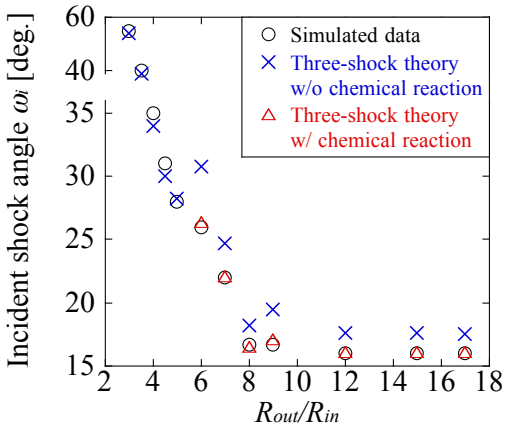

Fig. 4.18 Relation between R_{out}/R_{in} and incident shock angle ω_i of simulated data, three shock theories w/o and w/ chemical reaction.

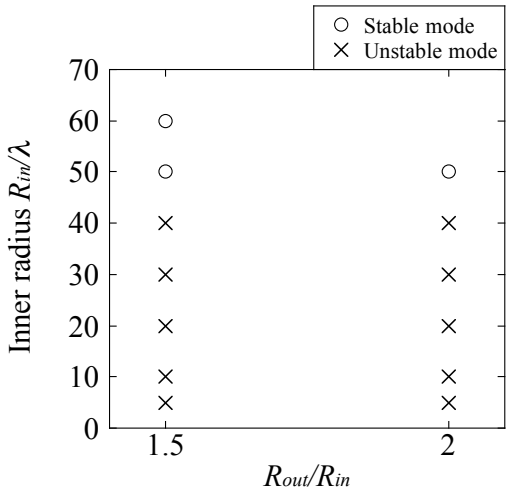

Fig. 4.19 Calculation parameters of ratio of outer and inner radius R_{out}/R_{in} and inner radius R_{in}/λ. Two detonation modes are observed; one is stable mode (○) and the other is unstable mode (×).

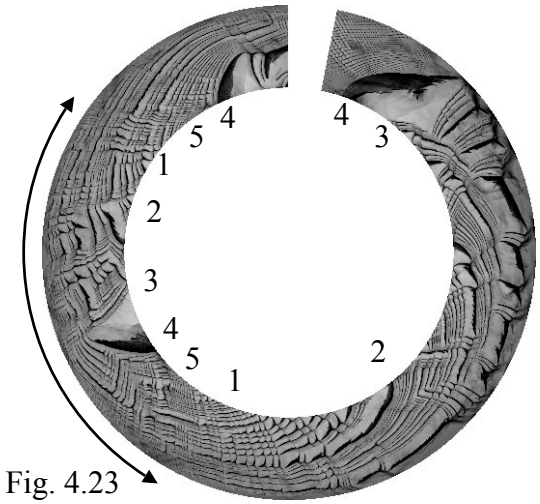

Fig. 4.23

(a)

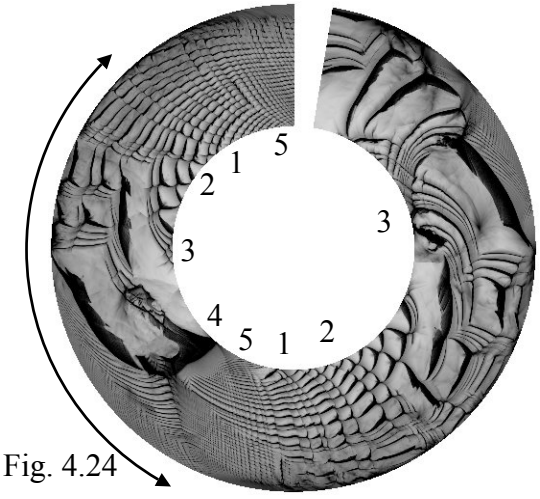

Fig. 4.24

(b)

Fig. 4.20 Soot track images using the maximum pressure histories of (a) $R_{in}/\lambda = 40$ at $R_{out}/R_{in} = 1.5$ and (b) $R_{in}/\lambda = 20$ at $R_{out}/R_{in} = 2$.

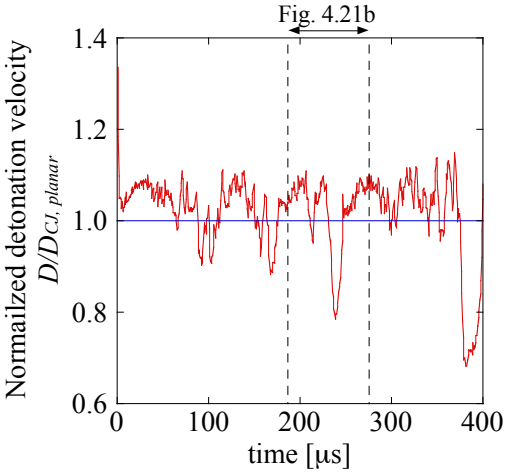

(a) Overview

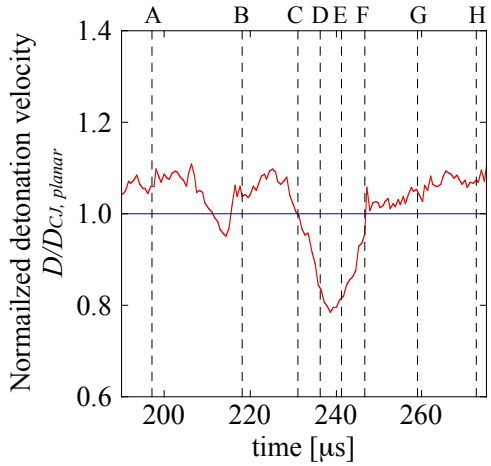

(b) Close up view of Fig. 4.21a

Fig. 4.21 Detonation velocity histories in a circumferential direction at the center of channel $R = (R_{out}+R_{in})/2$ in the case of $R_{in}/\lambda = 40$ at $R_{out}/R_{in} = 1.5$.

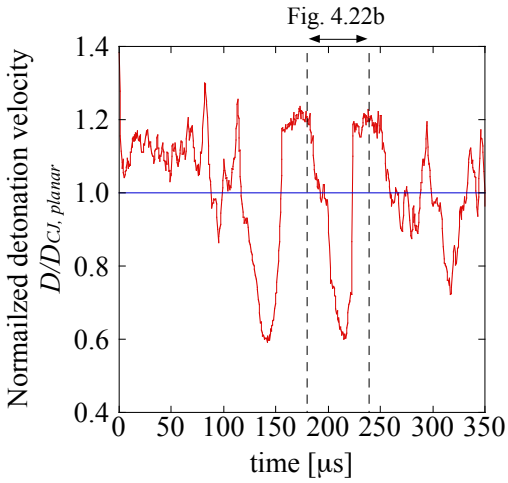

(a) Overview

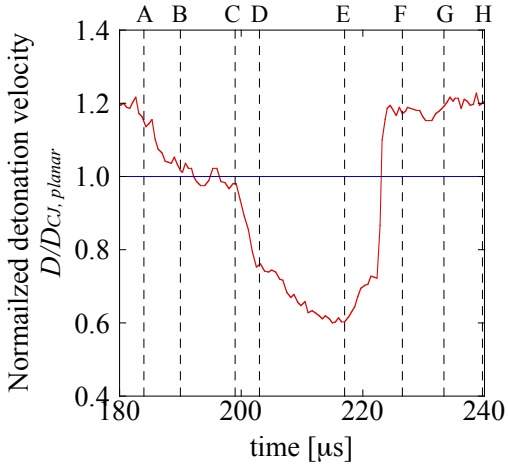

(b) Close up view of Fig. 4.22a

Fig. 4.22 Detonation velocity histories in a circumferential direction at the center of channel $R = (R_{out}+R_{in})/2$ in the case of $R_{in}/\lambda = 20$ at $R_{out}/R_{in} = 2$.

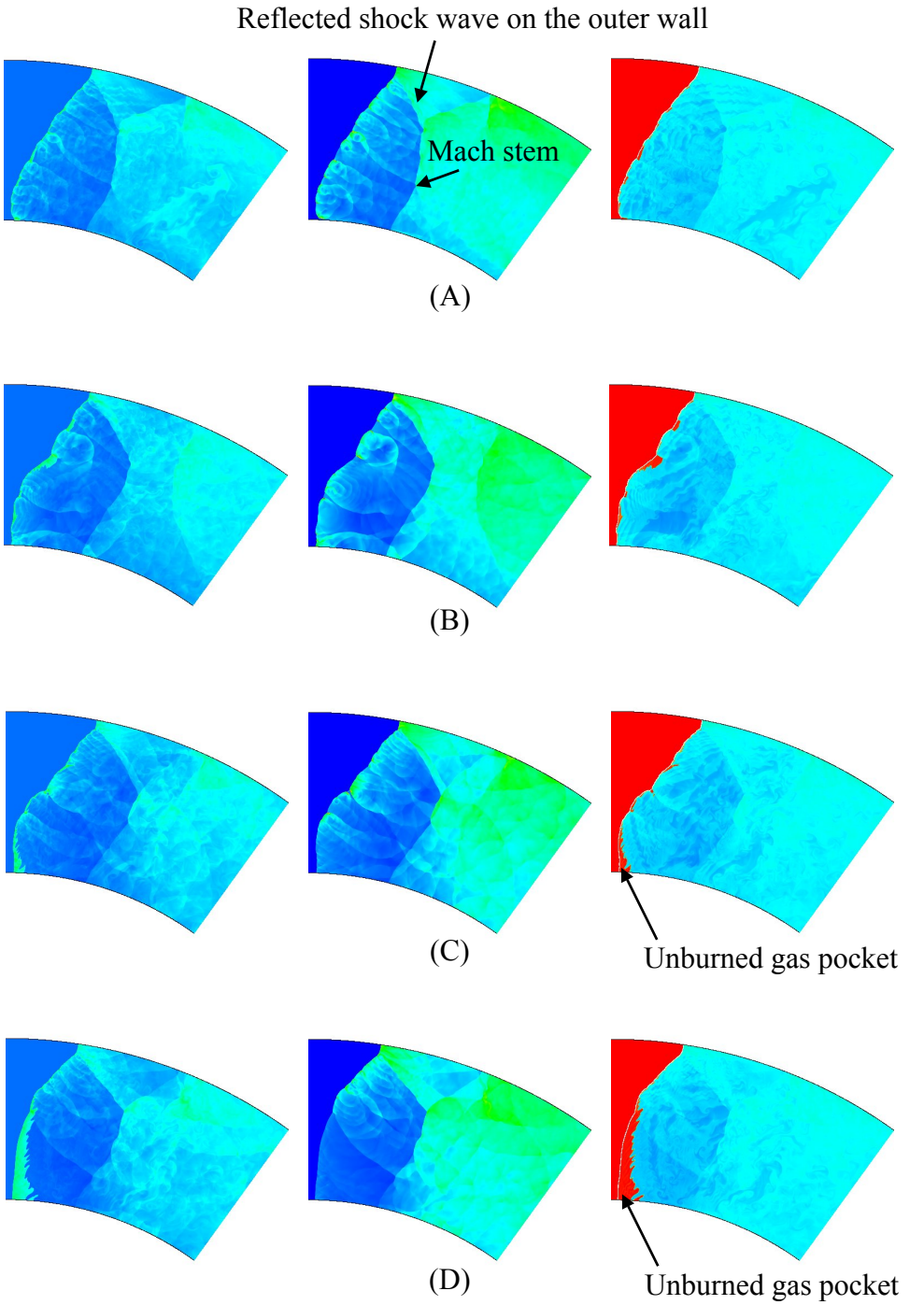

Fig. 4.23 Instantaneous distributions A – H of (a) density ρ, (b) pressure P and (c) mass fraction of reactant β in the case of $R_{in}/\lambda = 40$ at $R_{out}/R_{in} = 1.5$.

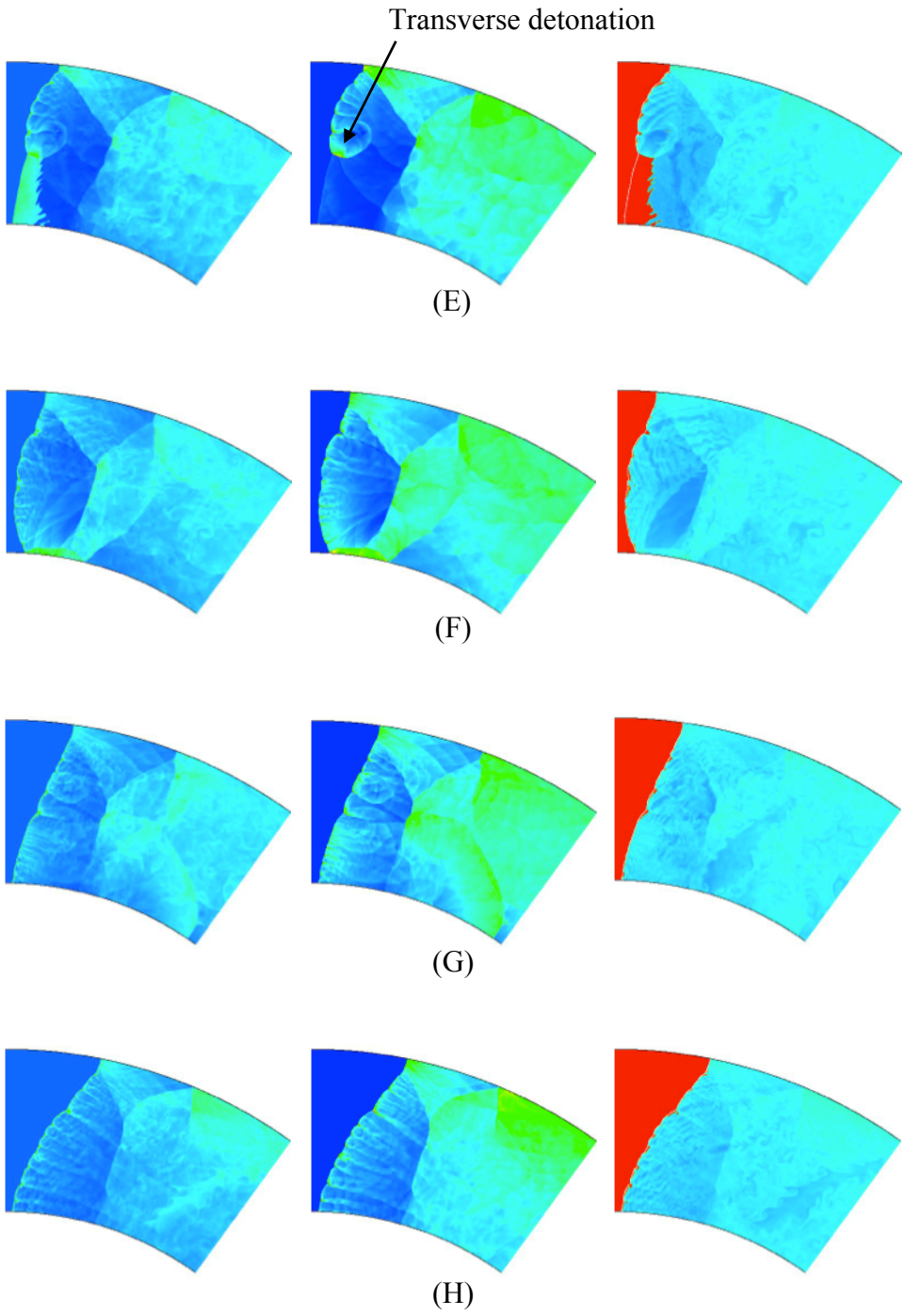

Fig. 4.23(cont.) Instantaneous distributions A – H of (a) density ρ, (b) pressure P and (c) mass fraction of reactant β in the case of $R_{in}/\lambda = 40$ at $R_{out}/R_{in} = 1.5$.

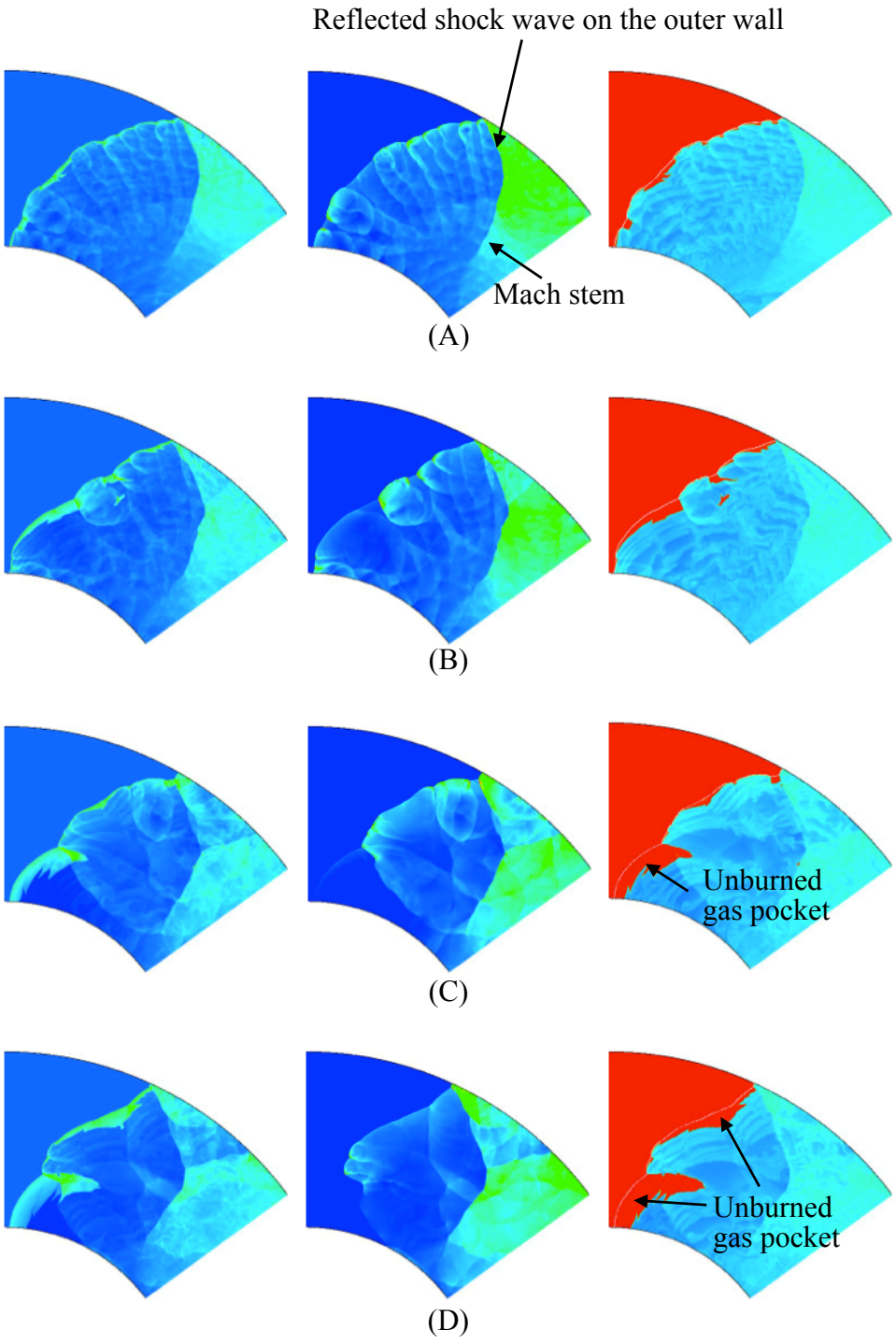

Fig. 4.24 Instantaneous distributions A – H of (a) density ρ, (b) pressure P and (c) mass fraction of reactant β in the case of $R_{in}/\lambda = 20$ at $R_{out}/R_{in} = 2$.

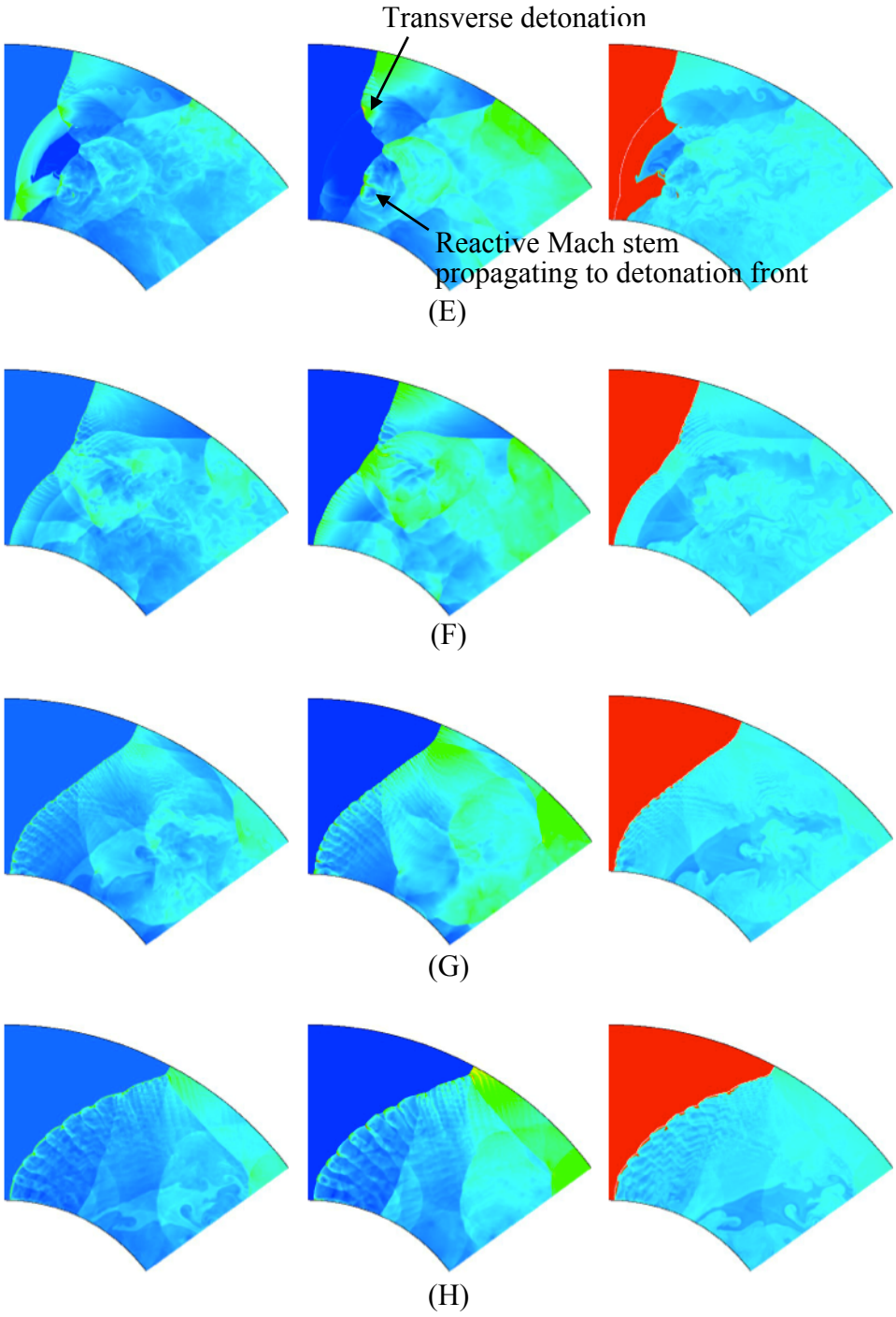

Fig. 4.24(cont.) Instantaneous distributions A – H of (a) density ρ, (b) pressure P and (c) mass fraction of reactant β in the case of $R_{in}/\lambda = 20$ at $R_{out}/R_{in} = 2$.

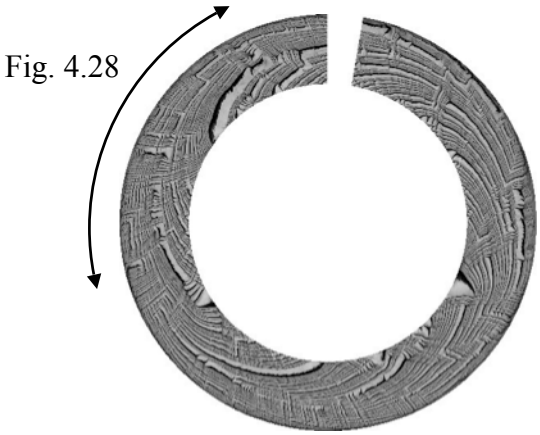

(a)

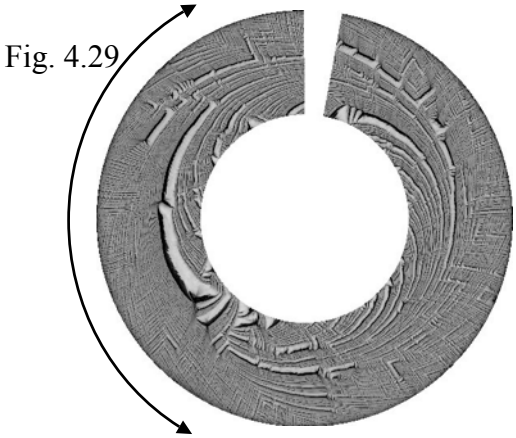

(b)

Fig. 4.25 Soot track images using the maximum pressure histories in cases of (a) R_{in}/λ = 60 at R_{out}/R_{in} = 1.5 and (b) R_{in}/λ = 50 at R_{out}/R_{in} = 2.

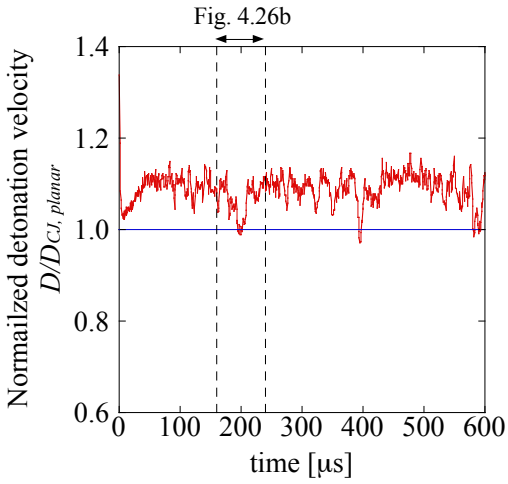

(a) Overview

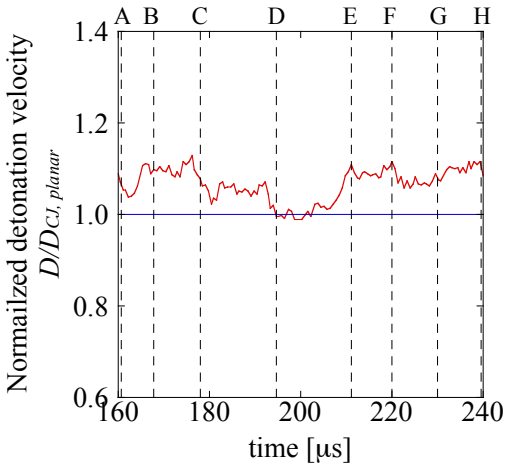

(b) Close up view of Fig. 4.26a

Fig. 4.26 Detonation velocity histories in a circumferential direction at the center of channel $R = (R_{out}+R_{in})/2$ in the case of $R_{in}/\lambda = 60$ at $R_{out}/R_{in} = 1.5$.

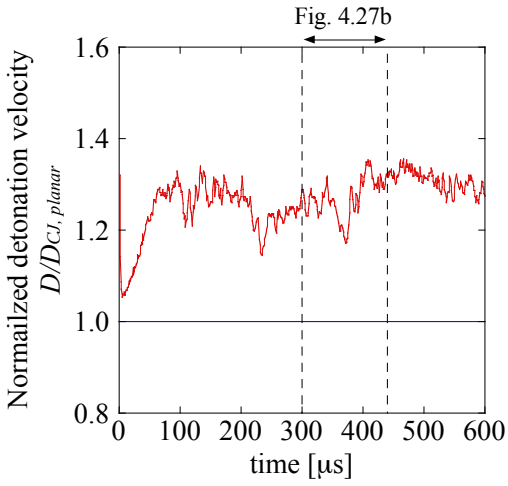

(a) Overview

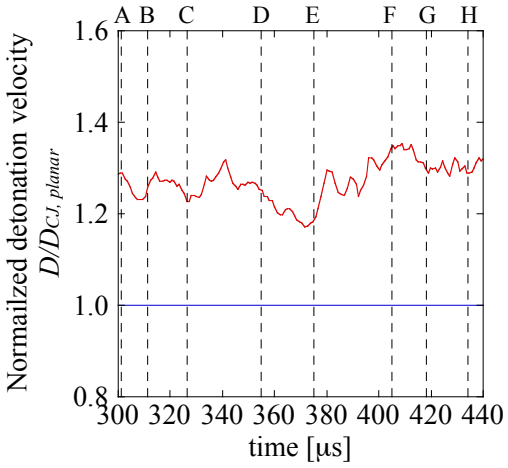

(b) Close up view of Fig. 4.27a

Fig. 4.27 Detonation velocity histories in a circumferential direction at the center of channel $R = (R_{out}+R_{in})/2$ in the case of $R_{in}/\lambda = 50$ at $R_{out}/R_{in} = 2$.

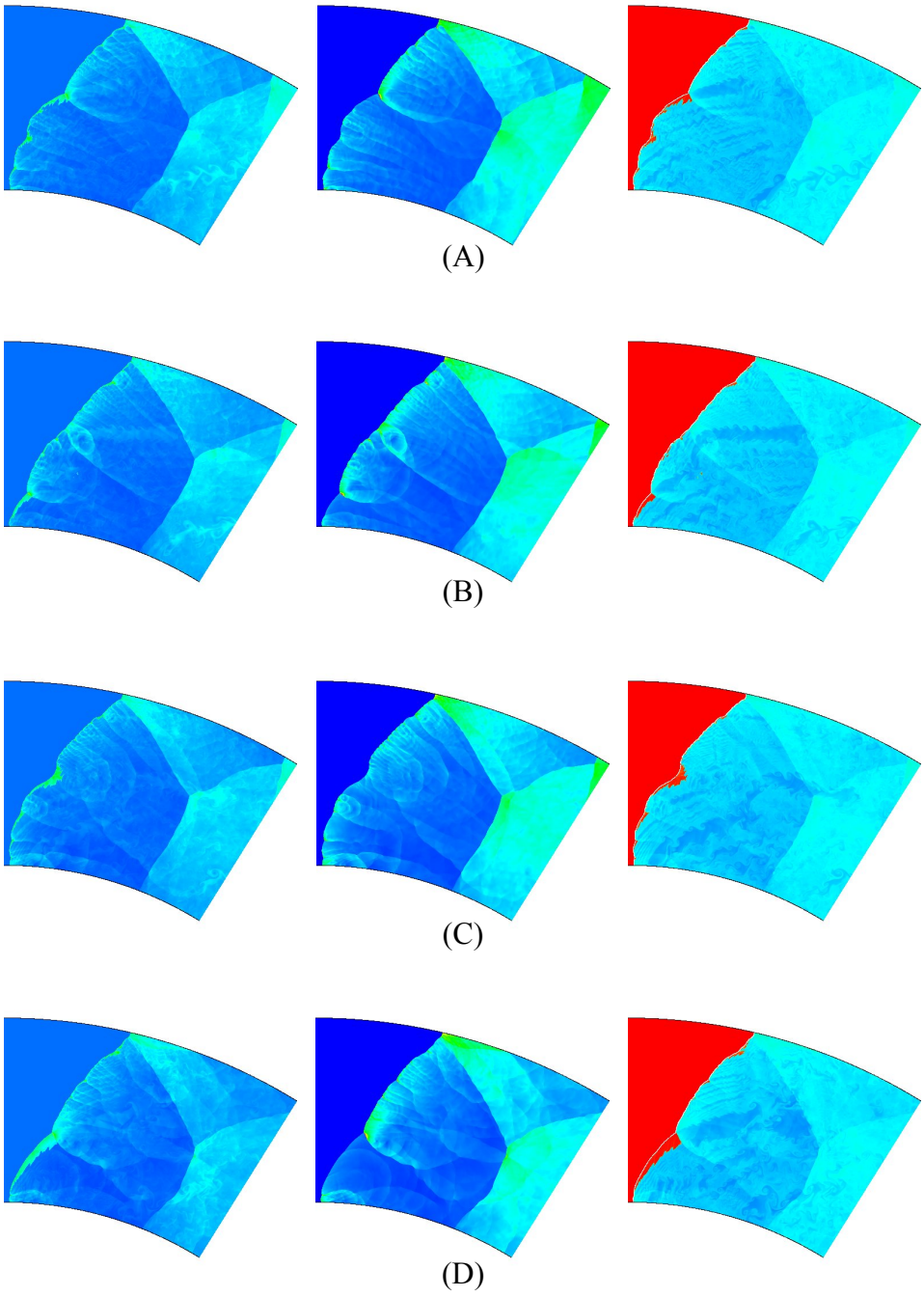

Fig. 4.28 Instantaneous distributions A – H of (a) density ρ, (b) pressure P and (c) mass fraction of reactant β in the case of $R_{in}/\lambda = 60$ at $R_{out}/R_{in} = 1.5$.

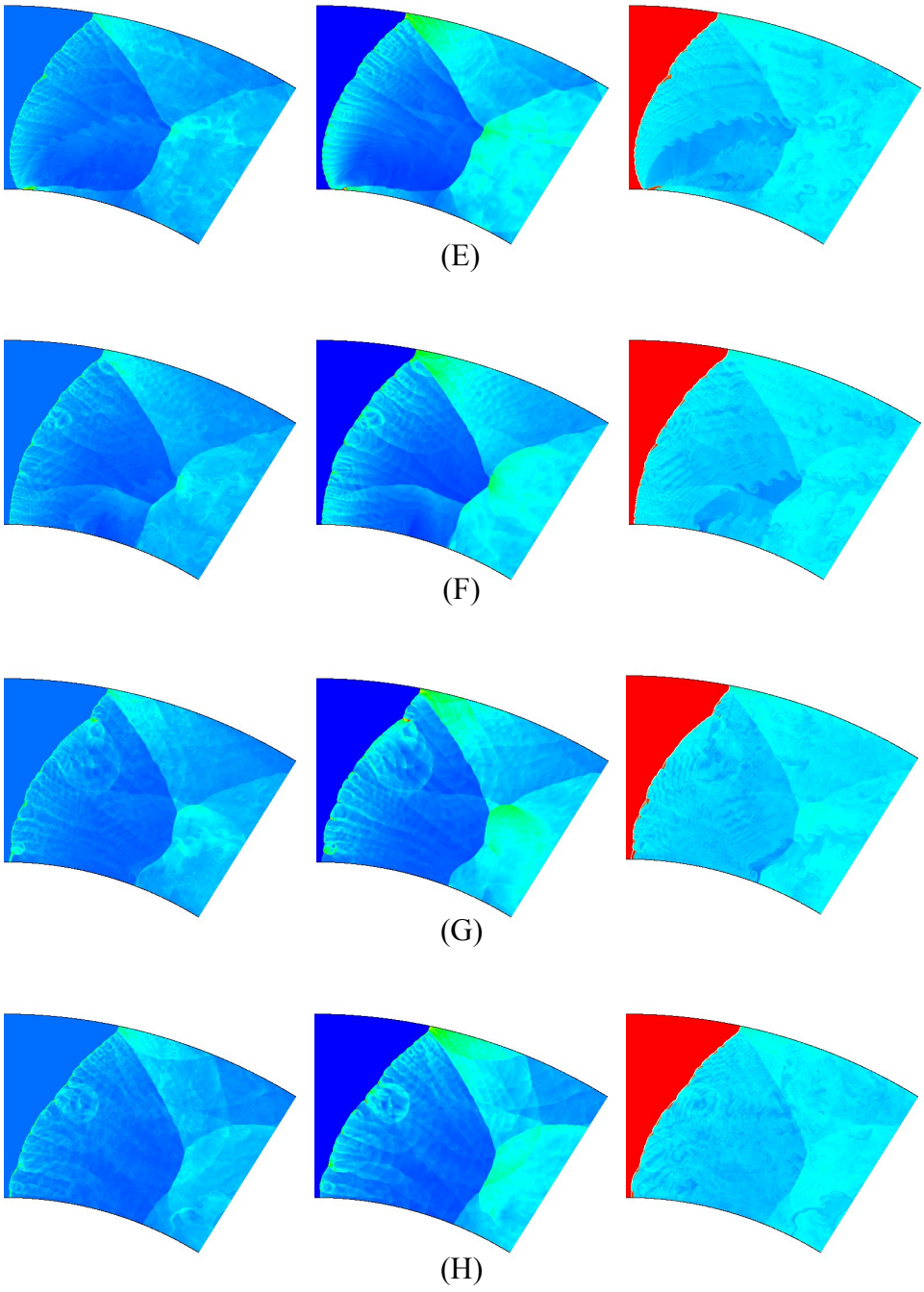

Fig. 4.28(cont.) Instantaneous distributions A – H of (a) density ρ, (b) pressure P and (c) mass fraction of reactant β in the case of $R_{in}/\lambda = 60$ at $R_{out}/R_{in} = 1.5$.

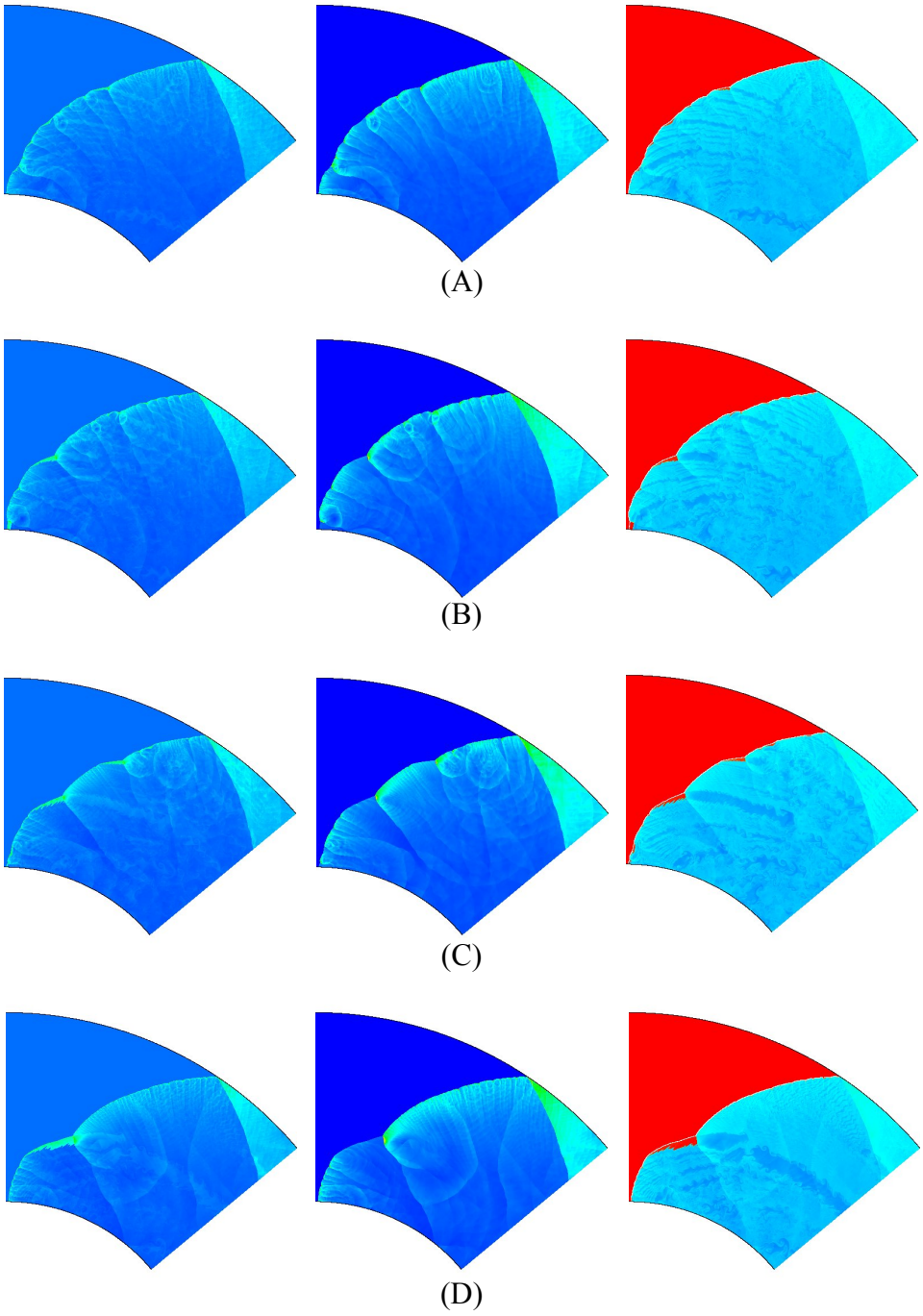

Fig. 4.29 Instantaneous distributions A – H of (a) density ρ, (b) pressure P and (c) mass fraction of reactant β in the case of $R_{in}/\lambda = 50$ at $R_{out}/R_{in} = 2$.

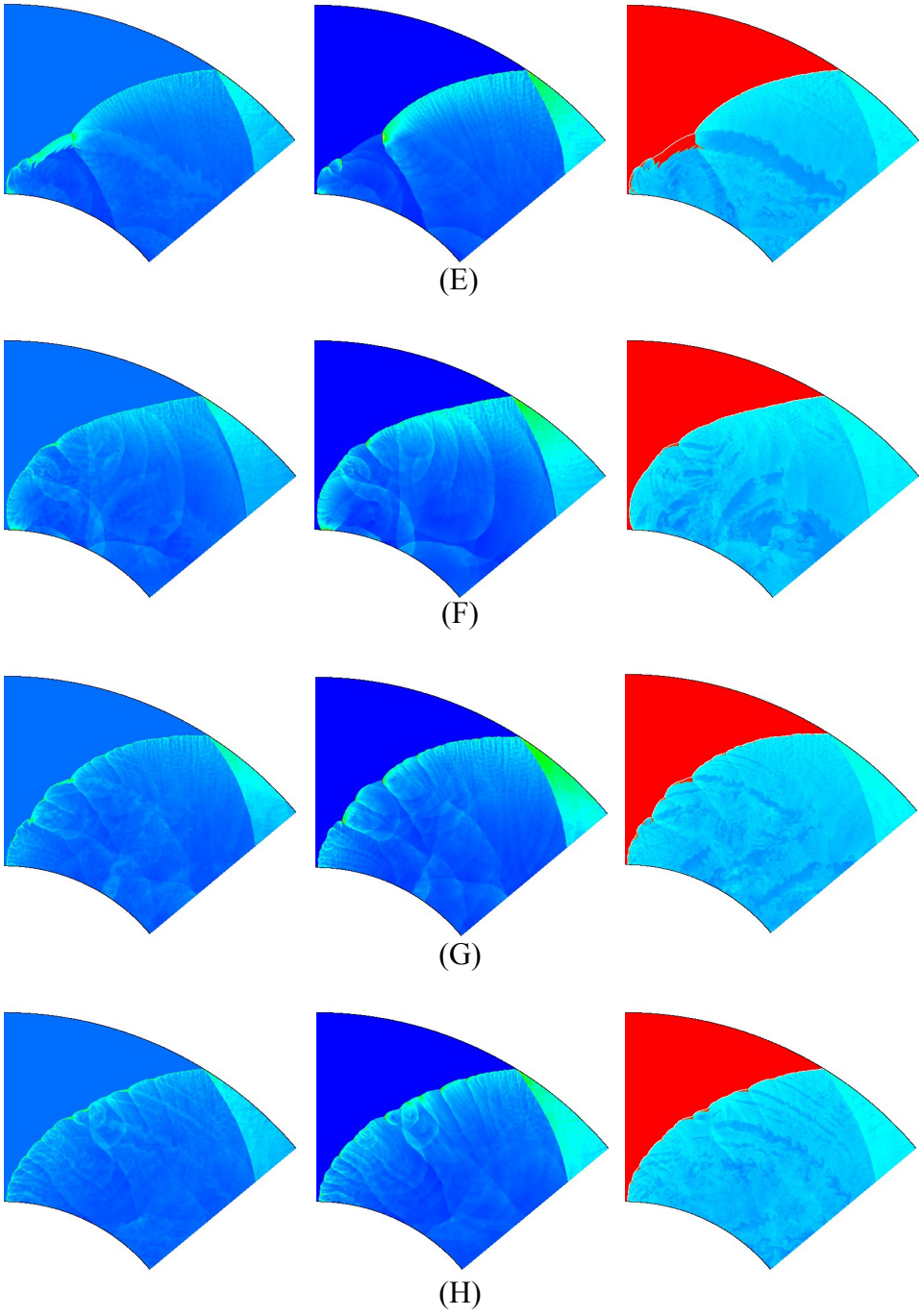

Fig. 4.29(cont.) Instantaneous distributions A – H of (a) density ρ, (b) pressure P and (c) mass fraction of reactant β in the case of $R_{in}/\lambda = 50$ at $R_{out}/R_{in} = 2$.

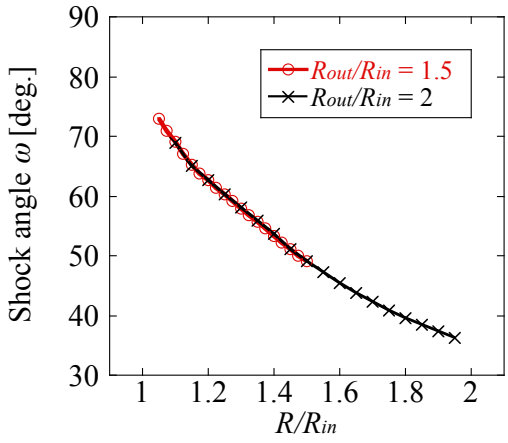

(a)

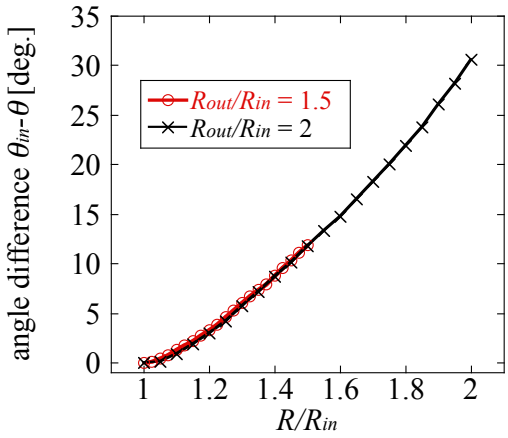

(b)

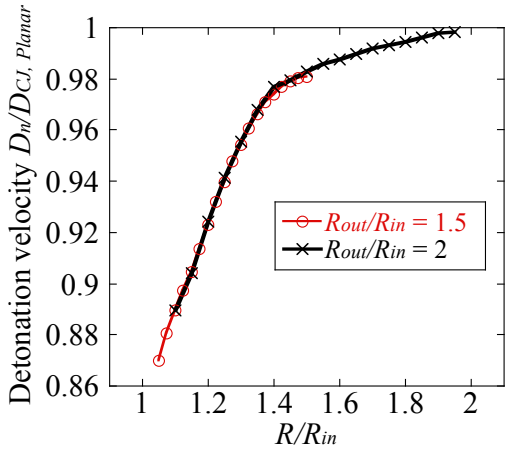

(c)

Fig. 4.30 Distributions of (a) shock angle ω, (b) angle difference $\theta_{in} - \theta$, and (c) the normal detonation velocity $D_n/D_{CJ,planar}$ on normalized radius R/R_{in}.

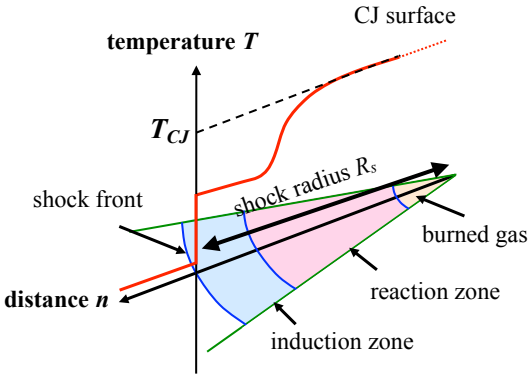

Fig. 4.31 Schematic picture of steady curved detonation with shock radius R_s.

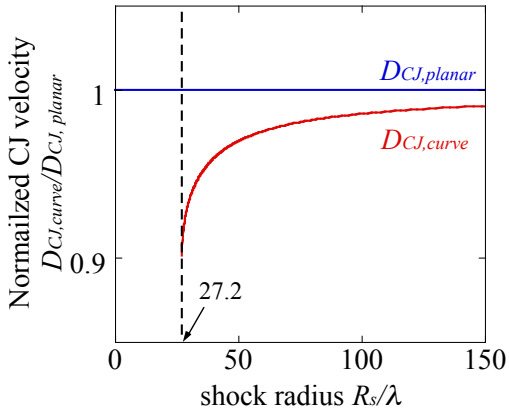

Fig. 4.32 Relation between shock radius R_s/λ and the CJ detonation velocity with curved shock front normalized with respect to planar CJ detonation velocity $D_{CJ,planar}$.

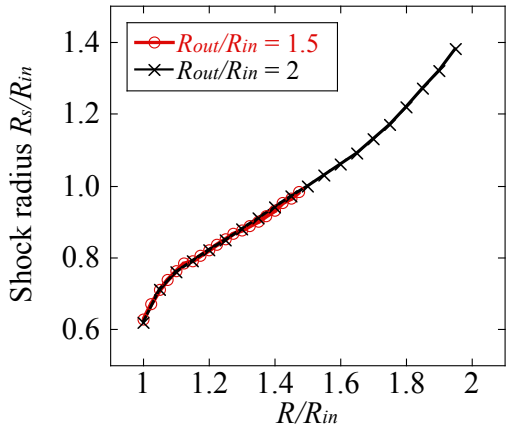

Fig. 4.33 Relation of the normalized radius R/R_{in} and shock radius R_s/λ in the case of stable mode at $R_{in}/\lambda = 60$ at $R_{out}/R_{in} = 1.5$ and $R_{in}/\lambda = 50$ at $R_{out}/R_{in} = 2$.

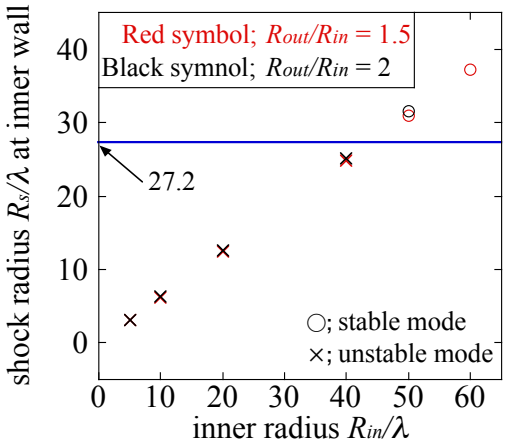

Fig. 4.34 Relation between propagation modes (○; stable mode and ×; unstable mode), inner radius R_{in}/λ and shock radius R_s/λ at inner wall. Blue line indicates R_s/λ = 27.2 calculated by quasi-steady solution. Red and Black symbols show the numerical results in cases of R_{out}/R_{in} = 1.5 and 2, respectively.

Chapter 5

Double cellular detonation in a two-dimensional straight channel

5.1. Introduction

In usual gaseous reactive mixtures (for instance, mixtures of H_2 or C_nH_m with O_2), detonation is characterized by a single cellular structure because the chemical energy is released in one step. Presles *et al.* [22] observed a double cellular structure in pure nitromethane and nitromethane-oxygen mixtures. They assumed that the double cellular structure could be associated with two characteristic chemical lengths during the process of heat release and the chemistry was supposed to proceed through two main steps. Investigations of double cellular detonation have been conducted [22-29] to reveal the propagation mechanism by the experiments and numerical simulations. Joubert *et al.* [23] showed soot track images of single and double cellular structure of the detonation of the H_2 - (NO_2/N_2O_4) mixture. They revealed that, in the case of fuel-rich condition, the detonation wave contains double cellular structures with small and large patterns and the ratio of two cell widths is over 10 in the experiments. They [28] also calculated one-dimensional steady detonation with detailed chemical reaction model and showed that the chemical energy is released in two successive exothermic steps inside the reaction zone in the case of fuel-rich condition. Each exothermic process has its chemical induction length, and their induction lengths differ at least by

one order of magnitude as well as the ratio between two cell widths by the experiment [23]. Desbordes *et al*. [27] evaluated the detonability on the basis of critical conditions of double cellular self-sustained detonations transmission from a cylindrical tube to free space. Guilly *et al.* [26] simulated a two-dimensional unsteady detonation with two successive exothermic reaction models and gave qualitative results in agreement with experimental ones. Virot *et al.* [29] calculated three-dimensional detonations with two successive exothermic reactions in order to discuss the influence of tube diameter. However, its characteristics are not well understood.

In Chapter 5, I investigate to clarify the cellular structure and the instability of double cellular detonation using two successive exothermic reactions model by two-dimensional simulations. The detailed discussions are conducted with the time evolutions of the simulated results and soot track images. The effect of two successive reactions is investigated to reveal the instability of double cellular detonation.

5.2. Numerical setup

The governing equations are the compressible and reactive two-dimensional Euler equations (5.1). The fluid is an ideal gas with constant specific heat ratio as shown in Eqs. (5.2) and (5.3), and all diffusion terms are neglected. The chemistry is modeled as two successive exothermic reactions steps A $\rightarrow$ B $\rightarrow$ C, which are governed by Arrhenius kinetics as shown in Eqs. (5.4) and (5.5). I use physical values such as cell width and half reaction length with subscripts 1 and 2 caused by the first and second steps in two successive reactions. Here, ρ, u, v, P, e and T are the density, velocity in x

and y directions, pressure, total energy per volume and temperature, respectively. Variable parameters a, b and c are mass fractions of reactant, intermediate and product, respectively, and the mass fraction of the intermediate is calculated as $b = 1\text{-}a\text{-}c$. E_i and K_i in Eqs. (5.4) and (5.5) are the activation energy and pre-exponential factor of i-th reaction. Parameters in Ref. [26] are described as follows. Initial pressure, temperature and specific heat ratio are $P_1 = 5$ kPa, $T_1 = 293$ K and $\gamma = 1.25$. The molecular weight is $W = 30.3$ kg/kmol, and pre-exponential factors of the first and second reactions are $K_1 = 4.5\times10^{11}$ m^3/(kg·s) and $K_2 = 3.0\times10^{8}$ m^3/(kg·s), respectively. Gas constant is $R = 8.314$ J/mol/K, and the activation energies and heat releases are the same for both steps: $E_1 = E_2 = 250$ kJ/mol and $Q_1 = Q_2 = 2.2$ MJ/kg. For these conditions, the Chapman-Jouguet detonation velocity and Mach number are 2270 m/s and 7.16, respectively.

$$\mathbf{Q} = \begin{bmatrix} \rho \\ \rho u \\ \rho v \\ e \\ \rho a \\ \rho c \end{bmatrix}, \quad \mathbf{E} = \begin{bmatrix} \rho u \\ \rho u^2 + P \\ \rho uv \\ (e+P)u \\ \rho au \\ \rho cu \end{bmatrix}, \quad \mathbf{F} = \begin{bmatrix} \rho v \\ \rho vu \\ \rho v^2 + P \\ (e+P)v \\ \rho av \\ \rho cv \end{bmatrix}, \quad \mathbf{S} = \begin{bmatrix} 0 \\ 0 \\ 0 \\ 0 \\ \omega_a \\ \omega_c \end{bmatrix}, \tag{5.1}$$

$$e = \frac{P}{\gamma - 1} + \rho Q_1 a - \rho Q_2 c + \frac{1}{2}\rho\left(u^2 + v^2\right), \tag{5.2}$$

$$P = \rho RT, \tag{5.3}$$

$$\omega_a = -\rho^2 K_1 a \exp\left(-\frac{E_1}{RT}\right) \tag{5.4}$$

and

$$\omega_c = \rho^2 K_2 b \exp\left(-\frac{E_2}{RT}\right). \tag{5.5}$$

Figure 5.1 shows distributions of (a) the mass fraction of reactant, intermediate and product and (b) the density and temperature calculated by the one-dimensional steady solution. Half reaction lengths for first (L_1) and second (L_2) steps are defined as the length between the shock front and the point that the mass fraction of reactant and product becomes 0.5 as shown in Fig. 5.1a and are 0.275 mm and 13.9 mm, respectively. I define the grid resolution as the grid points in the half reaction length in the first step L_1, and grid size varies from 6 to 400 μm, which correspond to 47 and 2 points in L_1. Figure 5.1b shows the transition point (dashed line with the notation 1/2) between the first and second steps. Its physical values are denoted with subscript 1/2, and temperature and density are $T_{1/2}$ = 3651 K and $\rho_{1/2}$ = 0.24 kg/m^3, respectively.

The computational grid is an orthogonal system, and channel width L is varied from as 15 to 1800 mm. The boundary conditions are as follows: premixed gas with CJ velocity flows from the left boundary in order to reduce the number of grid points, the adiabatic and slip conditions are imposed at the upper and lower boundary, and the downstream condition is the boundary proposed by Gamezo *et al.* [19]. The results of

one-dimensional steady detonation in Fig. 5.1 are used for an initial flow distribution, where sheets of unburned gas mixture are artificially added behind detonation front in order to create initial disturbances. As discretization methods, Yee's Non-MUSCL Type 2nd-Order TVD Upwind Scheme [56] is used for the spatial integration, and the point-implicit method that treats only source term implicitly is used for the time integration.

5.3. Results and discussion

5.3.1. Double cellular detonation structure

The soot tracks recorded on the tube in previous experiments have showed the remarkable insight for the propagation mechanism. Figure 5.2 shows the soot track image created by the maximum pressure history in the case of channel width L = 200 mm. The image shows agreement with the previous experimental and numerical observations. Distance x starts leftward at the point of the collision of triple points at the center of the channel, drawn with a white dashed line. Figure 5.3 shows instantaneous distributions of (a) density and (b) mass fraction of product showing the process of the second reaction. White lines in Fig. 5.3b indicate the shock front. In Fig. 5.3a, two distinct transverse wave structures are observed, one is a couple of large transverse waves and the other is a large number of the fine transverse waves. They are supposed to be originated from successive first and second reactions, and to make the double cellular detonation as shown in Fig. 5.2. The first reaction seems to be instantaneously completed behind the shock front because channel width is much larger than its

chemical reaction length. However, the second reaction needs the longer distance to consume the intermediate as shown in Fig. 5.3b. Because cell width strongly depends on the reaction length such as half reaction length, small and large cells must be formed by the first and second reactions.

Here, I focus on the cell widths λ_1 and λ_2, quantitatively. In Fig. 5.2, a very fine cellular pattern is observed at 150 mm < x < 370 mm inside the large cell, and the cell size of the fine cellular pattern grows toward the end of the large cell at x = 370 mm. Figure 5.4 shows the change of the cell width λ_1 along the distance x in Fig. 5.2, and the cell width λ_1 gradually increases from 2.87 to 9.01 mm. In general, the leading shock velocity in a detonation cell changes from overdriven to underdriven between collisions of triple points; that is to say the half reaction length also becomes short to large in one cycle of detonation cell. Therefore, the cell width λ_1 formed by the first reaction is varied and cannot be estimated as a unique value. The large cell width λ_2 in Fig. 5.2 is estimated as 200 mm, which is equal to the channel width. Since the cell width strongly depends on the channel width in the case of narrow channel width, I conduct calculations with larger channel widths 600, 1000 and 1800 mm under less resolution than that in Fig. 5.2. The averaged cell width λ_2 with larger channel widths is calculated as 171 mm < λ_2 < 222 mm, and therefore λ_2 = 200 mm is appropriate for the cell width. Using two cell widths of 2.86 mm < λ_1 < 9.01 mm and λ_2 = 200 mm, the ratio of cell widths is estimated as 22.2 < λ_2/λ_1 < 69.9, which qualitatively agrees with that of half reaction length (L_2/L_1 = 50.5). Previous experimental observations [23, 25] also showed one

order of magnitude of two reaction lengths. Therefore, The above investigation suggests that two successive reaction processes are independent each other.

5.3.2. Detonation physics of two successive reactions

Double cellular detonation is caused by two successive exothermic steps having very different characteristic chemical reaction lengths. In this section, I divide double cellular detonation with two successive reactions into two detonations with a single reaction. Figure 5.5 shows the schematics of Rayleigh line and Hugoniot curves of double detonation structure on P–V plane. Points indicate as follows; A: initial state, vN: von Neumann state, 1/2: transition from the first to the second reaction, CJ: CJ state, and D: hypothetical initial state. Table 5.1 shows the pressure and specific volume at points A, vN, 1/2, CJ and D in Fig. 5.5. Hugoniot curves l_1, l_2 and l_3 denotes conditions of the adiabatic ($Q = 0$), the end of the first reaction ($Q = Q_1$) and the end of second reaction ($Q = Q_1+Q_2$), respectively. The solution moves along Hugoniot curve l_1 for the leading shock wave as A $\rightarrow$ vN and Rayleigh line for two successive reactions vN $\rightarrow$ 1/2 $\rightarrow$ CJ. In the present reaction parameters, the second reaction starts after the first reaction is completed. Therefore, I divide successive processes into each one. From the initial state to the end of the first reaction, the solution varies as A $\rightarrow$ vN $\rightarrow$ 1/2. In this process, overdriven detonation appears and is defined as “primary detonation”. During the second reaction, the solution varies as 1/2 $\rightarrow$ CJ without leading shock wave. Here, I put the hypothetical initial state D in Fig. 5.5 and assume that solution varies D $\rightarrow$ 1/2 along the Hugoniot curve l_2 by the hypothetical leading shock wave. I obtain

"secondary detonation", whose solution varies as D → 1/2 → CJ. In order to investigate the chemical characteristics of double, primary and secondary detonation, the temperature gradients of these detonations are obtained by the one-dimensional steady solutions in Fig. 5.6. The profile of double detonation is successfully divided into those of primary and secondary ones. Indeed, half reaction lengths of primary (L_p = 0.275 mm) and secondary (L_s = 13.6 mm) detonations also agree well with L_1 and L_2 - L_1, respectively.

In order to clarify the interaction between the first and the second reactions in double cellular detonation, cell widths are numerically obtained by the simulated results of two-dimensional unsteady primary and secondary detonations. I use the subscripts *p* and *s* to express physical values of the primary and secondary detonations, respectively. Grid resolution for simulations of primary and secondary detonations is sufficient because 47 point in L_p and 33 points in L_s are prepared. Figure 5.7 shows the soot track images at the condition of (a) primary and (b) secondary detonations, at channel widths L = 15 and L = 1800 mm, respectively. Averaged cell widths λ_p and λ_s in Fig. 5.7 are estimated as 3.75 and 200 mm, which agrees well with those formed by the first (2.87 mm < λ_1 < 9.01 mm) and the second reaction (λ_2 = 200 mm) in the double detonation. The ratio of cell widths (λ_s/λ_p = 53.3) also agrees well with that of the half reaction lengths L_s/L_p = 49.5 and L_2/L_1 = 50.5. Our simulations successfully demonstrate that the primary and secondary detonations are characterized by the first and the second reactions in double detonation, individually. Double cellular detonation is divided into two detonations with a single exothermic reaction by means of the addition of the

hypothetical condition for intermediate initial state of Rayleigh line and Hugoniot curves. This idea easily explains the critical diameter of double cellular detonation simulated by Virot *et al*[29].

Linear stability analysis [50-52] has been studied so as to investigate one-dimensional longitudinal unsteadiness. Figure 5.8 [51] is the neutral stability curve for planar detonation classified by the Mach number of detonation and effective activation energy defined as $\theta = E/RT_{vN}$ with one-step Arrhenius rate law. The conditions of the first and second reaction of double detonation, and primary and secondary detonations are plotted in Fig. 5.8, as denoted by First, Second, Primary and Secondary. First and Primary are located at the identical position, which indicates that instability of detonation and the irregularity of cellular pattern must be the same. The soot track image of primary detonation in Fig. 5.7a shows irregular cellular pattern as well as those by Vasil'ev *et al.* [49] and Gamezo *et al.* [19] due to the detonation instability. In the case of Second and Secondary, although the effective activation energy, which is estimated by the temperature at 1/2 in Fig. 5.5 ($T_{1/2}$ = 3651 K), is the same, Mach number of secondary detonation is smaller than that of double cellular detonation because of the disagreement on the initial temperature of secondary detonation (2350 K) and double one (293 K). Therefore, points of Second and Secondary are different, and moreover, the former is located in the unstable region, whereas the latter in stable region. Figure 5.9 shows the soot tracks at the double detonations at channel width (a) L = 15 mm and (b) L = 600 mm, respectively. The channel width in Fig. 5.9a is too narrow to see the cell caused by the second reaction, and therefore, cellular structure in

Fig. 5.9a is originated by the first reaction. The resolution in Fig. 5.9b is coarser than that in Fig. 5.2, and therefore, the first cells are resolved in the earlier stage in the large cell in the case of finer grid size in Fig. 5.2. Irregularity of cellular pattern by the first reaction in Fig. 5.9a shows good agreement with that by the primary detonation as shown in Fig. 5.7a. Figure 5.9b shows double cellular structure with the regular cellular pattern as well as Fig. 5.7b, although Second in Fig. 5.8 is located in the unstable region by the linear stability analysis. This indicates that the instabilities of primary and secondary detonations are dominant to those of double cellular detonation with two successive reactions. The simulated results lead to the conclusion that the introduction of the appropriate hypothetical condition to divide successive reactions is a useful procedure to estimate the detonation instability and its cellular structure.

5.4. Summary

Double cellular detonations propagating in two-dimensional straight channel were numerically investigated with two successive reaction models governed by Arrhenius rate law whose chemical energy is released in two successive steps of different characteristic times and lengths. Soot track image shows good agreement with that of previous experiments and numerical simulations. Two cell widths λ_1 and λ_2 in double cellular detonation are formed by first and second reactions. The ratio of cell widths (λ_2/λ_1) qualitatively agrees with that of half reaction lengths (L_2/L_1). Double cellular detonation with two successive reactions is divided into two detonations, primary and secondary detonations with a single exothermic reaction, based on the relation of

Rayleigh line and Hugoniot curves with the addition of the hypothetical condition of the intermediate initial state. Half reaction lengths and temperature gradient of the primary and secondary detonations show good agreement with those of double cellular detonation. The ratio of cell widths λ_s/λ_p estimated by primary and secondary detonations shows good agreement with that (λ_2/λ_1) of double cellular detonation. This indicates that two successive chemical reactions proceed independently. The instabilities of double, primary and secondary detonations are investigated using soot track images and neutral stability curve of planar detonation. Simulated results shows that instabilities of the primary and secondary detonations are dominant to those by the first and second reactions of double detonation. It denotes that the introduction of the appropriate hypothetical condition to divide successive reactions is a useful procedure to estimate the detonation instability and its cellular structure.

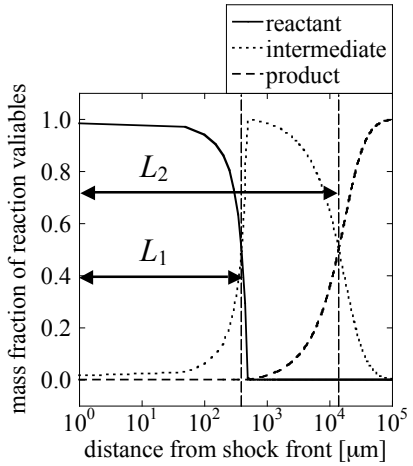

(a) mass fraction of reactant, intermediate and product

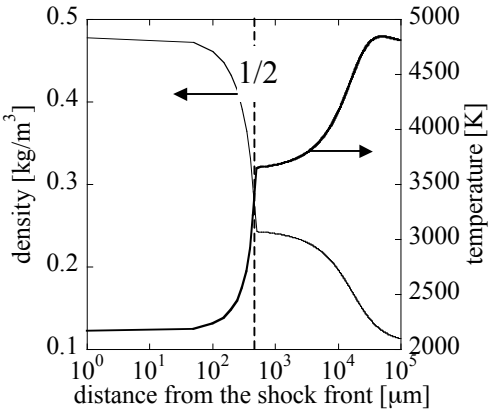

(b) density and temperature

Fig. 5.1 Distributions of (a) mass fractions of reactant, intermediate and product, and (b) of density and temperature calculated by the one-dimensional steady solution. L_i and 1/2 denote the half reaction length of i-th reaction and the transition point of the first and second reactions, respectively.

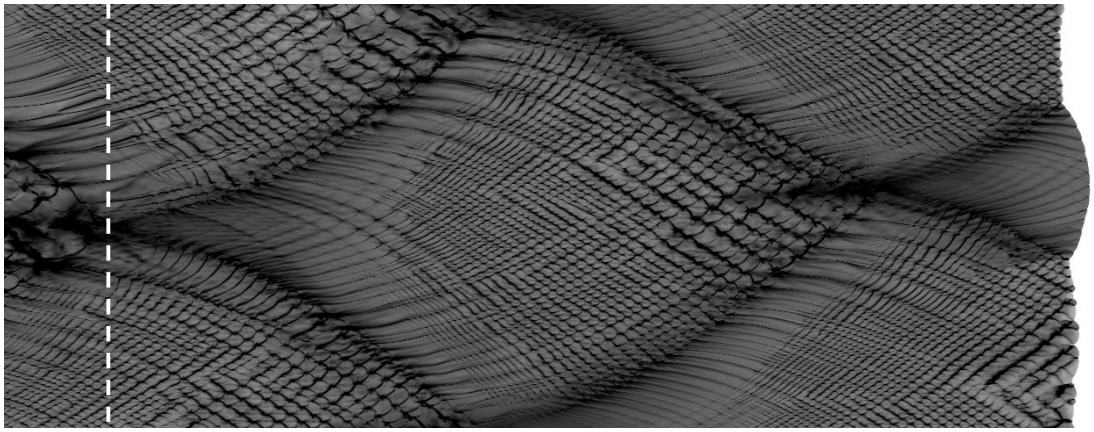

Fig. 5.2 Soot track image of double cellular detonation in the case of the channel width L = 200 mm.

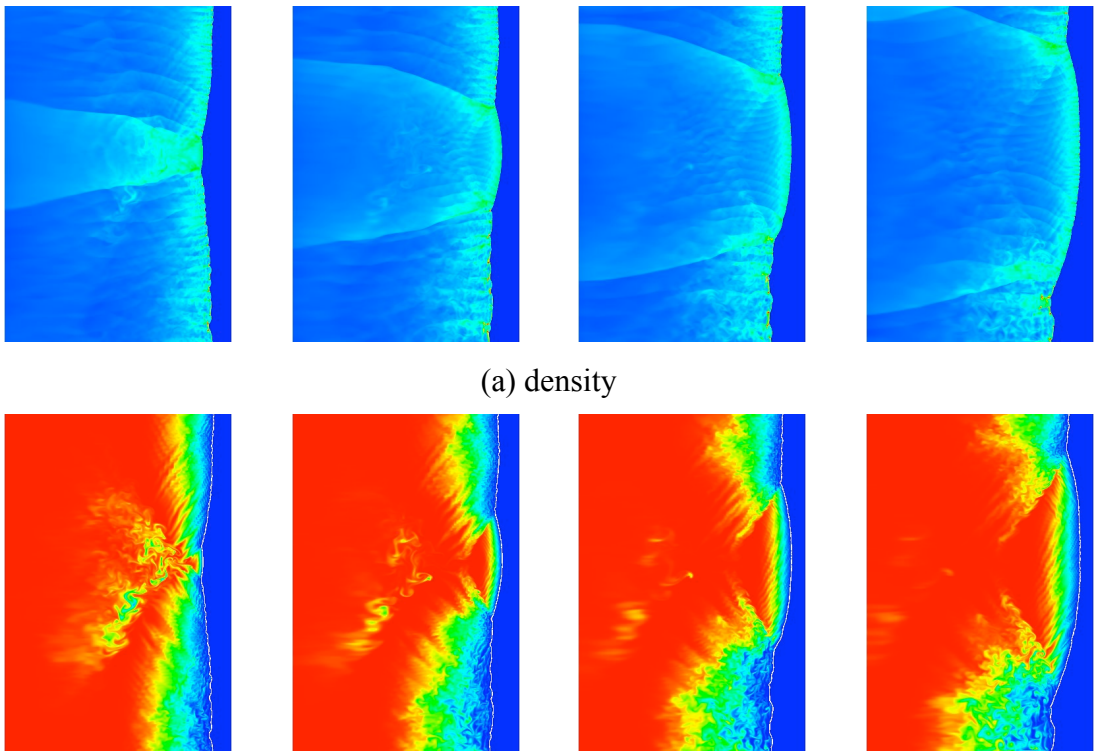

(a) density

(b) mass fraction of product

Fig. 5.3 Instantaneous distributions of (a) density and (b) mass fraction of product.

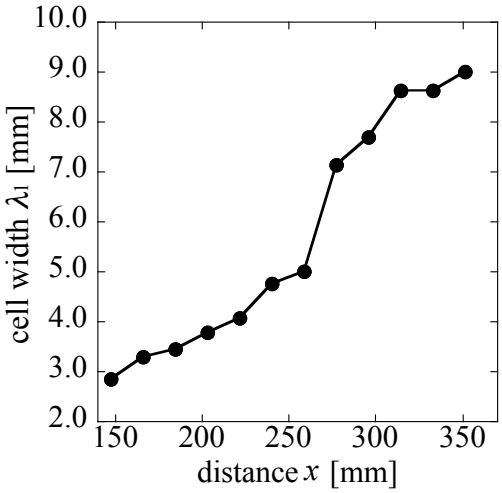

Fig. 5.4 The change of cell width λ_1 along the distance x.

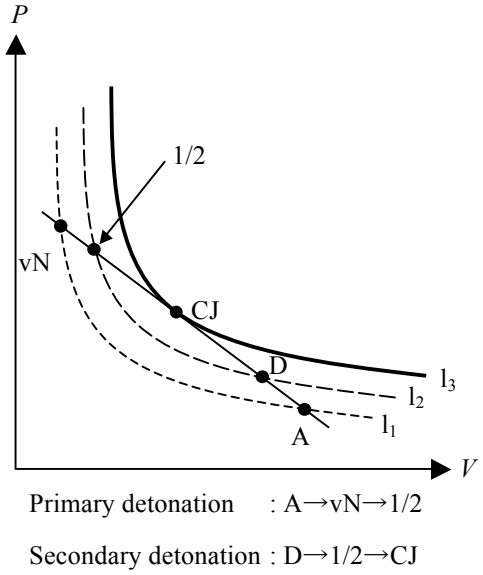

Fig. 5.5 Schematics of Rayleigh line and Hugoniot curves on P-V plane. A: initial state, vN: von Neumann point, 1/2: transition from the first to second reaction, CJ: CJ state and D: hypothetical initial state. Hugoniot curves l_1, l_2 and l_3 denotes conditions of the adiabatic (Q=0), the end of the first reaction (Q=Q_1) and the end of second reaction (Q=Q_1+Q_2), respectively.

Table 5.1

Pressure and specific volume at points A, vN, 1/2, CJ and D in Fig. 5.5.

point	pressure [atm]	specific volume [m^3/kg]
A	0.050	16.1
vN	2.842	2.07
1/2	2.412	4.15
CJ	1.478	8.93
D	0.455	14.2

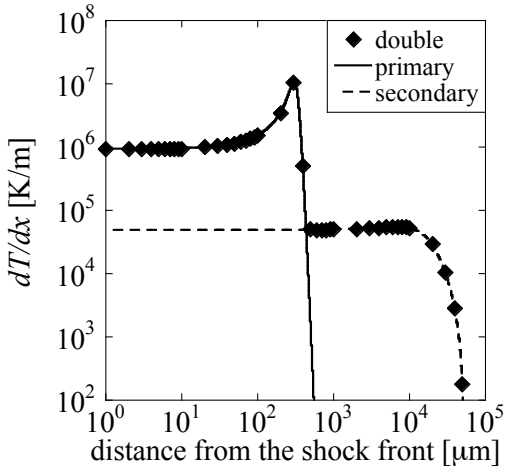

Fig. 5.6 Temperature gradient of double, primary and secondary detonation by the one-dimensional steady solutions.

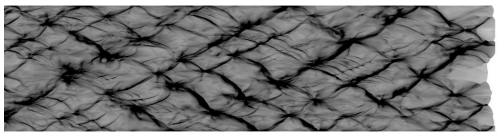

(a) primary detonation

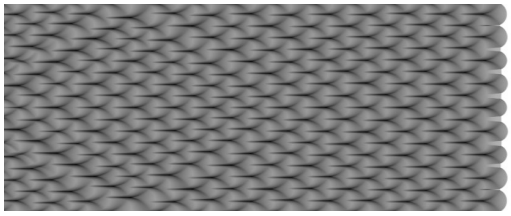

(b) secondary detonation

Fig. 5.7 Soot track images of (a) primary and (b) secondary detonations, at channel widths L = 15 mm and L = 1800 mm, respectively.

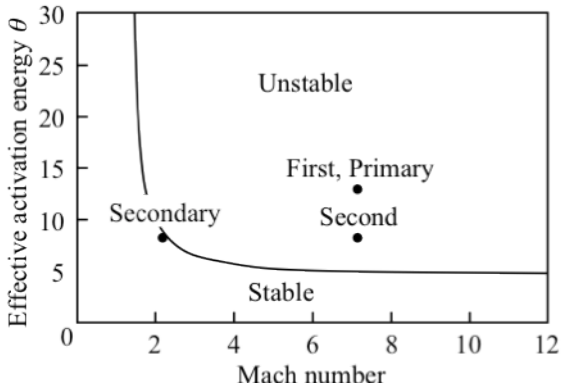

Fig. 5.8 Neutral stability curve for planar detonations with one-step Arrhenius rate law.

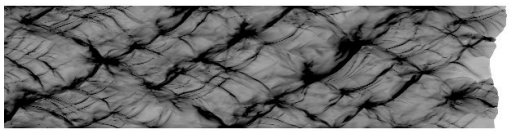

(a) cellular structure formed by the first reaction

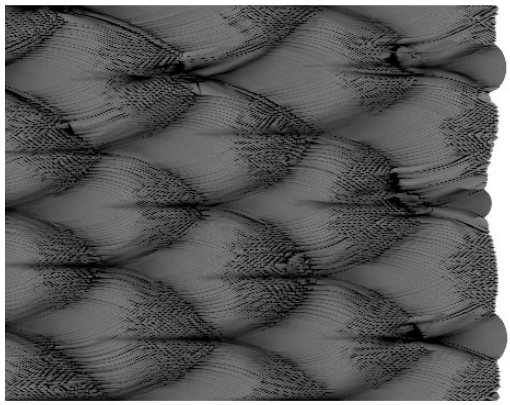

(b) cellular structure formed by the second reaction

Fig. 5.9 Soot track images of double cellular detonations at channel widths (a) L = 15 mm and (b) L = 600 mm.

Chapter 6

Conclusion

The present research focuses on the propagation behaviors of detonations by two- and three-dimensional numerical simulations using Euler equations.

In Chapters 2, the three-dimensional detonations are numerically investigated using A series of simulations are carried out in an attempt to understand the propagation behaviors of pulsating detonations in small square and circular tubes. The soot track image of pulsating detonation is numerically obtained using the maximum pressure history on the tube wall, which qualitatively agrees with the soot track of galloping detonation experimentally obtained by Vasil'ev. Numerical results show strong pulsations with the intermittent local explosion under cyclic behavior, where the detonation velocity varies from underdriven to overdriven in one cycle. At the initial stage of each pulsation, a new explosion occurs in the induction zone near the flame front, which develops the inner detonation. It overtakes the leading shock wave and creates a highly overdriven detonation wave. The overdriven wave induces multi-headed detonation and is gradually attenuated from the multi-headed mode to a single-headed spinning mode. After that, the spinning detonation disappears, and the shock wave separates from the flame front with increasing length of the induction zone. These processes are repeated in each pulsation. As the pulsating detonation shows strong oscillation in the longitudinal direction, the cross-sectionally averaged *x-t*

diagrams are compared with an *x-t* diagram of one-dimensional detonation. Flow features and characteristic values such as reignition time, the period of pulsating detonation, and the velocity of the failed regime in a circular tube agree with those of one-dimensional detonation. Therefore, it is concluded that longitudinal instability is dominant in pulsating detonation after the lack of a transverse wave.

In Chapter 3, spinning detonation in circular and square tubes are investigated in order to understand the effect of initial pressure and geometry size. Two distinct propagation modes are obtained namely steady mode, unstable mode in a circular tube. Steady mode shows stable propagation without change in the shock structure. The maximum pressure history of transverse detonation on the wall and velocity history of detonation remained nearly constant, and a Mach leg always existed on the shock front and rotated at a constant speed. Coupling with transverse detonation and acoustic wave is always satisfied. Meanwhile, unstable mode shows periodical change in the shock structure. Complex Mach interaction periodically appears due to periodical generation of transverse detonation. Its velocity history shows the fluctuation, which qualitatively agrees with that of rapid fluctuation mode by Lee *et al*. Coupling and decoupling with transverse detonation and acoustic wave is repeated, which induce the periodical flow field. In the case of pulsating mode, spinning detonation cannot keep its propagation due to decoupling of acoustic wave and transverse detonation. In order to discuss the physics of transverse detonation in a radial direction, I analyze the effect of acoustic coupling in radial direction using the acoustic theory and the extent of Mach leg. Acoustic theory says that transverse wave and Mach leg can rotates in a circumferential

direction when Mach number behind incident shock wave is larger than 1.841.

In the case of square tube, maximum and minimum track angle in order to keep the propagation of spinning detonation in a square tube is analyzed from the viewpoint of acoustic coupling between transverse detonation projected on walls and reflecting acoustic wave. Present results show that acoustic coupling with transverse detonation and acoustic wave traveling between walls is also important to keep the propagation as well as in the case of circular tube.

In Chapter 4, I show the propagation mechanism of curved detonations in a two-dimensional channel to clarify the effect of the size of curved channel and the stable detonation limit.

The effect of the ratio of outer and inner radii R_{out}/R_{in} of detonation propagation in a small curved channel is investigated. In a small two-dimensional curved channel whose width is equivalent to 0.5λ (λ: simulated cell width), steady detonations with curved shock front are obtained. In the case of $R_{out}/R_{in} = 2$, shock front generally stands perpendicular to walls. Chemical reaction intermittently occurs in the zig-zag chemical reaction zone, and generated compression wave affects the shock front. This induces periodical change of shock front shape and makes cellular-like pattern. In cases of $R_{out}/R_{in} \geq 3$, a steady shock front shows Mach reflection with curved incident shock and Mach stem. As R_{out}/R_{in} increases, Mach number of incoming flow in a circumferential direction of shock-attached coordinate at inner wall gradually decreases and is smaller than 1.0 in cases of $R_{out}/R_{in} \geq 7$. In cases of $R_{out}/R_{in} \leq 6$ and $R_{out}/R_{in} \geq 7$, incident waves becomes shock wave and continuous compression waves, respectively. Shock front

characteristics are discussed in detail using Whitham theory and three-shock theories with and without chemical reaction. In cases of $R_{out}/R_{in} \leq 7$, distribution of shock angle between inner wall and triple point does not agree with that by Whitham theory. However, the knowledge from shock dynamics without chemical reaction, that distribution of shock angle is independent of R/R_{in}, is also adapted to those with chemical reaction only when Mach number at inner wall is larger than 1.0. In cases of $R_{out}/R_{in} \geq 8$, shock angle does not depend on $(R-R_{in})/(R_{out}-R_{in})$, and the shock characteristics differ from those in cases of $R_{out}/R_{in} \leq 7$. As Mach number at inner wall is smaller than 1.0, continuous compression waves from weakest (Mach wave) to some strong waves are observed. Therefore, Mach wave is important propagation mechanism to decide shock front angle. I investigate structure of three-shock configuration using three-shock theories with and without chemical reaction. Depending on Mach number of triple point, the simulated incident shock angles agree well with those by three-shock theory with (at larger than CJ Mach number) and without (at smaller than CJ Mach number) chemical reaction.

In a large two-dimensional curved channel, propagation behavior and stable detonation limit are investigated. I simulate detonations with various channel widths in two types of two-dimensional curved channels, where the ratios of inner and outer radii R_{out}/R_{in} are 1.5 and 2. Two propagation modes, namely unstable and stable modes, are observed depending on the normalized inner radius R_{in}/λ. In unstable mode, diffraction and accumulation effects from inner and outer wall complexly appear in detonation propagation. A curved detonation propagates with repetition of decay, reignition and

propagation. Its velocity varies from underdriven to overdriven in one cycle. In stable mode, the detonation propagates steadily with keeping a curved shock front structure with multi-cellular pattern and a constant detonation velocity in circumferential direction. Shock front structures does not depend on R_{out}/R_{in} as well as the previous experimental studies. Since quasi-steady solution exists when the shock radius of CJ detonation front is larger than the critical value, I apply the idea of quasi-steady solution to the numerical results of detonation propagating in a two-dimensional curved channel. I confirm that the detonation propagates steadily in the case of larger shock radius of detonation front than the critical value. This says that the idea of quasi-steady solution is available to a steadily propagating curved detonation and gives the stable detonation limit in a curved channel.

In Chapter 5, double cellular detonations propagating in two-dimensional straight channel are numerically investigated with two successive reaction models governed by Arrhenius rate law whose chemical energy is released in two successive steps of different characteristic times and lengths. Soot track image shows good agreement with that of previous experiments and numerical simulations. Two cell widths λ_1 and λ_2 in double cellular detonation are formed by first and second reactions. The ratio of cell widths (λ_2/λ_1) qualitatively agrees with that of half reaction lengths (L_2/L_1). Double cellular detonation with two successive reactions is divided into two detonations, primary and secondary detonations with a single exothermic reaction, based on the relation of Rayleigh line and Hugoniot curves with the addition of the hypothetical condition of the intermediate initial state. Half reaction lengths and temperature gradient

of the primary and secondary detonations show good agreement with those of double cellular detonation. The ratio of cell widths λ_s/λ_p estimated by primary and secondary detonations shows good agreement with that (λ_2/λ_1) of double cellular detonation. This indicates that two successive chemical reactions proceed independently. The instabilities of double, primary and secondary detonations are investigated using soot track images and neutral stability curve of planar detonation. Simulated results shows that instabilities of the primary and secondary detonations is dominant to those by the first and second reactions of double detonation. It denotes that the introduction of the appropriate hypothetical condition to divide successive reactions is a useful procedure to estimate the detonation instability and its cellular structure.

References

1. M. Berthelot and P. Vieille, *Ann. Chim. Phys. Ser. 5 (28)* (1883) 289 – 332.
2. H. Dixon, *Phil. Trans A 184* (1893) 97-188.
3. D.L. Chapman, *Phil. Mag. 47* (1889) 90-104.
4. E. Jouguet, *C. R. Acad. Sci. Paris 140* (1904) 1211.
5. W.J. Rankine, *Phil. Trans. 160* (1870) 277-288.
6. H. Hugoniot, *J. Ecole Polytech., 57* (1887) 3-97.
7. H. Hugoniot, *J. Ecole Polytech., 58* (1889) 1-125.
8. Y. Zel'dovich, *Zh. Exp. Teor. Fiz. 10 (5)* (1940) 542-568
9. J. von Neumann, *Theory of detonation waves*, O.S.R.D. Rept. 549
10. W. Döring, *Ann. Phys. 5e Folge 43* (1943) 421-436
11. W. Fickett, W. C. Davis (1979), *Detonation*, University of California Press.
12. J.H.S. Lee, *Ann. Rev. Fluid Mech. 16* (1984) 311-336.
13. S. Taki, T. Fujiwara, *AIAA J. 16* (1978) 73-77.
14. V. P. Korobeinikov, V. A. Levin, V. V. Markov, G. G. Cher, *Astronaut. Acta 17* (1972) 529-537.
15. K. Kailasanath, E. S. Oran, J. P. Boris, T. R. Young, *Combust. Flame 61* (1985) 199-209.
16. A. Bourlioux, A. J. Majda, *Combust. Flame 90* (1992) 211-229.
17. M. H. Lefebvre, E. S. Oran, *Shock Waves 4* (1995) 277-283.

18. E. S. Oran, J. W. Weber, E. I. Lefebvre, J. D. Anderson, *Combust. Flame 113* (1998) 147-163.

19. V. N. Gamezo, D. Desbordes, E. S. Oran, *Shock Waves 9* (1999) 11-17.

20. V. N. Gamezo, D. Desbordes, E. S. Oran. *Combust. Flame 116* (1999) 154–165.

21. G. J. Sharpe, *J. Fluid Mech. 4* (2001) 557-574.

22. H. N. Presles, D. Desbordes, M. Guirard. C. Guerraud, *Shock Waves 6* (1996) 111-114.

23. F. Joubert, D. Desbordes, H. N. Presles, *C. R. Mec. 331* (2003) 365-372.

24. M. O. Sturtzer, N. Kamoureux, C. Matignon, D. Desbordes, H. N. Presles, *Shock Waves 14* (2005) 45 – 51.

25. J. Luche, D. Desbordes, H. N. Presles, *C. R. Mec. 334* (2006) 323-327.

26. V. Guilly, B. Khasainov, H. N. Presles, D. Desbordes, *C. R. Mec. 334* (2006) 679-685.

27. D. Desbordes, F. Joubert, F. Virot, B. Khasainov, H.N. Presles, *Shock Waves 18* (2008) 269-276.

28. F. Joubert, D. Desbordes, H. N. Presles, *Combust. Flame 152* (2008) 482-495.

29. F. Virot, B. Khasainov, D. Desbordes, H. N. Presles, *Combust. Explos. Shock Waves 45* (2009) 435-441.

30. Y. Sugiyama, A. Matsuo, *Proc. Combust. Inst. 33* (2011) 2227-2233

31. D. N. Williams, L. Bauwens, E. S. Oran, *Proc. Combust. Inst. 26* (1996) 2991-2998.

32. V. Deledicque, M. V. Papalexandris, *Combust. Flame 144* (2006) 821-837.

33. K. Eto, N. Tsuboi, A. K. Hayashi, *Proc. Combust. Inst. 30* (2005) 1907-1913.

34. N. Tsuboi, M. Asahara, K. Eto, A. K. Hayashi, *Shock Waves 18* (2008) 329-344.

35. C. Campbell, D. W. Woodhead, *J. Chem. Soc.* (1926) 3010-3021.

36. C. Campbell, D. W. Woodhead, *J. Chem. Soc.* (1927) 1572-1578.

37. C. Campbell, A. C. Finch, *J. Chem. Soc.* (1928) 2094-2106.

38. N, Tsuboi, A. K. Hayashi, *Proc. Combust. Inst. 31* (2007) 2389-2396.

39. N. Tsuboi, K. Eto, A. K. Hayashi, *Combust. Flame 149* (2007) 144-161.

40. F. Virot, B. Khasainov, D. Desbordes, H. Presles, *21st International Colloquium on the Dynamics of Explosions and Reactive Systems* (2007) on CD-ROM.

41. A.R. Kasimov, D.S. Stewart, *J. Fluid Mech. 466* (2002) 179–203.

42. Y. Sugiyama, A. Matsuo, *Proc. Combust. Inst. 32* (2009) 2331-2337.

43. D.-R. Cho, S.-H. Won, J.-R. Shin, J.Y. Choi, *Proc. Combust. Inst* (2012) in press, http://dx.doi.org/10.1016/j.proci.2012.08.003

44. G.D. Roy, S.M. Frolov, A.A. Borisov, D.W. Netzer, *Prog. Energy Combust. Sci. 30 (6)* (2004) 545–672.

45. K. Kailasanath, *AIAA J., 41 (2)* (2003) 145-159.

46. F.A. Bykovskii, S.A. Zhdan, E.F. Vedernikov, *J. Propulsion Power 22* (2006) 1204-1216.

47. F.A. Bykovskii, S.A. Zhdan, E.F. Vedernikov, *Combust. Explo. Shock Waves, 42 (4)* (2006) 463-471.

48. A. J. Mooradian, W. E. Gordon, *J. Chem. Phys. 19* (1951) 1166-1172

49. A. A. Vasil'ev, *Fiz. Goreniya Vzryva 23* (1987) 121-126

50. J. J. Erpenbeck, *Phys. Fluids 7* (1964) 684-696

51. C. A. Eckett, J. J. Quirk, J. E. Shepherd, *J. Fluid Mech. 421* (2000) 147-183

52. G. J. Sharpe, S. A. E. G. Falle, *Combust. Theory Modelling 4* (2000) 557–574

53. A. Bourlioux, A. J. Majda, and V. Roytburd, *SIAM (Soc. Ind. Appl. Math.) J. Appl. Math. 51* (1991) 303-343

54. Y. Daimon, A. Matsuo, *Phys. Fluids 15* (2003) 112-122

55. Y. Daimon, A. Matsuo, *Phys. Fluids 19* (2007) 116101

56. H. C. Yee, *NASA Technical Memorandum 89464* (1987).

57. M. Kaneshige and J.E. Shepherd. *Detonation database. Technical Report FM97-8, GALCIT*, July 1997. See also the electronic hypertext version at http://www.galcit.caltech.edu/detn db/html/.

58. A. Matsuo, T. Fujiwara, *AIAA J. 31* (1993) 1835-1841

59. A. Matsuo, K. Fujii, *AIAA J. 33* (1995) 1828-1835

60. A. Fay, *J. Chem. Phys. 20* (1952) 942-950.

61. G. L. Schott, *Phys. Fluids 8* (1965) 850-865.

62. B. V. Voitsekhovskii, V. V. Mitrofanov, M. E. Topchian, *Izd-vo Sibirsk, Odetl. Adak. Nauk SSR, Novosibirsk* (1963), Translation 1966, *Wright-Patterson Air Force Base Report, FTD-MT-64-527 (AD-633-821).*

63. M. E. Topchian, V. Y. Ul'yanitskii, *Acta Astronaut. 3* (1976) 771-779.

64. Z.W. Huang, M.H. Lefebvre, P.J. Van Tiggelen, *Shock waves* 10 (2000) 119-125

65. Y. B. Zel'dvich, *NASA Technical Memorandum 1261* (1950).

66. J. J. Lee, G. Dupre, R. Knystautas, J. H. Lee, *Shock Waves 5* (1995) 175-181.

67. V. Y. Ul'yanitskii, *Fiz. Goreniya Vzryva* 16 (1980) 105-111.

68. R. Zitoun, D. Desbordes, *Combust. Sci. Technol. 144* (1999) 93–114.

69. T. Endo, T. Fujiwara, *Trans. Jpn. Soc. Aeronaut. Space Sci. 44 (146)* (2002) 217–222.

70. T. Endo, T. Yatsufusa, S. Taki, J. Kasahara, *Sci. Technol. Energetic Mater. 65 (4)* (2004) 103–110.

71. M. Hishida, T. Fujiwara, P. Wolanski, *Shock Waves 19 (1)* (2009) 1–10

72. D. Schwer, K. Kailasanath, *Proc. Combust. Inst. 33* (2011) 2195–2202

73. Z. Pan, B. Fan, X. Zhang, M. Gui, G. Dong, *Combust. Flame 158* (2011) 2220–2228

74. Y. Uemura, A.K. Hayashi, M. Asahara, N. Tsuboi, E. Yamada, *Proc. Combust. Inst.* (2012) in press, http://dx.doi.org/10.1016/j.proci.2012.06.184

75. G.O. Thomas, R.Ll. Williams, *Shock Waves 11* (2002) 481-492.

76. S.M. Frolov, V.S. Aksenov, I.O. Shamshin, *J. Loss Prevent. Proc. Ind. 20* (2007) 501-508

77. S.M. Frolov, V.S. Aksenov, I.O. Shamshin, *Proc. Combust. Inst. 31* (2006) 2421-2428

78. S.M. Frolov, V.S. Aksenov, I.O. Shamshin, *Russ. J. Phys. Chem. B, 2 (5)* (2008), pp. 759–774

79. Y. Kudo, Y. Nagura, J. Kasahara, Y. Sasamoto, A. Matsuo, *Proc. Combust. Inst. 33* (2011) 2319-2326

80. H. Nakayama, T. Moriya, J. Kasahara, A. Matasuo, Y. Sasamoto, I. Funaki,

Combust. and Flame 159 (2012) 859-869

81. H. Nakayama, T. Moriya, J. Kasahara, A. Matasuo, Y. Sasamoto, I. Funaki, *Proc. Combust. Inst.* (2012) in press, http://dx.doi.org/10.1016/j.proci.2012.06.012
82. G.B. Whitham, *J. Fluid Mech. 2* (1957) 145-171
83. B.W. Skews, *Shock Waves 14 (3)* (2005) 137-146
84. F. Pintgen, J.E. Shepherd, *Combust. Flame 156* (2009) 665–677.
85. V.V. Mitrofanov, R.I. Soloukhin, *Sov. Phys. Dokl. 9 (12)* (1965) 1055–1058.
86. D.H. Edwards, G.O. Thomas, M.A. Nettleton, *J. Fluid Mech. 95* (1979) 79–96.
87. Y. Nagura, J. Kasahara, Y. Sugiyama, A. Matsuo, *Proc. Combust. Inst.* (2012), http:// dx.doi.org/10.1016/j.proci.2012.07.078
88. J. Yao, D.S. Stewart, *Combust. Flame 100* (1995) 519-528.
89. J. Yao, D.S. Stewart, *J. Fluid Mech. 309* (1996) 225-275.
90. S.D. Watt, G.J. Sharpe, *J. Fluid Mech. 522* (2005) 329-356
91. H. Soury, K. Mazaheri, *Int. Hydrogen Energy 34* (2009) 9847-9856

Appendix A

Solution Algorithm

Two- and three-dimensional Euler equations are solved by a finite difference method, and the unsteady solutions are obtained at each time step. Non-MUSCL type TVD upwind algorithm developed by Yee [56] is used in the present simulations. This algorithm is second-order in time and second-order in the space accurate for the system of equations. Here, I describe one-dimensional Euler equations as

$$\frac{\partial \mathbf{Q}}{\partial t} + \frac{\partial \mathbf{E}}{\partial x} = \mathbf{0}, \tag{A.1}$$

$$\mathbf{Q} = \begin{bmatrix} \rho \\ \rho u \\ e \end{bmatrix}, \quad \mathbf{E} = \begin{bmatrix} \rho u \\ \rho u^2 + P \\ (e + P)u \end{bmatrix}, \tag{A.2}$$

where, ρ, u, e and P are density, velocity, total energy per volume and pressure, respectively. The basic idea of Godunov scheme is to use the finite volume structure of spatial discretization as

$$\mathbf{Q}_j^{n+1} = \mathbf{Q}_j^n - \frac{\Delta t}{\Delta x}\left(\mathbf{E}_{j+1/2}^n - \mathbf{E}_{j-1/2}^n\right). \tag{A.3}$$

The function $\tilde{\mathbf{E}}^{n}_{j+1/2}$ is the numerical fluxes evaluated at (j+1/2). There exist many algorisms with higher order resolution, for example; Total Variation Diminishing (TVD), Monotone Upstream-Centered Schemes for Conservation Laws (MUSCL), and Essentially Non-oscillatory (ENO). Typically, $\tilde{\mathbf{E}}^{n}_{j+1/2}$ for a non-MUSCL TVD algorithm ca be expressed as

$$\tilde{\mathbf{E}}_{j+1/2} = \frac{1}{2}\left(\hat{\mathbf{E}}_{j} + \hat{\mathbf{E}}_{j+1} + \mathbf{R}_{j+1/2}\mathbf{\Phi}_{j+1/2}\right) \tag{A.4}$$

where $\mathbf{R}_{j+1/2}$ is the matrix whose columns are right eigenvectors of flux Jacobian $\partial\mathbf{E}/\partial\mathbf{Q}$. The elements of the vector $\Phi_{j+1/2}$ can be written as

$$\left(\phi^{i}_{j+1/2}\right)^{\mathrm{U}} = \sigma\left(a^{l}_{j+1/2}\right)\left(g^{l}_{j+1} + g^{l}_{j}\right) - \psi\left(a^{l}_{j+1/2} + \gamma^{l}_{j+1/2}\right)\alpha^{l}_{j+1/2} \tag{A.5}$$

where $a^{l}_{j+1/2}$ is l-th eigenvalue of $\partial\mathbf{E}/\partial\mathbf{Q}$ and $\alpha^{l}_{j+1/2}$ is the difference vector of the characteristic variables, for example, as

$$\alpha^{l}_{j+1/2} = \left(\mathbf{R}^{-1}_{j+1/2}\right)^{l}\left(\mathbf{Q}^{l}_{j+1} - \mathbf{Q}^{l}_{j}\right). \tag{A.6}$$

$\mathbf{R}^{-1}_{j+1/2}$ indicates the inverse of $\mathbf{R}_{j+1/2}$ ($\mathbf{R}^{-1}\mathbf{R}=\mathbf{I}$, $\mathbf{I}$: Identity matrix). In equation (A.5), $\gamma^{l}_{j+1/2}$ is the function of the limiter function and is defined as

$$\gamma_{j+1/2}^{l}=\sigma_{j+1/2}^{l}\begin{cases}\left(g_{j+1}^{l}-g_{j}^{l}\right)\Big/\alpha_{j+1/2}^{l} & \alpha_{j+1/2}^{l}\neq 0\\ 0 & \alpha_{j+1/2}^{l}=0\end{cases}. \tag{A.7}$$

Several types of the form of the limiter functions are suggested by Yee. In the present study, the following limiter functions are used.

$$g_{j}^{l}=\text{minmod}\left(\alpha_{j+1/2}^{l},\alpha_{j-1/2}^{l}\right) \tag{A.8}$$

where the minmod function is given as

$$\text{minmod}(\text{x},\text{y})=\text{sgn}(\text{x})\cdot\max\left\{0,\left[|\text{x}|,\text{y}\cdot\text{sgn}(\text{x})\right]\right\}. \tag{A.9}$$

In equation (A.5), $\sigma_{j+1/2}^{l}$ is expressed as

$$\sigma(z)=\frac{1}{2}\left[\psi(z)-\frac{\Delta t}{\Delta x}z^{2}\right]. \tag{A.10}$$

The $\psi(z)$ is an entropy correction function that is expressed

$$\psi(z)=\begin{cases}|z| & |z|\geq\delta_{1}\\ \left(z^{2}+\delta_{1}{}^{2}\right)\Big/2\delta_{1} & |z|<\delta_{1}\end{cases}. \tag{A.11}$$

δ_{1} is a function that defines the range of entropy correction, and should be a function of

the velocity and the sound speed. The form the function used here is

$$\delta_1 = \delta_2\left(|u| + a_{j+1/2}\right) \tag{A.12}$$

with a constant δ_2 setting to 0.1.

Approximate Riemann Solvers

It is necessary that the value at half-cell j+1/2 is evaluated. Thus, the Riemann problem at j+1/2 has to be solved. We employ the approximate Riemann solver. Among the various approximate Riemann solvers for a perfect gas, the most common one is Roe's average. For the one-dimensional, the Roe's average can be obtained as

$$\rho_{ave} = \sqrt{\rho^L \rho^R}\,, \tag{A.13}$$

$$u_{ave} = \frac{\sqrt{\rho^L}u^L + \sqrt{\rho^R}u^R}{\sqrt{\rho^L} + \sqrt{\rho^R}}, \tag{A.14}$$

$$H_{ave} = \frac{\sqrt{\rho^L}H^L + \sqrt{\rho^R}H^R}{\sqrt{\rho^L} + \sqrt{\rho^R}}, \tag{A.15}$$

where, H is total enthalpy per mass.

Appendix B

Point-Implicit Method

In order to treat stiff equations due to widely disparate time scales in source terms, it is advantageous to use the point implicit scheme in which the source terms are provided implicitly. I describe one-dimensional Euler equations with the two step reactions model by Korobeinikov *et al.* [14] as

$$\frac{\partial \mathbf{Q}}{\partial t} + \frac{\partial \mathbf{E}}{\partial x} = \mathbf{S}, \tag{B.1}$$

and

$$\mathbf{Q} = \begin{bmatrix} Q_1 \\ Q_2 \\ Q_3 \\ Q_4 \\ Q_5 \end{bmatrix} = \begin{bmatrix} \rho \\ \rho u \\ e \\ \rho\alpha \\ \rho\beta \end{bmatrix}, \quad \mathbf{E} = \begin{bmatrix} E_1 \\ E_2 \\ E_3 \\ E_4 \\ E_5 \end{bmatrix} = \begin{bmatrix} \rho u \\ \rho u^2 + P \\ (e+P)u \\ \rho u\alpha \\ \rho u\beta \end{bmatrix}, \quad \mathbf{S} = \begin{bmatrix} S_1 \\ S_2 \\ S_3 \\ S_4 \\ S_5 \end{bmatrix} = \begin{bmatrix} 0 \\ 0 \\ 0 \\ \omega_\alpha \\ \omega_\beta \end{bmatrix}, \tag{B.2}$$

where, ρ, u, e P, α and β are density, velocity, total energy per volume, pressure, induction progress and mass fraction of reactant, respectively. Reaction rate ω_α and ω_β equation of state and are described as

$$\omega_\alpha \equiv \frac{d\alpha}{dt} = -k_1 \rho \exp\left(-\frac{E_1}{RT}\right), \tag{B.3}$$

$$\omega_\beta \equiv \frac{d\beta}{dt} = \begin{cases} -k_2 p^2 \left[\beta^2 \exp\left(-\frac{E_2}{RT} \right) - (1-\beta)^2 \times \exp\left(-\frac{E_2 + Q}{RT} \right) \right] & (\alpha \le 0) \\ 0 & (\alpha > 0) \end{cases}, \tag{B.4}$$

and

$$e = \frac{P}{\gamma - 1} + \rho Q \beta + \frac{1}{2} \rho u^2, \quad P = \rho R T. \tag{B.5}$$

In Eqs. (B.3) - (B.5), k_1 and k_2 are reaction rate constants, E_1 and E_2 are activation energies and Q and γ are heat release and specific heat ratio, respectively. Using time step n+1 and n, the point-implicit finite difference scheme of equation is used for and is written as

$$\frac{\mathbf{Q}^{n+1} - \mathbf{Q}^n}{\Delta t} + \left. \frac{\partial \mathbf{E}}{\partial x} \right|^n = \theta \mathbf{S}^{n+1} + (1-\theta) \mathbf{S}^n. \tag{B.6}$$

When θ = 0, 0.5 and 1, time integration is namely fully Euler explicit method, Crank-Nicolson method and fully Euler implicit method, respecitively. Conservative variables at time step n+1 $\mathbf{Q}^{n+1}$ and $\mathbf{S}^{n+1}$ are expressed as

$$\mathbf{Q}^{n+1} = \mathbf{Q}^n + \Delta \mathbf{Q}. \tag{B.7}$$

and

$$\mathbf{S}^{n+1} = \mathbf{S}^n + \left.\frac{\partial \mathbf{S}}{\partial \mathbf{Q}}\right|^n \Delta\mathbf{Q} + O\left((\Delta t)^2\right). \tag{B.8}$$

Substituting Eqs. (B.6) - (B.8) into Eq. (B.5), implicit form of $\Delta\mathbf{Q}$ is obtained as

$$\mathbf{D}^n \Delta\mathbf{Q} = -\Delta t\left(\left.\frac{\partial \mathbf{E}}{\partial x}\right|^n - \mathbf{S}^n\right), \quad where, \;\; \mathbf{D}^n = \left(\mathbf{I} - \theta\Delta t \left.\frac{\partial \mathbf{S}}{\partial \mathbf{Q}}\right|^n\right). \tag{B.10}$$

$\Delta\mathbf{Q}$ is calculated by matrix inversion of $\mathbf{D}^n$.

The Jacobian of the chemical source term $\partial\mathbf{S}/\partial\mathbf{Q}$ in equation (B.10) for the two-step chemical reactions model by Korobeinikov et al. [14] is written in Eq. (B.11).

$$\frac{\partial \mathbf{S}}{\partial \mathbf{Q}} = \begin{pmatrix} \frac{\partial S_1}{\partial Q_1} & \frac{\partial S_1}{\partial Q_2} & \frac{\partial S_1}{\partial Q_3} & \frac{\partial S_1}{\partial Q_4} & \frac{\partial S_1}{\partial Q_5} \\ \frac{\partial S_2}{\partial Q_1} & \frac{\partial S_2}{\partial Q_2} & \frac{\partial S_2}{\partial Q_3} & \frac{\partial S_2}{\partial Q_4} & \frac{\partial S_2}{\partial Q_5} \\ \frac{\partial S_3}{\partial Q_1} & \frac{\partial S_3}{\partial Q_2} & \frac{\partial S_3}{\partial Q_3} & \frac{\partial S_3}{\partial Q_4} & \frac{\partial S_3}{\partial Q_5} \\ \frac{\partial S_4}{\partial Q_1} & \frac{\partial S_4}{\partial Q_2} & \frac{\partial S_4}{\partial Q_3} & \frac{\partial S_4}{\partial Q_4} & \frac{\partial S_4}{\partial Q_5} \\ \frac{\partial S_5}{\partial Q_1} & \frac{\partial S_5}{\partial Q_2} & \frac{\partial S_5}{\partial Q_3} & \frac{\partial S_5}{\partial Q_4} & \frac{\partial S_5}{\partial Q_5} \end{pmatrix} \tag{B.11}$$

$$= \begin{pmatrix} 0 & 0 & 0 & 0 & 0 \\ 0 & 0 & 0 & 0 & 0 \\ 0 & 0 & 0 & 0 & 0 \\ \frac{\partial \omega_\alpha}{\partial \rho} & \frac{\partial \omega_\alpha}{\partial (\rho u)} & \frac{\partial \omega_\alpha}{\partial e} & \frac{\partial \omega_\alpha}{\partial (\rho\alpha)} & \frac{\partial \omega_\alpha}{\partial (\rho\beta)} \\ \frac{\partial \omega_\beta}{\partial \rho} & \frac{\partial \omega_\beta}{\partial (\rho u)} & \frac{\partial \omega_\beta}{\partial e} & \frac{\partial \omega_\beta}{\partial (\rho\alpha)} & \frac{\partial \omega_\beta}{\partial (\rho\beta)} \end{pmatrix}$$

10 components in Eq. (B.11) are calculated by Eqs. (B.3) – (B.5).

Appendix C

One-dimensional steady solution of detonation

One-dimensional steady compressible Euler equations with two-step reaction are described as Eq. (C.1) and (C.2)

$$\frac{\partial \mathbf{E}}{\partial x} = \mathbf{S}, \tag{C.1}$$

$$\mathbf{E} = \begin{bmatrix} \rho u \\ P + \rho u^2 \\ (e + P)u \\ \rho u \alpha \\ \rho u \beta \end{bmatrix}, \qquad \mathbf{S} = \begin{bmatrix} 0 \\ 0 \\ 0 \\ \omega_\alpha \\ \omega_\beta \end{bmatrix}, \tag{C.2}$$

where, ρ, u, e P, α and β are density, velocity, total energy per volume, pressure, induction progress and mass fraction of reactant, respectively. Reaction rate ω_α and ω_β equation of state and are described as (B.3), (B.4) and (B.5), respectively.

Since values of ρu, $P + \rho u^2$, and $(e + P)u$ are constant in distance x, they are defined as

$$\begin{bmatrix} \rho u \\ P + \rho u^2 \\ (e + P)u \end{bmatrix} = \begin{bmatrix} m \\ A \\ B \end{bmatrix}. \tag{C.3}$$

Source terms are discretized by forward difference formulas as Eqs. (C.4) and (C.5).

$$\frac{(\rho u\alpha)_{j+1}-(\rho u\alpha)_j}{\Delta x}=\omega_\alpha \tag{C.4}$$

$$\frac{(\rho u\beta)_{j+1}-(\rho u\beta)_j}{\Delta x}=\omega_\beta \tag{C.5}$$

Initial state at j=1 is estimated by Rankine-Hugoniot relation of shock compression. Therefore, input parameter is detonation Mach number and upstream conditions of pressure and density. In two-step reactions model by Korobeinikov *et al.* [14], induction progress variable α first changes from 1 to 0 (exothermic progress variable β is constant with 1.0) in the induction period, and exothermic progress variable β changes from 1 to β_{eq} in the exothermic period after induction progress variable becomes smaller than 0. (e + P)u is calculated using m, A and B in (C.3) as

$$\begin{aligned}(e+P)u &= \left(\frac{P}{\gamma-1}+\rho Q\beta+\frac{1}{2}\rho u^2+P\right)u \\ &= \left[\frac{\gamma}{\gamma-1}\left(A-\frac{m^2}{\rho}\right)+\rho Q\beta+\frac{m^2}{2\rho^2}\right]\frac{m}{\rho}=B.\end{aligned} \tag{C.6}$$

One solution of Eq. (C.6) is obtained as

$$\rho_{j+1}=\frac{1}{2(Q\beta_{j+1}-B/m)}\left[-\frac{\gamma A}{\gamma-1}+\sqrt{\left(\frac{\gamma A}{\gamma-1}\right)^2+\frac{2(\gamma+1)(Q\beta_{j+1}-B/m)m^2}{\gamma-1}}\right]. \tag{C.7}$$

Integrating in distance x, one-dimensional steady solution of detonation is obtained and used for initial condition of numerical simulations in Chapters 2, 3 and 4.

Appendix D

Verification and validation

D.1. Grid convergence study

When numerical simulation of detonation is conducted, grid resolution is very important to obtain detonation phenomena including cellular structure, transverse wave interaction and complex chemical reaction zone. In many previous studies, grid spacing is determined by the number of grid points in characteristic length of chemical reaction such as induction length. Here, grid convergence study is conducted, and cell width is estimated by changing the grid spacing in induction zone length L_{ind}.

The governing equations are the same as those used in Chapter 3. The details of the compressible and reactive two-dimensional Euler equations with two-step reactions model by Korobeinikov *et al*. [14] as shown in Eqs. (2.4), (2.5), (2.6), (2.7), (2.8) and (2.9). The parameters of the chemical reaction model in the present work are listed in Table 2.1. Premixed gas is modeled as stoichiometric hydrogen-air. Initial pressure and temperature are fixed as P_1 = 1.0 atm and T_1 = 293 K, respectively.

As discretization methods, Yee's Non-MUSCL Type 2nd-Order Upwind Scheme [56] is used for the spatial integration, and Point-Implicit Method that treats only source term implicitly is used for the time integration. The details of Yee scheme and Point-Implicit Method are described in Appendix A and B. The premixed gas velocity of incoming flow is 2000 m/s, which is slightly (about 3 %) overdriven with respect to CJ velocity in

the present chemical parameters. In this condition, induction length L_{ind} of one-dimensional steady simulation is 168 μm. Adiabatic and slip conditions are adopted for the lower and upper boundaries. The axial length in the computational grid is more than 500 L_{ind} to avoid disturbance from the outflow boundary, where the non-reflected boundary proposed by Gamezo *et al.* [19] is utilized. The results of one-dimensional steady detonation are used for an initial flow distribution, where sheets of unburned gas mixture are artificially added behind detonation front in order to create initial disturbances. If the channel width is not sufficiently large, then the computed cell width is determined by the channel width itself. Thus if one is interested in determining the natural cell size, a channel width many times larger than this size is needed to ensure the result is independent of the channel width. Therefore, in this section, channel width is 10 mm (~ 80 L_{ind}), and averaged cell width is calculated. Five grid sizes (Δx = 5, 10, 20, 30, 40 μm) are investigated. Table D.1 shows the relation between grid resolution Δx and the averaged cell width λ which is converged as 1.6 mm at $\Delta x \leq 20$ μm. Therefore, numerical simulations in Chapter 2, 3 and 4 are conducted at conditions of $\Delta x \leq 20$ μm depending on computational cost.

D.2. Comparison with experiments and numerical simulation on detonation propagation from straight to curved channel

In Sect. 4.3., fully developed detonations in two-dimensional curved channel are discussed. However, no experimental results are obtained because of difficulty of experimental apparatus with several rounds in a circumferential direction. Therefore,

experiments on detonation propagation from straight to curved channel are conducted for validation of the present numerical study.

D.2.1. Experimental setup and condition

The schematics of the curved channels and observation chamber used in the experiments are shown in Fig. D.1. Inner radius R_{in} is 5 mm, and the ratio of outer and inner radii R_{out}/R_{in} is 5. The cross-section of these channels is rectangular and the width is 20 mm. The mixture gas filled in the observation chamber is ignited by a spark plug mounted at the closed end of the circular-cross-section tube below the curved channel. A deflagration wave transitions to a detonation wave within the Shchelkin spiral section mounted in the tube. The detonation wave enters the curved channel via the rectangular cross section tube. A low-vacuum dump tank is connected to the outlet port of the observation chamber, and a mylar film separates the dump tank and the observation chamber. The detonation wave passing through the curved channel ruptures the film, and the high pressure and temperature gas is caught in the dump tank.

A stoichiometric ethylene–oxygen mixture gas was used in this experiment. The mixture gas is filled at a given pressure into the observation chamber in which the air is evacuated. The temperature of the mixture gas is equal to the room temperature and initial pressure is 10.4 kPa. Cell width λ in the present initial condition is 6.97 mm from the Detonation Database of the California Institute of Technology [57]. Therefore, normalized channel width L/λ is 2.90.

D.2.2. Numerical setup

The governing equations are the same as those used in Appendix D.2. The details of the compressible and reactive two-dimensional Euler equations with two-step reactions model by Korobeinikov *et al*. [14] as shown in Eqs. (2.4), (2.5), (2.6), (2.7), (2.8) and (2.9). The parameters of the chemical reaction model in the present work are listed in Table 2.1. In general, since normalized channel width L/λ is almost the same, detonation shows similar propagation pattern, premixed gas is modeled as stoichiometric hydrogen-air which is different from that of experiment. Initial pressure and temperature are fixed as P_1 = 1.0 atm and T_1 = 293 K, respectively.

As discretization methods, Yee's Non-MUSCL Type 2nd-Order Upwind Scheme [56] is used for the spatial integration, and Point-Implicit Method that treats only source term implicitly is used for the time integration. The details of Yee scheme and Point-Implicit Method are described in Appendix A and B. Grid resolution is defined as the number of grid points in induction length L_{ind} calculated by one-dimensional steady solution. 17 grid points in induction reaction length L_{ind} are set in all directions for calculations. Figure D.2 shows the computational grid and initial conditions in the case of the ratio of outer and inner radii R_{out}/R_{in} = 5. Computational grid is composed of the straight and curved channel regions. In a straight tube region, more than 200 times of induction zone length of CJ detonation L_{ind} is set to avoid disturbance from the outflow boundary, which is proposed by Gamezo *et al.* [19]. Inner and outer wall boundaries are adopted to adiabatic and slip conditions. I confirmed that the dependency of initial condition is small for observation of fully developed flows in a curved region. Therefore, the results

of one-dimensional steady simulation of CJ condition are used as an initial condition, and initial shock front is located at joint of straight and curved channels. Channel width L is equivalent to 2.90λ (λ: simulated cell width obtained in Chapter 2).

D.2.3. Results and Discussion

Figure D.3 shows seven time-evolving schlieren images of (a) experiment and (b) numerical simulation, and interval of two images is 45 degrees. As a detonation wave enters into curved channel, diffraction from inner wall makes detonation weak, and curved front appears. Reaction front separates from leading shock front. Accumulation from outer wall generates Mach reflection, and Mach stem stands perpendicular to the outer wall and rotates in a circumferential direction. Propagation behavior at $\theta \leq 270^{\circ}$ by experiment agrees well with that by numerical simulation. This indicates that my simulation can solve detonation propagation in curved region correctly. There are no experimental results at $\theta \geq 270^{\circ}$ because of difficulty of experimental apparatus with several rounds in a circumferential direction, and I cannot validate my numerical results of steady detonation. But, I expect that the steady curved detonation can maintain its propagation in a curved small channel, and further experimental study should be conducted.

Table D.1 Relation between grid resolution Δx and cell width λ

grid resolution Δx [μm]	cell width λ [mm]
5	1.57
10	1.62
20	1.65
30	2.86
40	4.35

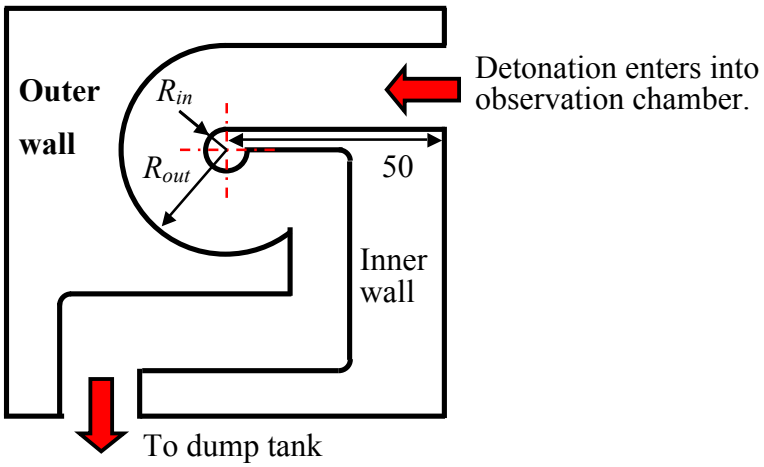

Fig. D.1 Schematics of observation chamber at R_{out}/R_{in} = 5 (R_{out} = 25 mm and R_{in} = 5 mm). Channel width is equivalent to 2.90λ (λ: cell width from the Detonation Database of the California Institute of Technology [57], 6.97 mm).

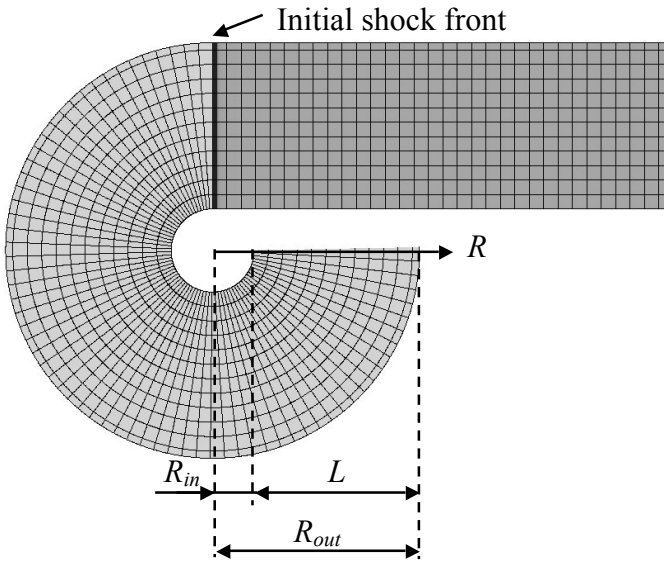

Fig. D.2 Computational grid and initial condition in the case of R_{out}/R_{in} = 5. In Appendix D, channel width L is equivalent to 2.90λ (λ: the simulated cell width in Chapter 2).

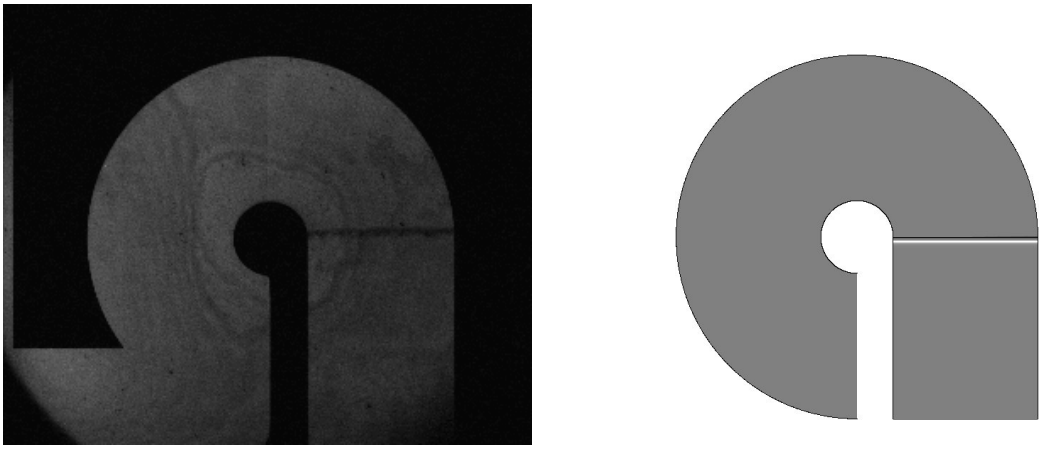

(A) $\theta = 0^{\circ}$

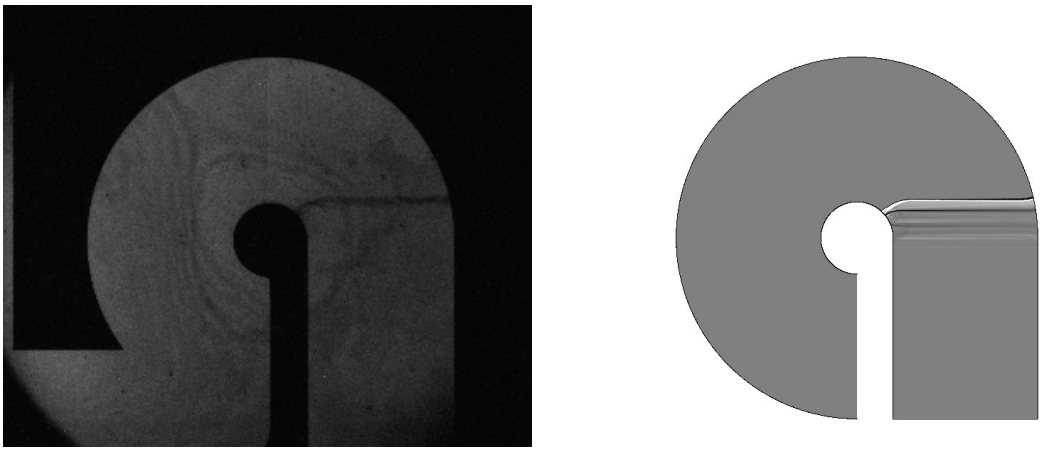

(B) $\theta = 45^{\circ}$

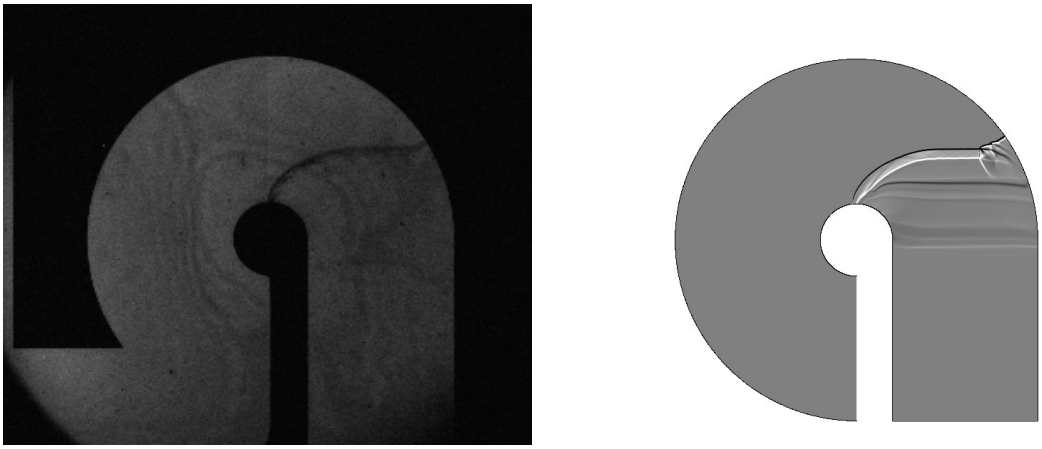

(C) $\theta = 90^{\circ}$

(a) experiment (b) numerical simulation

Fig. D.3 Seven time-evolving schlieren images of (a) experiment and (b) numerical simulation, and interval of two images is 45 degrees.

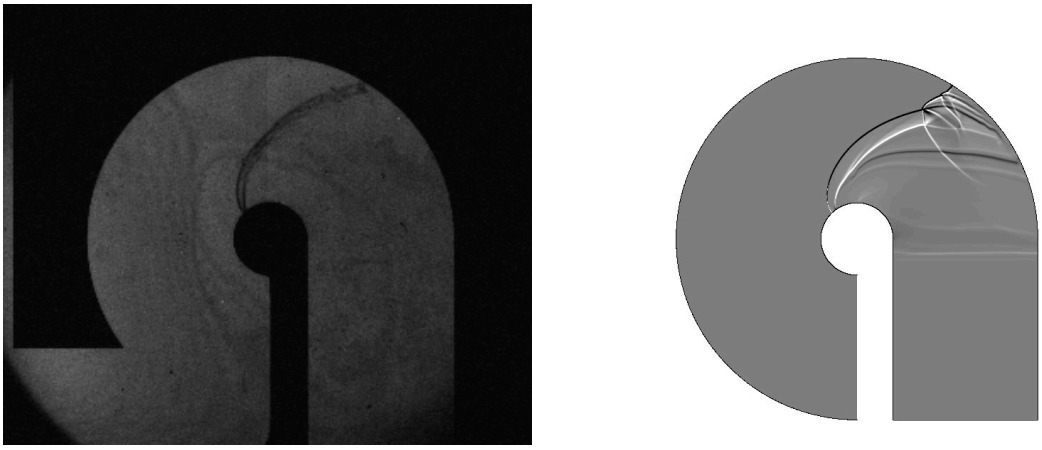

(D) $\theta = 135^{o}$

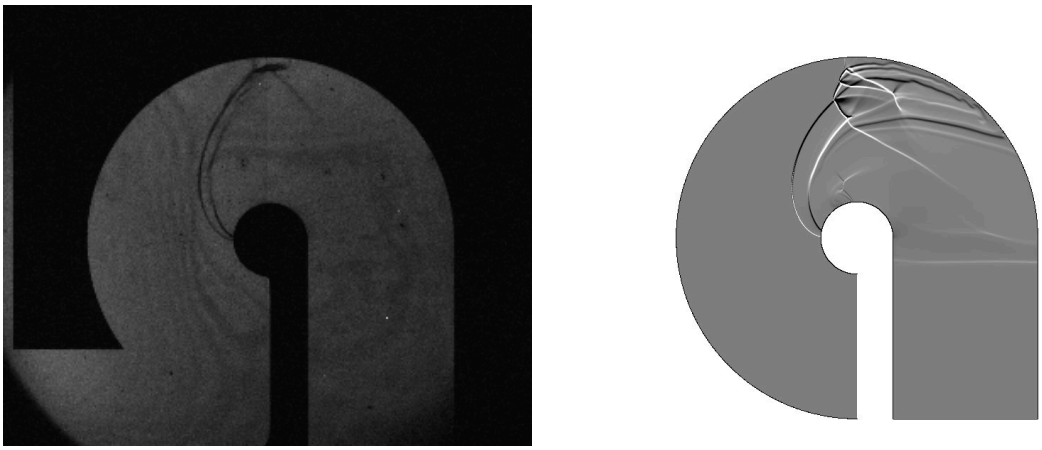

(E) $\theta = 180^{o}$

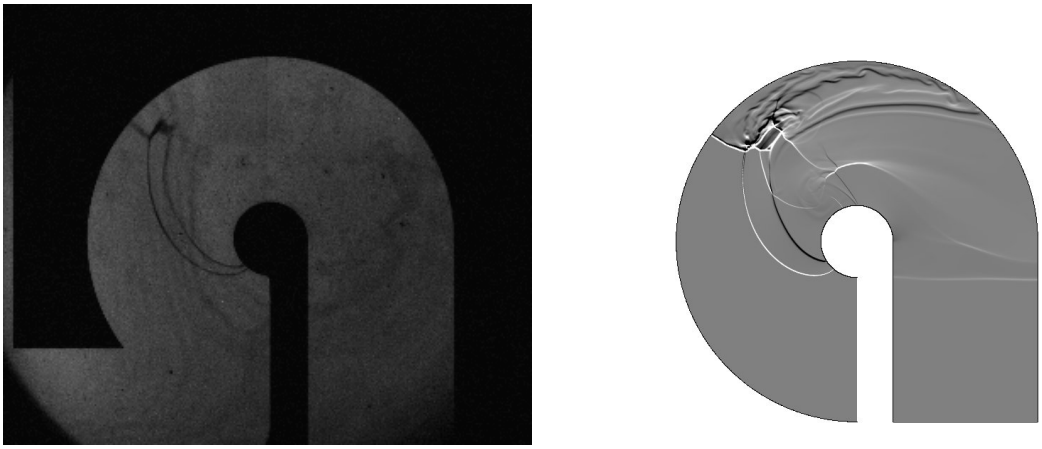

(F) $\theta = 225^{o}$

(a) experiment (b) numerical simulation

Fig. D.3(cont.) Seven time-evolving schlieren images of (a) experiment and (b) numerical simulation, and interval of two images is 45 degrees.

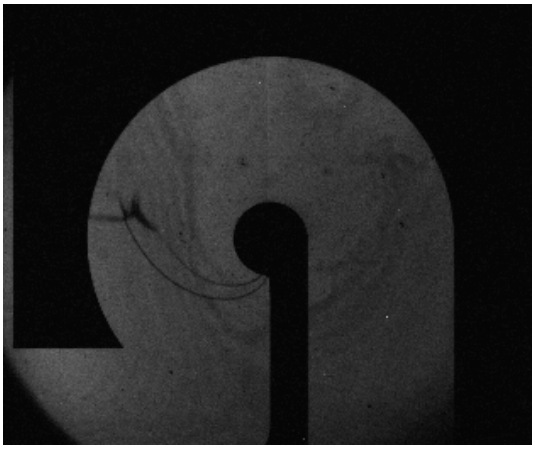

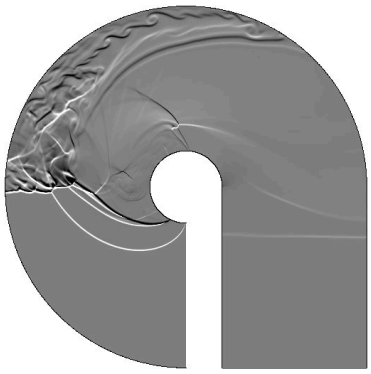

(G) $\theta = 270^{o}$

(a) experiment (b) numerical simulation

Fig. D.3(cont.) Seven time-evolving schlieren images of (a) experiment and (b) numerical simulation, and interval of two images is 45 degrees.

Appendix E

Fay's acoustic theory

Fay [60] showed theoretical spin pitch and track angle of spinning detonation using acoustic theory. Here, I describe the brief summary of Fay's acoustic theory.

Spinning detonation shows its periodic nature and the dependence of spin frequency on tube diameter. These properties suggest that spinning detonation is associated with a natural vibration of the gas such as combustion products behind the detonation waves. In order to determine the natural vibration, it is necessary to consider the vibrations to be sound waves. Under the usual assumptions of sound theory, the equation for the velocity potential ϕ in cylindrical coordinate (r, θ, z) is

$$\frac{\partial^2\phi}{\partial r^2}+\frac{1}{r}\frac{\partial\phi}{\partial r}+\frac{1}{r^2}\frac{\partial^2\phi}{\partial\theta^2}+\frac{\partial^2\phi}{\partial z^2}=\frac{1}{a^2}\frac{\partial^2\phi}{\partial t^2}, \tag{E.1}$$

where, a is sound speed. Appropriate solution of the wave equation is

$$\begin{aligned}\phi_n=\cos\left\{n\theta+2\pi\left(v-\frac{a}{l}\right)t+\frac{2\pi z}{l}\right\}\\ \times J_n\left[\frac{2\pi r}{a}\left\{v\left(v-2\frac{a}{l}\right)\right\}^{\frac{1}{2}}\right],\end{aligned} \tag{E.2}$$

where, wavelength l is z/a, v is the characteristic frequency, n is the number of circumferential crests and J_n is the Bessel function. Since spinning detonations in a circular tube apparently have one number of circumferential crest, n is considered to be 1. The wavelength l and the frequency v must be chosen so as to satisfy the two boundary conditions;

1. At the tube wall ($r = R$), the radial component of vibrational velocity must be zero.
2. At the detonation front, the changes in pressure and velocity due to the gaseous vibration must satisfy the conditions imposed by the combustion process.

From the first boundary condition, there is obtained

$$\frac{2\pi R}{a}\left\{v\left(v-2\frac{a}{l}\right)\right\}^{\frac{1}{2}} = k_{1m} \tag{E.3}$$

where

$$J_1'\left(k_{1m}\right) = 0. \tag{E.4}$$

k_{1m} is is the mth zero of the first derivative of the Bessel function J_1, the index m is the number of radial nodes (point of no radial velocity). k_{1m} is 1.841 at m = 1, 5.331 at m = 2 and so on. Since spinning detonations in a circular tube apparently have node only at

the wall, m is considered to be 1. As Z is defined as 1-vl/a, Eq. (E.3) becomes

$$v = \frac{1.841a}{2\pi R}\left(\frac{Z-1}{Z+1}\right)^{1/2} \tag{E.5}$$

Experiments showed that v is greater than a/l, therefore, Eq. (E.5) is approximately described as

$$v \approx \frac{1.841a}{2\pi R}. \tag{E.6}$$

From Eq. (E.6), sound speed a' at some radius R is expressed by Eq. (E.7).

$$a' \approx 1.841a. \tag{E.7}$$

Vibration appears behind detonation front, and therefore, sound speed a is estimated as that at CJ state a_{CJ}. Therefore, Eq. (E.7) becomes

$$a' \approx 1.841a_{CJ}. \tag{E.8}$$

Theoretical track angle α on the wall is calculated from a'/D_{CJ} (D_{CJ}: CJ detonation velocity) Rankine-Hugoniot relation as

$$\tan\alpha = \frac{a'}{V_{CJ}} = 1.841\frac{a_{CJ}}{V_{CJ}} = 1.841\frac{\gamma}{\gamma+1}\frac{\gamma \mathrm{M}_{CJ}^2+1}{\gamma \mathrm{M}_{CJ}^2} \approx 1.841\frac{\gamma}{\gamma+1}, \tag{E.9}$$

where, γ and M_{CJ} are specific heat ratio and CJ Mach number, respectively. When γ = 1.4 is substituted in Eq. (E.9), theoretical track angle becomes $\alpha = 47.0^{\circ}$.

Appendix F

Publications

Articles in Journals

Yuta Sugiyama and Akiko Matsuo, "Numerical investigation on propagation mechanism of spinning detonation in a circular tube", *Proceedings of the Combustion Institute 32* (2009), pp 2331-2337

Yuta Sugiyama and Akiko Matsuo, "On the characteristics of two-dimensional double cellular detonations with two successive reactions model", *Proceedings of the Combustion Institute 33* (2011), pp 2227-2233

Hiroki Yamashita, Jiro Kasahara, Yuta Sugiyama and Akiko Matsuo, "Visualization study of ignition modes behind bifurcated-reflected shock waves", *Combustion and Flame 159* (2012), pp 2954-2966

Yuto Nagura, Jiro Kasahara, Yuta Sugiyama and Akiko Matsuo, "Comprehensive visualization of detonation-diffraction structures and sized in unstable and stable mixtures", *Proceedings of the Combustion Institute 34* (2013), pp 1949-1956

Yuta Sugiyama and Akiko Matsuo, "Numerical investigation on the detonation regime

with longitudinal pulsation in circular and square tubes", *Combustion and Flame 159* (2012), pp 3646-3651

Oral Presentation at International Conferences

Yuta Sugiyama and Akiko Matsuo, "Three-dimensional numerical analysis for detonation propagating in circular tube", Asian Joint Conference on Propulsion and Power 2008, Gyeongju, Korea, March, 2008.

Yuta Sugiyama and Akiko Matsuo, "Numerical analysis on the dynamics of two-headed detonations in square tube", The 3rd International Symposium of Energetic Materials and their Applications, Tokyo, Japan, April, 2008.

Yuta Sugiyama and Akiko Matsuo, "Numerical investigation on propagation mechanism of spinning detonation in a circular tube", The 32nd International Symposium on Combustion, Montreal, Canada, August, 2008.

Akiko Matsuo and Yuta Sugiyama, "Computational study on unsteady mechanism of spinning detonation", Japan Korea CFD Seminar 2008, Seoul, Korea, October, 2008.

Yuta Sugiyama and Akiko Matsuo, "Numerical investigation of spinning detonations in a circular tube by one-step reaction model", 22nd International Colloquium on the

Dynamics of Explosions and Reactive Systems, Minsk, Beralus, July, 2009.

Yuta Sugiyama and Akiko Matsuo, "On the characteristics of two-dimensional double cellular detonations with two successive reactions model", The 33rd International Symposium on Combustion, Beijing, China, August, 2010.

Yuta Sugiyama and Akiko Matsuo, "Theoretical and Numerical investigations of detonation limit in a circular tube", 8th International Symposium on hazards, Prevention and Mitigation of Industrial Explosions, Yokohama, Japan, September, 2010.

Poster Presentation at International Conferences

Yuta Sugiyama, Akiko Matsuo, Hisahiro Nakayama and Jiro Kasahara, "Numerical investigations on detonations propagating in two-dimensional curved channel", The 34th International Symposium on Combustion, Warsaw, Poland, July, 2012.